Alpha Backgrounds and Their Implications for Neutrinoless Double-Beta Decay Experiments Using HPGe Detectors

Robert A. Johnson

A dissertation submitted in partial fulfillment of
the requirements for the degree of

Doctor of Philosophy

University of Washington

2010

Program Authorized to Offer Degree: Physics

University of Washington
Graduate School

This is to certify that I have examined this copy of a doctoral dissertation by

Robert A. Johnson

and have found that it is complete and satisfactory in all respects,
and that any and all revisions required by the final
examining committee have been made.

Chair of the Supervisory Committee:

John F. Wilkerson

Reading Committee:

Steven R. Elliott

Nikolai R. Tolich

John F. Wilkerson

Date:

University of Washington

Abstract

Alpha Backgrounds and Their Implications for Neutrinoless Double-Beta Decay Experiments Using HPGe Detectors

Robert A. Johnson

Chair of the Supervisory Committee:
Professor John F. Wilkerson
Physics

The observation of neutrinoless double-beta decay ($0\nu\beta\beta$) would prove the Majorana nature of the neutrino and show the non-conservation of lepton number. The nature of the neutrino (Majorana or Dirac) has implications for theories of the matter / anti-matter asymmetry of the universe, the generational structure of fundamental massive particles, and the mass of the neutrino.

The Majorana Demonstrator is a $0\nu\beta\beta$ experiment using germanium as both detector (HPGe detectors) and source to look for the decay $^{76}\text{Ge} \rightarrow {}^{76}\text{Se} + 2e^{-}$. The experimental signature for this search is a peak in the energy spectrum at 2039 keV, corresponding to the sum of the kinetic energies of the two emitted electrons where no neutrinos are emitted. Searches for $0\nu\beta\beta$ are hindered by obscuring backgrounds, and so experiments require that such backgrounds be understood and mitigated as much as possible.

A potentially important background contribution to Majorana and other double-beta decay experiments could come from decays of alpha-emitting isotopes in the ^{232}Th and ^{238}U decay chains on and near the surfaces of the detectors. An alpha particle, emitted external to an HPGe crystal, can lose energy before entering the active region of the detector, either in some external-bulk material or within the dead region of the crystal. The measured energy of the alpha will then only be a partial amount of its total kinetic energy and might coincide with the energy expected from neutrinoless double-beta decay. Measure-

ments were performed to quantitatively assess this background. This dissertation presents results from these measurements and compare them to simulations using Geant4 and to an analytic model. Surface-contamination requirements are calculated for double-beta decay experiments using high-purity germanium detectors.

TABLE OF CONTENTS

LIST OF FIGURES

Figure Number Page

LIST OF TABLES

GLOSSARY

$0\nu\beta\beta$: Short-hand for neutrinoless double-beta decay.

$2\nu\beta\beta$: Short-hand for two-neutrino double-beta decay.

$\chi 0\nu\beta\beta$: Short-hand for double-beta decay with a majoran (χ) emission.

DAQ: Data-Acquisition System

DIRAC(I): Paul A. M. Dirac (8 August, 1902 – 20 October, 1984). British theoretical physicist who discovered the equation which bares his name and made contributions to Quantum Mechanics and QED.

DIRAC(II): A particle classification. A *Dirac* particle is a fundamental fermion that is distinct from its anti-particle. All of the charged leptons are *Dirac* particles.

DGF: **D**igital **G**amma **F**inder, a series of waveform digitizers from XIA.

EMG: **E**xponentially-**M**odified **G**aussian. An exponential convolved with a gaussian distribution that is used for peak fitting.

GAT: **G**ermanium-**A**nalysis **T**oolkit, the name of a continuously-evolving suite of tools for analyzing HPGe data.

GERDA: A primarily European experiment searching for $0\nu\beta\beta$ in ^{76}Ge. Located at Gran Sasso.

HIGH-ENERGY: Usually refers to the realm of physics dealing with particles, at energies of ~ 1 GeV or above. In this document, unless otherwise noted, the adjective modifiers "high-energy" or "higher-energy" refer to the energy spectrum from an HPGe detector above 2.6 MeV.

HPGE: **H**igh-**P**urity **Ge**rmanium, typically used in conjunction with detector as in a high-purity germanium detector.

MAGE: Simulation package jointly developed by the MAJORANA and GERDA collaborations. Based on Geant4 and ROOT.

MAJORANA(I): Ettore Majorana, (5 August 1906 – 27 March 1938, presumed dead). Italian physicist who pioneered early work on neutrino mass.

MAJORANA(II): A particle classification. A *Majorana* particle is equal to it own antiparticle. Neutrinos are the only fundametal fermion for which this possibility exists.

MAJORANA(III): An experiment looking for $0\nu\beta\beta$ in ^{76}Ge.

MEGA: **M**ulti-**E**lement **G**amma **A**ssay. An array of high-purity germanium detectors inside of an electroformed copper cryostat. Designed at PNNL and installed at WIPP.

ROOT: An object-oriented software package, specifically written for high-energy data analysis. Written in C^{++}.

GEANT4: (**Ge**ometry **an**d **T**racking) An object-oriented simulation software package, written in C^{++}.

SANTA: **S**urface **A**lpha **N**-type **T**esting **A**pparatus. An n-type HPGe detector converted to a test stand for studying alpha backgrounds.

WIPP: **W**aste **I**solation **P**ilot **P**lant. An underground repository for low-level radioactive waste near Carlsbad, NM. The facility also provides space for low-background experiments.

WIPPN: An n-type HPGe detector located underground at WIPP.

XIA: XIA-LLC, formerly X-Ray Instrumentation Associates.

ACKNOWLEDGMENTS

I have wanted to be a scientist since I was six years old. This sentiment has not changed in 25 years, due in large part to my interactions with others. For starting things off, I offer thanks to my parents. They gave me beginnings, they gave me encouragement, and they let me watch 3-2-1 Contact on public television at an early age. Thank you for being awesome.

Thank you to Cy Tucker, Betty Watson, Lior Pachter, and Larry Yaffe for inspirational classes throughout the years. Thank you to Alex Filippenko, Dan Stamper-Kurn, J.C. Davis, and Sarah Keller for giving me valulable research experience. Huge thanks go out to Kyle McElroy for showing me what a physicist should strive to be.

I would like to acknowledge the people at the Waste Isolation Pilot Plant for their help with the clean room and WIPPn detector, with special thanks to Norbert Rempe and Mike Rogers.

I am very grateful for the support of many of the people at UW Physics and CENPA for keeping everything running smoothly, in particular Nichole Fernkes, Jen Lehner, Barb Fulton, Kate Higgins, Deb Nastaj, and Victoria Clarkson. I'd also like to thank Doug Will, John Amsbaugh, Greg Harper, and especially Tom Burritt for their willingness to share their technical expertise.

Thanks to my beloved postdocs and mentors, Jason Detwiler and Vincente Guiseppe. Both of them embody an amazing blend of capability and approachability, and I will attempt to follow their example in my postdoctal work and beyond.

My work at UW and LANL wouldn't have been nearly as enjoyable without the people I worked with. Thanks to Kareem Kazkaz and Vic Gehman for their help and for their absurdity. Thanks to Michelle Leber, Brandon Wall, and Noah Oblath for help and diversions. And thank you so much to my amazing office mates, Alexis Schubert and Mike Marino. I will forever owe you both baked goods.

I wish to express my deepest gratitude to John Wilkerson and Steve Elliott. They represent different sides of the same coin in terms of their approach to physics, and I have benefited from having them both. What's more, the patience they have shown in guiding me is humbling.

Thanks to my wonderful distractions. Thanks to Doug, Matt, Brian, and the rest of my first-year class for problem set help and for being ridiculous. Thanks to .83 for the lulz and shenanigans.

Most of all, thanks to Margaret for absolutely everything. Thank you for letting me cook for you.

DEDICATION

For Margaret, my candle.

Chapter 1

NEUTRINOS, DOUBLE-BETA DECAY, AND THE MAJORANA DEMONSTRATOR

"I have done a terrible thing. I have proposed a particle that cannot be detected. No theorist should have to do this." – Wolfgang Pauli (apocryphal)

"Nature gives us a peak every few keV" – Ettore Fiorini

1.1 The Universe, the Standard Model, and the Neutrino

1.1.1 A Desperate Remedy

In 1930–long before knowledge of the subatomic zoo–the theoretical proposition of a new and undetected particle was a radical concept. It was in this year that Wolfgang Pauli proposed a light, spin-$\frac{1}{2}$, electrically neutral particle of which there was no direct, experimental evidence. This particle, which would eventually be given the Italian diminutive for "neutral one" or *neutrino*, was originally introduced as a band-aid of sorts. Experiments examining the beta decay and spin of the nucleus were at odds with established tenets of physics. In beta decay as understood at the time, a nucleus undergoes a charge transition of $\Delta Z = 1$ and an electron is emitted. In such a two-body decay, conservation of energy and momentum dictate that the electron will take away a specific amount of kinetic energy. A detector measuring a great many such decays would measure a single peak at this energy, the so-called Q-value of the decay. Instead of such a single peak, a continuum of energies was observed leading up to the Q-value. It seemed that the law of conservation of energy and momentum was perhaps not so sacred after all.

This violation of the conservation laws wastroubling to physicists at the time, and so Pauli's "desperate remedy"[3] was at the very least well-motivated, if not universally accepted. If this missing, spin-$\frac{1}{2}$ particle was being ejected from the nucleus along with the electron in a 3-body decay, then the conservation laws could be saved. Soon after (in 1934), Enrico Fermi created a "4-vertex" theory of a weak interaction that incorporated the neutrino [4]. The model's predictions were soon tested and found accurate, and so opposition to the idea of a neutrino died down. The light and neutral neutrino seemed almost designed to make detection impossible, and undetected it remained until 1956 when a team led by Fred Reines and Clyde Cowan detected anti-neutrinos from the Savannah River reactor [5]. Pauli's postulation was finally proven proper.

1.1.2 The Standard Model and Massive Neutrinos

The physical world can be described by four interactions describing how particles interact with one another. In order of strength, they are: strong, electromagnetic, weak, and gravity. Gravity is the weakest force by far; it dominates over large distances, but its effect is so negligible on nuclear scales that it can be safely ignored. The other three fundamental interactions, and the very successful theory that describes how they interact with particles and with themselves, make up the Standard Model of Particle Physics (SM). Predictions from the Standard Model are overall in excellent agreement with physical measurements, but there are several reasons that the SM cannot be a complete theory. Undesirable high-energy behavior and the failure to incorporate gravity are two excellent examples that will not be mentioned again here. More germane to this dissertation is the fact that the Standard Model (in its minimal form) assumes neutrinos to be massless, and this has now been proven false. To be more specific, at least two of the three neutrino mass eigenstates have non-zero masses The clinching proof of this was found in neutrino oscillation experiments.

The three neutrino types, ν_e, ν_μ, and ν_τ, are named as such because they interact via the weak interaction with electrons, muons, and taus, i.e.

$$
\begin{aligned}
W^- &\to e^- + \overline{\nu}_e \\
&\text{or} \\
&\to \mu^- + \overline{\nu}_\mu \\
&\text{or} \\
&\to \tau^- + \overline{\nu}_\tau
\end{aligned} \tag{1.1}
$$

The "flavor" (e, μ, τ) of these neutrinos (or anti-neutrinos) is defined by the flavor of lepton emitted, and so these three neutrinos[1] constitute a basis of flavor eigenstates ($|\nu_e\rangle$, $|\nu_\mu\rangle$, $|\nu_\tau\rangle$). For reasons that are not yet theoretically understood, these flavor eigenstates turn out to be substantially different than the eigenstates of mass, ($|\nu_1\rangle$, $|\nu_2\rangle$, $|\nu_3\rangle$). These two different bases are related via a unitary transformation. An illustrative example using only two neutrino types demonstrates the concept of neutrino oscillation. The two weak states ($|\nu_e\rangle$ and $|\nu_\mu\rangle$) can be described by a linear superposition of the two mass states ($|\nu_1\rangle$ and $|\nu_2\rangle$):

$$
\begin{bmatrix} |\nu_e\rangle \\ |\nu_\mu\rangle \end{bmatrix} = \begin{bmatrix} \cos\theta & \sin\theta \\ -\sin\theta & \cos\theta \end{bmatrix} \begin{bmatrix} |\nu_1\rangle \\ |\nu_2\rangle \end{bmatrix} \tag{1.2}
$$

A neutrino might be emitted in the $|\nu_e\rangle$ state, but the propagation operator acts on the mass states. Differences in mass manifest as difference in phases when the propagation operator is applied, resulting in intererference. If a neutrino of energy E is detected a distance L away, the probability that it will be detected as a ν_μ is

$$
P_{e\to\mu}(L, E) = \left|\left\langle \nu_\mu|\hat{\mathcal{P}}(L, E)|\nu_e\right\rangle\right|^2 = \sin^2 2\theta_{12} \sin^2\left(1.267\frac{\Delta m^2_{21} L}{E}\right) \tag{1.3}
$$

where $\hat{\mathcal{P}}$ is the propagation operator and $\Delta m^2_{21} = m^2_2 - m^2_1$ is the difference of the squares of

[1]The width of the Z-boson resonance has shown that there are three active neutrinos with masses < 92 GeV. There could theoretically be other neutrinos that do not participate in the weak interaction and are "sterile," but their relevance does not intersect with this dissertation.

the neutrino masses. As shown in Eq. 1.3, the probability for a ν_μ of energy E to be found in a ν_e state a distance L away is proportional to $\sin^2 2\theta_{12}$ and disappears for $\theta_{12} = 0$ (zero mixing). The probability also depends on Δm^2_{21} and disappears if $m_1 = m_2$. The mixing matrix becomes slightly more complicated for three neutrinos, requiring three mixing angles (θ_{12}, θ_{23}, and θ_{13}), two mass-square differences (Δm^2_{21} and Δm^2_{32}), and a separate phase factor representing CP-violation ($e^{-i\delta_{CP}}$) [6, 7] :

$$|\nu_\ell\rangle = \sum_{m=1}^{N} U_{\ell m}|\nu_m\rangle$$

$$\begin{bmatrix}|\nu_e\rangle\\|\nu_\mu\rangle\\|\nu_\tau\rangle\end{bmatrix} = \underbrace{\begin{bmatrix}1 & 0 & 0\\0 & c_{23} & s_{23}\\0 & -s_{23} & c_{23}\end{bmatrix}}_{\text{Atmospheric}}\underbrace{\begin{bmatrix}c_{13} & 0 & s_{13}e^{-i\delta_{CP}}\\0 & 1 & 0\\-s_{13}e^{i\delta_{CP}} & 0 & c_{13}\end{bmatrix}}_{\text{Reactor / Long Baseline}}\underbrace{\begin{bmatrix}c_{12} & s_{12} & 0\\-s_{12} & c_{12} & 0\\0 & 0 & 1\end{bmatrix}}_{\text{Solar}}\begin{bmatrix}|\nu_1\rangle\\|\nu_2\rangle\\|\nu_3\rangle\end{bmatrix} \tag{1.4}$$

Here, s_{ij} and c_{ij} are short-hand notation for $\sin\theta_{ij}$ and $\cos\theta_{ij}$. As shown, the mixing matrix can be deconstructed into three separate matrices, each depending on only one mixing angle. The analog of Eq. 1.3 for three neutrinos is more complicated, but the physics and implications remain the same. If neutrinos of a particular flavor are observed to oscillate, then neutrinos must have different mass eigenstates. Such behavior has now been observed in many experiments ([8, 9, 10, 11]), showing that neutrinos have mass and that the Standard Model is in need of revision, or at least amendment.

The measured values or limits of θ_{ij} and Δm^2_{ij} to date are shown in Table 1.1. While θ_{12} and θ_{23} are large (especially compared with the quark-mixing matrix), the angle θ_{13} has only an upper limit. Observation of CP-violation in the neutrino sector (e.g. $P(\nu_e \to \nu_\mu) \neq P(\bar{\nu}_e \to \bar{\nu}_\mu)$) requires three non-zero mixing angles. It is for this reason that the CP phase $e^{-i\delta_{CP}}$ is attached to the $\sin\theta_{13}$ terms in the mixing matrix: looking for CP-violation becomes moot if θ_{13} is zero.

Table 1.1: Neutrino mixing-matrix parameters. Taken from [1].

$\sin^2(2\theta_{12})$	0.87 ± 0.03
$\sin^2(2\theta_{23})$	> 0.92 (90% C.L.)
$\sin^2(2\theta_{13})$	< 0.19 (90% C.L.)
Δm^2_{21}	$(7.59 \pm 0.20) \times 10^{-5}$ eV^2
Δm^2_{32}	$(2.43 \pm 0.13) \times 10^{-3}$ eV^2

1.1.3 Open Questions

The Neutrino-Mass Hierarchy Problem

Oscillation experiments are only sensitive to mass-square differences; they can tell us that neutrinos *have* mass, but not what that mass is. The magnitudes of Δm^2_{21} and Δm^2_{32} have been measured, but only the sign of Δm^2_{21} is known[2]. This leads to the so-called neutrino-mass hierarchy problem (Fig. 1.1.3). The masses of the charged fermions (up quarks, down quarks, and charged leptons) are arranged (within their own fermion family) in a similar pattern, with a narrow splitting between the lightest and medium fermion, and a larger splitting between the medium and heaviest fermions. This arrangement is a "normal" hierarchy. If $\Delta m^2_{32} = m^2_3 - m^2_2$ is positive, then $m_3 > m_2$ and neutrinos would also follow a normal hierarchy. If Δm^2_{32} is negative, than the neutrinos have an inverted hierarchy. This question is important in placing a lower mass limit on the neutrino and also for the observation of neutrinoless double-beta decay.

The Mass-Scale of the Neutrinos

The mass scale of the neutrino, while currently unknown, does have constraints. Direct-mass searches use the endpoint of a beta decay spectrum in attempts to measure the mass of the neutrino. The observable mass in such an experiment is

[2]The sign of Δm^2_{21} is known from solar-neutrino data. Neutrinos traveling through matter exhibit different oscillatory behavior due to the MSW effect (Mikheyev, Smirnov, Wolfenstein [12, 13]).

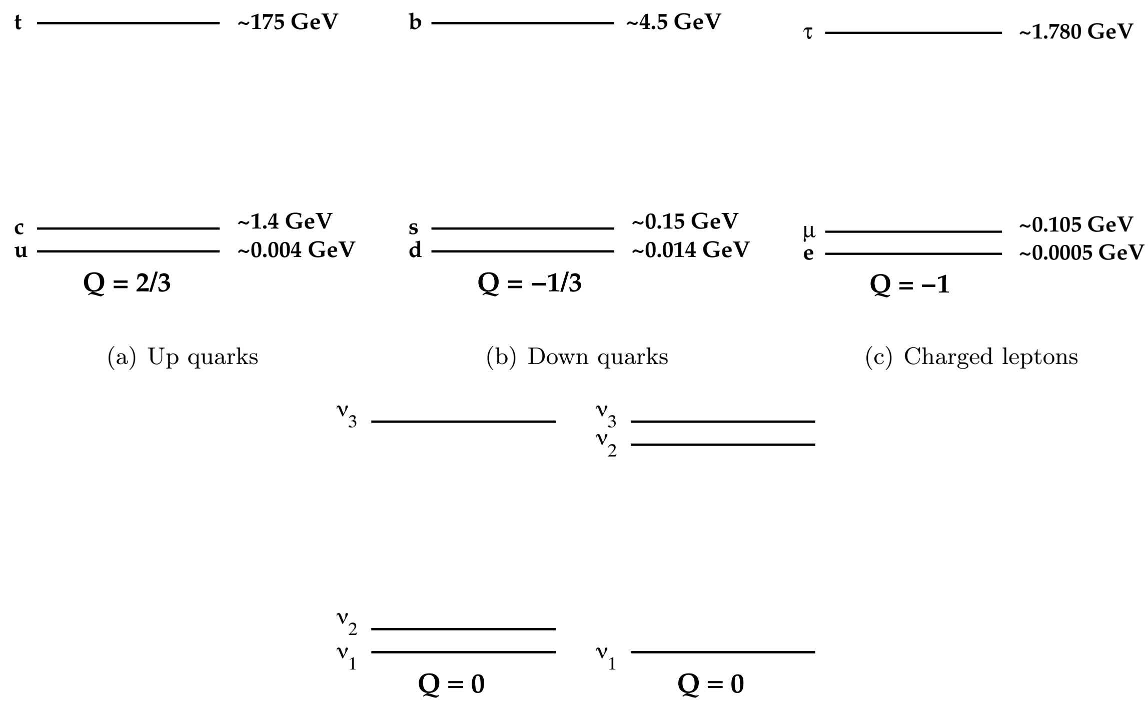

(a) Up quarks (b) Down quarks (c) Charged leptons

(d) Neutrino hierarchy, normal (left) and inverted (right).

Figure 1.1: The mass hierarchy of the charged fermions (a, b, c) and the hierarchy options for neutrinos (d). Values taken from [1].

$$m_{\nu_e} = \sqrt{\sum_l |U_{el}|^2 \, m_{\nu_j}^2}, \tag{1.5}$$

where U_{el} is the l^{th} element in the first row (corresponding to the electron) of the neutrino mixing matrix (Eq. 1.4). The Mainz collaboration published an upper limit on the mass of the electron neutrino, giving a value of $m_{\nu_e} < 2.3$ eV at the 90 % C.L.[14]. This limit is 5 orders of magnitude less than the next-lightest fermion (the electron at 511 keV). There are other, more stringent limits from cosmology, but these are also model-dependent.

The Nature of the Neutrino: Dirac vs. Majorana

The electric charges of the quarks and charged leptons ensures that each has a distinct anti-particle. For example, applying the charge-conjugation operator $\mathcal{C}$ to an electron results in a positron,

$$\mathcal{C}|e^-(\mathbf{p}, s)\rangle = |e^+(\mathbf{p}, s)\rangle, \tag{1.6}$$

where the momentum $\mathbf{p}$ and spin s are unchanged. The change in sign of the electric charges ensure that the electron and positron are different particles, just as the rest of the charged leptons and quarks are distinct from their respective anti-leptons and anti-quarks. By breaking down into underlying chiral fields, a particle can be expressed as a 4-field, e.g. an electron as (e_L, e^c_R, e^c_L, e_R) where the subscript L, R refers to left- or right-handed (chiral) and the superscript c refers to charge-conjugated. Such a particle is called a *Dirac* particle, after Paul M. Dirac who among other things discovered the Dirac equation and made significant contributions to Quantum Mechanics and Quantum-Electro Dynamics (QED).

Neutrinos participate in reactions such as

$$n \to p^+ + e^- + \overline{\nu}_e \qquad \text{(beta decay)} \tag{1.7}$$

$$\bar{\nu}_e + p \to e^+ + n \qquad \text{(inverse-beta decay)} \tag{1.8}$$

the anti-neutrino ($\overline{\nu}_e$) was observed to be right-handed and the neutrino (ν_e) was observed to be left-handed. If the neutrino has mass–as it does–then it is always possible to boost to a frame where a previously left-handed neutrino is now a right-handed neutrino, and similarly for the anti-neutrino. It then appears that we are on similar footing with the charged fermions, where we require four independent fields to describe the neutrino as a Dirac particle $(\nu_L, \nu^c_R, \nu^c_L, \nu_R)$. But the neutrino is fundamentally different than the charged fermions: the neutrality of the neutrino negates the *need* for a separate neutrino and anti-neutrino. This doesn't mean that they are not in fact different, but there is the possibility that instead of being a Dirac particle with four independent fields, the neutrino is a *Majorana* particle and needs only two: ν_L and ν_R. Whether the neutrino is Majorana or Dirac is currently unknown, but the rest of this chapter discusses the ramifications of this question and the experimental method for finding out.

1.1.4 Majorana Neutrinos and Majorana Masses

The neutrino has mass, but we don't know what it is. There are three distinct mass eigenstates; we know how far apart they are, but we don't know in which order they occur. The neutrino, alone among the fundamental fermions, is neutral and can therefore be a Majorana particle. The nature of the neutrino has important ramifications for our theoretical understanding of the Universe.

Returning to mass scales, the question of why the neutrinos are much-much smaller than the other fermions is puzzling. Neutrinos are forced to be massless in the standard model by omitting the right-handed neutrino, but the right-handed version has to exist because the neutrino has mass. How then to insert this into the Standard Model? Appendix A.1 includes a derivation of a method of inserting a right-handed Majorana neutrino. An astonishing result is that simply by including a right-handed neutrino field and imposing Lorentz-invariance, a natural mechanism to explain the mass disparity falls out. This so-called see-saw mechanism relates the (small) mass of the neutrinos with the Dirac masses of the other fermions by way of a very-heavy, right-handed Majorana neutrino [6]. The mass of this heavy neutrino is $\sim 10^{15} - 10^{16}$ GeV, approaching mass scales indicative of Grand Unified Theories (GUT). This also opens up a a vast range of theoretical possibilities, including relating Majorana neutrinos with the matter-anti matter asymmetry of the Universe by way of Leptogenesis.

In addition to the see-saw mechanism, a Majorana neutrino might also shed light on the value of mass scale for neutrinos and on the hierarchy problem. The way to discover the nature of the neutrino, and possibly the mass and hierarchy values, is via an experimental search for neutrinoless double-beta decay ($0\nu\beta\beta$).

It is worth reiterating that the distinction between Dirac and Majorana particles is only sensible for massive particles. The observation that neutrinos undergo flavor oscillations and therefore have mass represents one of the most exciting discoveries of the previous century and has opened up a large field of experimental and theoretical exploration in neutrino research. OK, neutrinos are massive, so why don't we yet know whether they are Dirac or Majorana particles? The two states of neutrino we have seen so far can be categorized as left-handed or right-handed. Those two states either constitute both states of a Majorana neutrino, or else they constitute two of the Dirac states, and are in fact a left-handed neutrino and right-handed anti-neutrino. The experimental difficulty of distinguishing between these two scenarios comes from the small mass of the neutrino in comparison to the other energy scales in the problem. A massive neutrino emitted in beta decay is a superposition of left-handed and right-handed helicity states:

$$|\nu\rangle = |\nu_R\rangle + O\left(\frac{m_\nu}{E}\right)|\nu_L\rangle \tag{1.9}$$

Assume that the neutrino mass is $\sim$ 50 meV. The total energy of the neutrino in such a decay is typically $\sim$ 1 MeV, leading to a suppression of order 5×10^{-8}. This suppression gets even worse for the energies in "controlled" (i.e. beam) experiments such as neutrinos from $\pi^{+/-}$-decay. The lepton-violation is tied to the mass of the neutrino, on the order of $\left(\frac{m_\nu}{E}\right)$. There is a promising experimental technique to surmount this small, small number, and that is the search for neutrinoless double-beta decay.

1.2 Neutrinoless Double-Beta Decay

Given the set of nuclei with A nucleons, there is typically one nucleus that is stable. As an example, Fig. 1.2 shows the ground states of the different nuclei with $A = 76$. Here, A is even and so there is a disparity in energy between even-even and odd-odd nuclei, as shown by the solid (even-even) and dashed (odd-odd) parabolas. This disparity arises form the pairing interaction between nuclei, and is absent for odd A. Certain even-even nuclei are forbidden from undergoing beta decay, either because it is energetically impossible (as in Figure 1.2 where ^{76}Ge cannot undergo beta decay because ^{76}As is heavier) or else it is suppressed by a large angular momentum barrier (such as ^{48}Ca$\rightarrow$ ^{48}Ti). While these nuclei are unable to undergo a single beta decay, the Standard Model allows for a second-order

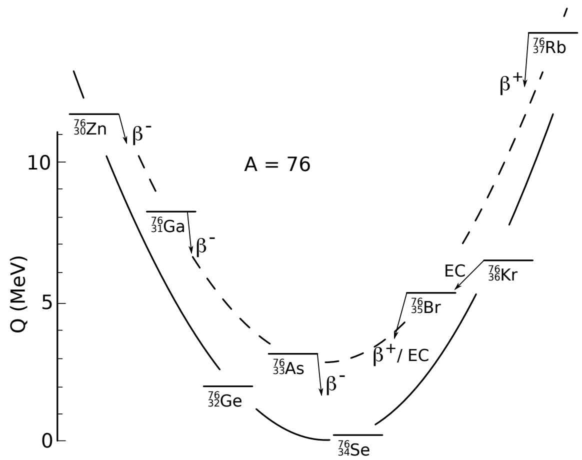

Figure 1.2: Energy levels for isotopes of A=76, taken from [7].

decay whereby the charge of the nucleus is increased by two, and two electrons and two anti-neutrinos are emitted (see Figure 1.3(a)):

$$^{A}_{Z}X \rightarrow \; ^{A}_{Z+2}X + 2e^{-} + 2\bar{\nu}_e. \tag{1.10}$$

This is called two-neutrino double-beta decay ($2\nu\beta\beta$). Using Fermi's golden rule, the half-life for the $0^+ \rightarrow 0^+$ decay can be written as

$$\left[T^{2\nu}_{1/2}(0^+ \rightarrow 0^+)\right]^{-1} = G^{2\nu}(Q,Z)\left|M^{2\nu}_{GT}\right|^2 \tag{1.11}$$

where $T^{2\nu}_{1/2}$ is the half-life for the decay, $G^{2\nu}(Q,Z)$ is an exactly calculable quantity containing phase-space factors, and $M^{2\nu}_{GT}$ is the Gamow-Teller transition amplitude. This amplitude is given by

$$M^{2\nu}_{GT} = \sum_m \frac{\langle f||\sigma\tau_+||m\rangle \langle m||\sigma\tau_+||i\rangle}{E_m - (M_i + M_f)/2}. \tag{1.12}$$

In this matrix element, the sum is over possible intermediate (virtual) states, f and i represent the final and initial states, $\sigma\tau_+$ is the axial vector operator, E_m the energy of the intermediate state, and M_i and M_f the masses of the initial and final state. This double-beta decay (Fig. 1.3(a)) differs from two simultaneous beta decays in that the intermediate nucleus (in our example, ^{76}As) is virtual. The individual beta decays can't happen on their own, but the matrix element involves a sum of the intermediate states in ^{76}As. In principle, there is also a Fermi transition amplitude with vector operators τ_+, given by:

$$M_F^{2\nu} = \sum_m \frac{\langle f||\tau_+||m\rangle \langle m||\tau_+||i\rangle}{E_m - (M_i + M_f)/2}. \tag{1.13}$$

This amplitude can be neglected, as it only comes from isospin-mixing effects. The Fermi element only governs over states in the same isospin multiplet, and the only overlap between initial and final states comes from the relatively small Coulomb interaction (see e.g. [15]).

A similar decay might involve the charge of a nucleus increasing by two, with two electrons ejected but *zero* neutrinos. The neutrino emitted form one nucleon is absorbed by another. This 0ν mode of beta decay (Fig. 1.3(b)) is <u>not</u> permitted by the Standard Model, and would therefore constitute the presence of new physics. Deviations from the Standard Model in this decay stem from lepton-number violation (in addition to the requirement of a massive neutrino). The 2ν mode emits 2 leptons (the electrons) and 2 anti-leptons (the anti-electron neutrinos), with a change in overall lepton number of 0. The 0ν mode emits 2 electrons and 0 neutrinos, resulting in an increase of lepton number by 2 and would show the non-conservation of lepton number.

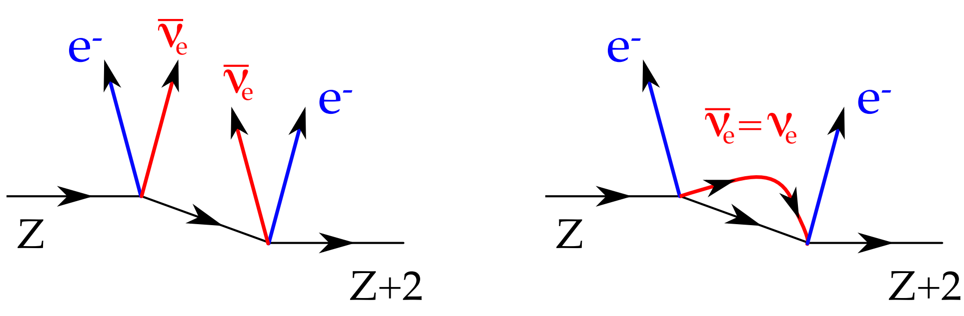

(a) 2ν mode (b) 0ν mode

Figure 1.3: Simplified Feynman diagrams for double-beta decay. The diagram in (b) assumes a $0\nu\beta\beta$ mechanism involving the transfer of a light-neutrino between nucleons.

The 0ν mode of double-beta decay is assumed to be dominated by the exchange of a light Majorana neutrino between nucleons in the nucleus, as this is the simplest mechanism and follows directly from adding a Majorana neutrino mass to the current Standard Model. There are more exotic mechanisms that would allow this decay as well, such as from various supersymmetric models or right-handed currents. Understanding the underlying mechanism is not critical in terms of the Dirac/Majorana debate, and the importance of double-beta decay can be summarized in the following line: "Any process that allows $0\nu\beta\beta$ to occur requires Majorana neutrinos with non-zero mass." This quote is taken from a paper by Schechter and Valle [16], who provide an elegant proof of the assertion. Their argument is presented in Fig. 1.4. No matter the mechanism for $0\nu\beta\beta$ (hidden in the figure by a black box, Fig. 1.4(a)), one can write down a Feynman diagram for the external outgoing particles. By assuming normal Standard Model vertices, the diagram in Fig. 1.4(b) can be constructed, just as in any other Standard Model diagram. The diagram then becomes a mechanism for converting a right-handed anti-neutrino into a left-handed neutrino, which is exactly the criteria for a Majorana-mass term. In plain terms, observation of $0\nu\beta\beta$ proves that neutrinos are Majorana particles and that lepton number is not conserved, even if the exact mechanism for $0\nu\beta\beta$ is unknown. The underlying mechanism *is* important for extracting information about the neutrino's mass scale, and so extracting the physics will depend on several observations in different isotopes (see e.g. [17]).

In a model with massive, Majorana neutrinos, the half-life for the 0ν mode of beta decay, $0^+ \to 0^+$, is

$$\left[T^{0\nu}_{1/2}(0^+ \to 0^+)\right]^{-1} = G^{0\nu}(Q,Z)\left|M^{0\nu}_{GT} - \frac{g_V^2}{g_A^2}M^{0\nu}_F\right|^2 \langle m_{\beta\beta}\rangle^2 \tag{1.14}$$

with $G^{0\nu}$ again an exactly calculable quantity ([18]). M_{GT} and M_F are the Gamow-Teller and Fermi nuclear matrix elements. The Fermi term cannot be ignored here, because the matrix elements must now include the propagator for the virtual neutrino intermediary, leading to significant overlap of the initial and final states. The term $\langle m_{\beta\beta}\rangle$ has units of mass and is a measure of the amount of lepton-number violation in the decay. In other words, this term contains any "new physics" and is zero if the neutrino is not a Majorana fermion.

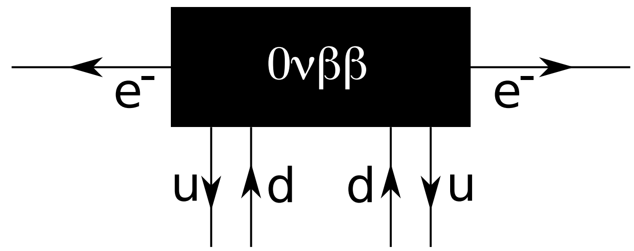

(a) Feynman diagram for $0\nu\beta\beta$, with the $0\nu\beta\beta$ mechanism hidden by a black box.

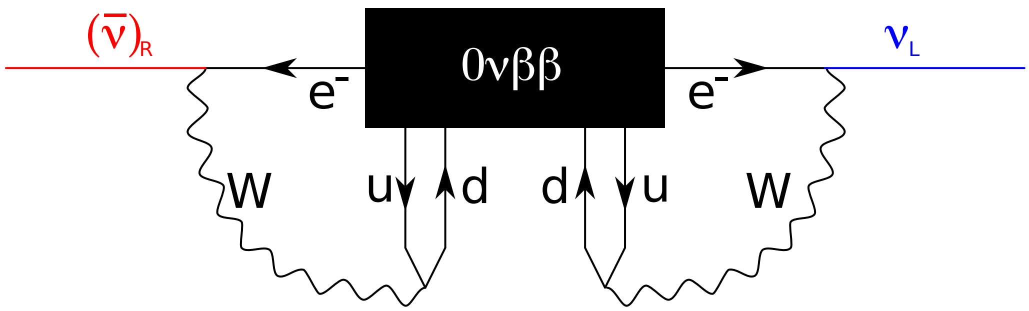

(b) Applying Standard-Model interactions converts a right-handed anti-neutrino into a left-handed neutrino, to wit, a Majorana mass term.

Figure 1.4: Pictorial proof of the assertion that observation of $0\nu\beta\beta \Rightarrow$Majorana neutrinos. Adapted from [16].

While there are many mechanisms that might give rise to $0\nu\beta\beta$, the simplest involves the transfer of a light neutrino between nucleons. For this mechanism, the lepton-violating term is proportional to the neutrino mass:

$$\langle m_{\beta\beta} \rangle = \left| \sum_j m_j U_{ej}^2 e^{i\alpha_j} \right| \tag{1.15}$$

The phases α_j are possible CP-violating phases. The mass in Eq. 1.15 contains a coherent sum and the CP-violating phases leave open the possibility of cancellations. This is in direct contrast to the incoherent sum in Eq. 1.5, the neutrino mass measured in beta decay endpoint experiments. Figure 1.5 plots the value of $\langle m_{\beta\beta} \rangle$ as a function of the lightest mass eigenstate. The hierarchy problem is illustrated here by the two different curves. Uncertainties in matrix-element calculation are not included, and the phase space represents all possible values of the CP-violating Majorana phases α_1 and α_2.

The observation of $0\nu\beta\beta$ would demonstrate that neutrinos are Majorana particles and that lepton number is not a conserved quantity. A measurement of the half-life of $0\nu\beta\beta$ would constitute a measurement of the lepton-number violating term, establishing the absolute mass scale for the neutrino if the light-neutrino exchange is the dominant $0\nu\beta\beta$ mechanism. It could also, in principle, distinguish between the two hierarchies. All that is left to do is to actually observe and measure this decay.

1.3 Measuring $0\nu\beta\beta$

1.3.1 Experimental aspects of double-beta decay measurements

At the most basic level, a search for double-beta decay involves an amount of the isotope of interest along with some way to measure the betas that are emitted from the material. The observed signal–or lack-thereof–either gives a value or a lower-limit on the half-life of the decay, depending on the detector livetime and mass of the candidate isotope.

The energy of the decay is split amongst the 4 leptons (with a very small fraction going to the recoil of the nucleus), and measuring the summed energies of the electrons will result in a continuous energy spectrum from 0 to the Q-value (See Figure 1.6). This is similar to the situation for single-beta decay. For the 0ν mode, the absence of any emitted neutrinos means that the kinetic energy of the electrons corresponds to the full Q-value of the decay. The corresponding energy spectrum would occur at a peak at the Q-value (Figure 1.6). This peak is the experimental signature for $0\nu\beta\beta$. Observation of this peak would establish the Majorana nature of the neutrino, and the peak area would determine the value of $T^{0\nu}_{1/2}$ . . . with one large caveat. One has to be sure that the peak comes from $0\nu\beta\beta$, and not other backgrounds. The situation is made more complicated in practice because there are many physical processes that can deposit energy in a detector at the Q-value for a given isotope. These background events can mimic the signal from $0\nu\beta\beta$ decay, decreasing sensitivity to such a search. The resolution of radiation detectors can also limit sensitivity.

There are many sources of noise that contribute to the observed width of a peak in an

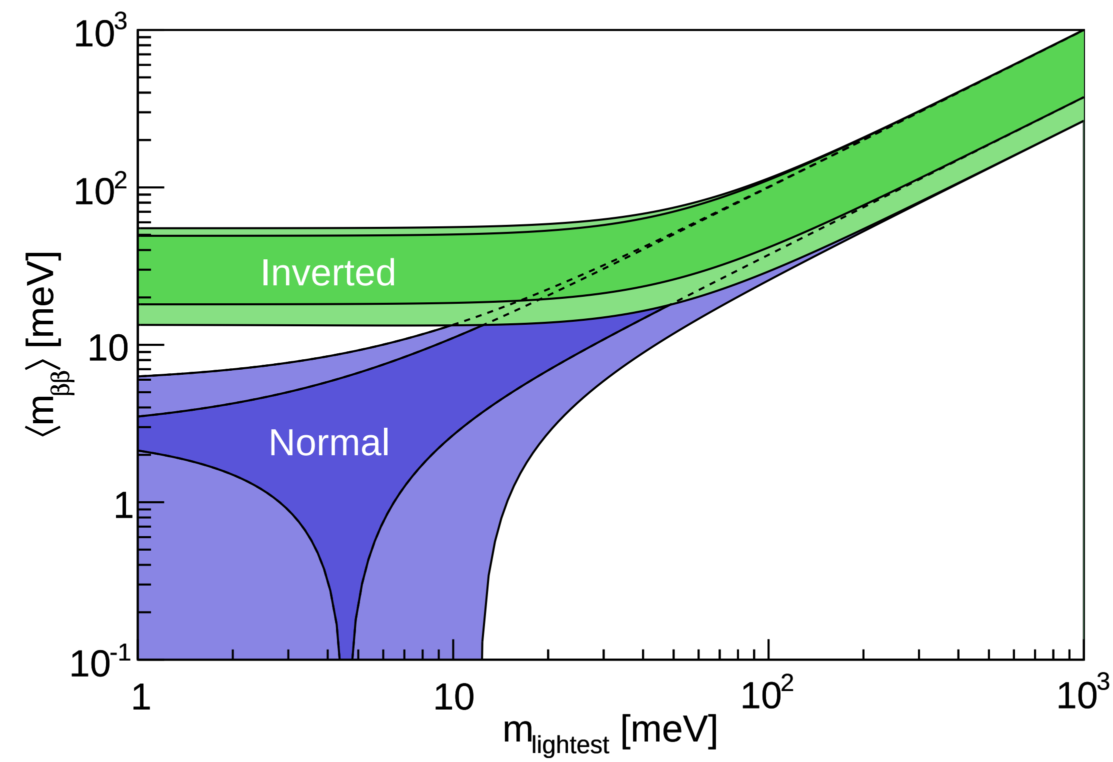

Figure 1.5: Value of $\langle m_{\beta\beta} \rangle$ (light-neutrino exchange) as a function of the lightest neutrino mass eigenstate (from Eq. 1.15). The neutrino-mass hierarchy is unknown, so the lightest neutrino mass is either m_1 (normal) or m_3 (inverted), and this is represented in the figure by the two different phase spaces. The dark regions assume the best-fit oscillation parameters with θ_{13} taken to be zero. The variance in the dark regions is then exclusively from the Majorana phases. The ligher-shaded regions incorporate the uncertainty in the oscillation parmaeters at the 68% confidence level, as taken from [1]. Figure from A.G. Schubert.

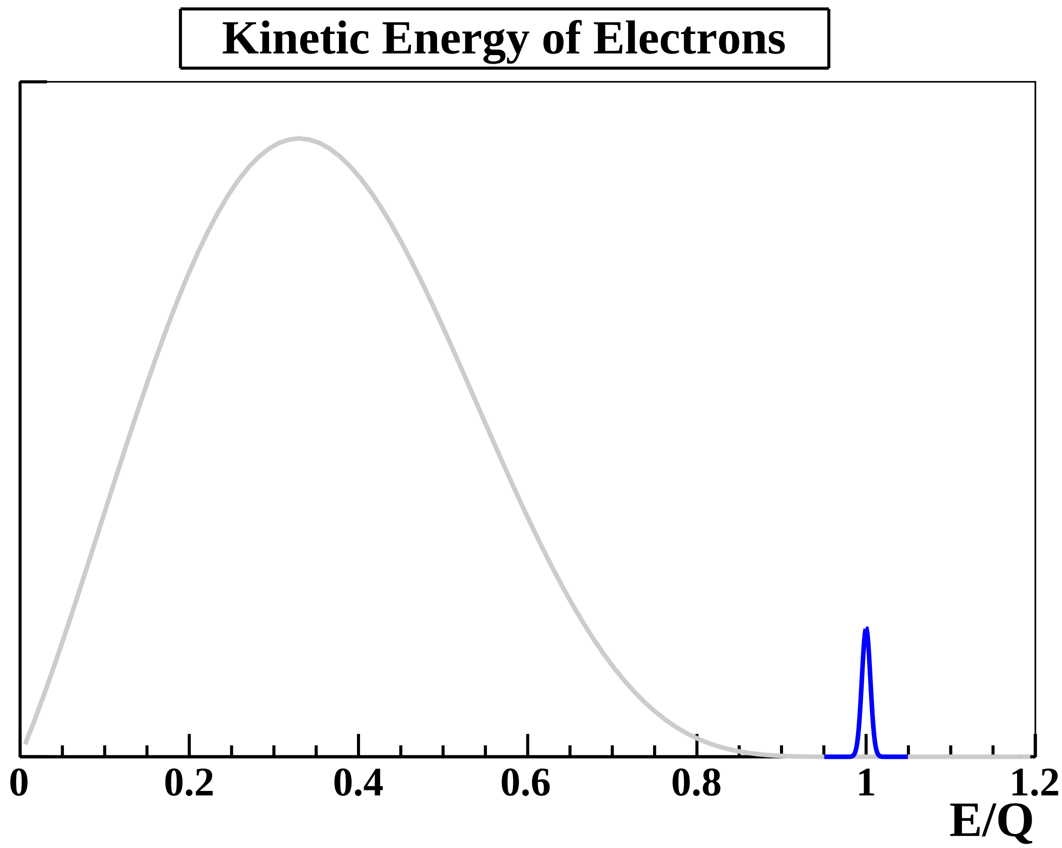

Figure 1.6: The sum of kinetic energies of the two emitted electron in double-beta decay. The 0ν signal is at the Q-value, because there are no emitted neutrinos to carry away kinetic energy.

Table 1.2: Q-values for select $0\nu\beta\beta$ isotopes. The half-life of the 2ν mode is included if it has been measured. Values taken from [19].

Isotope	Q-Value [keV]	$T_{1/2}^{2\nu}$ [y]
^{48}Ca	4274.0 ± 4	$(4.2^{+2.1}_{-1.0})\times10^{19}$
^{76}Ge	2039.0 ± 0.05	$(1.5 \pm 0.1)\times10^{21}$
^{82}Se	2995.5 ± 1.9	$(9.2 \pm 0.7)\times10^{19}$
^{100}Mo	3035.0 ± 6	$(7.1 \pm 0.4)\times10^{18}$
^{116}Cd	2809.0 ± 4	$(3.0 \pm 0.2)\times10^{19}$
^{130}Te	2530.3 ± 2.0	$(0.9 \pm 0.1)\times10^{21}$
^{150}Nd	3367.7 ± 2.2	$(7.8 \pm 0.7)\times10^{18}$

energy spectrum, but the largest is typically the statistical variance of collected charges. The measured width of a peak at the Q-value determines the “Region of Interest", or ROI, for double-beta decay. For ^{76}Ge, the excellent resolution of High purity germanium (HPGe) detectors gives a region of interest of $\sim$ 4 keV at the Q-value of 2039 keV. Counts within this region can be either from $0\nu\beta\beta$ or backgrounds. The hard part is determining which is which.

1.3.2 Backgrounds and Sensitivity in $0\nu\beta\beta$ Experiments

The region-of-interest (ROI) is the energy window in which to look for counts from $0\nu\beta\beta$. For a $0\nu\beta\beta$ half-life for given by $T_{1/2}^{0\nu}$, the rate of counts in the ROI is proportional to $1/T_{1/2}^{0\nu}$. The rate also scales with the number of target isotopes (N_a), and so is also proportional to the detector mass. The efficiency (ε) for a decay to register with the detector is dependent upon the geometry, but this is generally close to 100% for experiments utilizing target source as the detector. For N_a isotopes, the rate of decay is

$$\mathcal{R} = \frac{N_a}{\tau} = \ln(2)\frac{N_a}{T_{1/2}^{0\nu}}. \tag{1.16}$$

Assuming that there are N_S counts in the ROI that are *all* signal with *no* backgrounds and detection efficiency ε, the actual decay rate ($\mathcal{R}$) is related to the measured rate ($\mathcal{R}_m$) by

$$\mathcal{R} = \frac{\mathcal{R}_m}{\varepsilon} = \frac{N_{\mathrm{S}}}{\varepsilon \Delta t} \tag{1.17}$$

where Δt is the livetime of the measurement. The half-life can then be extracted from such a measurement as

$$T_{1/2}^{0\nu} = \frac{\ln(2) N_a \varepsilon \Delta t}{N_{\mathrm{S}}}. \tag{1.18}$$

This of course represents an ideal experiment with zero backgrounds. This is not the case in practice. Backgrounds in the ROI come from radioactive and cosmogenic sources. Simply put, any physical process that can deposit energies at or above the ROI can constitute a background for $0\nu\beta\beta$ experiments. The Q-values for a number of candidate $0\nu\beta\beta$ nuclei are listed in Table 1.2. Typical background-source culprits come from the ^{238}U and ^{232}Th decay chains and other radioactive isotopes, neutrons, and cosmic rays. Even the 2ν mode of double-beta decay. Experimentally, the two decays are exactly the same except for the amount of energy deposited. This background cannot be vetoed, and good detector resolution is the only way to distinguish the high-energy tail of $2\nu\beta\beta$ from a $0\nu\beta\beta$ peak. ^{60}Co and ^{68}Ge are cosmogenic backgrounds, produced by cosmic ray interactions with copper and germanium within a detector. From the U and Th decay chains, backgrounds can come from higher energy gammas (^{208}Tl and ^{214}Bi), beta decays with higher endpoint energies, and all of the α-decays. Energies from α-decays in the U and Th chains range from 3.9-8.8 MeV, and their effects are discussed in Chapter 2.

For an experiment with no discernible signal, the sensitivity for a double-beta decay experiment, in terms of a half-life limit, is given by

$$T_{1/2}^{0\nu} > \frac{\ln(2) N_a \Delta t \varepsilon}{\mathrm{UL}_{90}\left(\mathcal{B}(\Delta t)\right)} \qquad (90\% \text{ C.L.}), \tag{1.19}$$

where again N_a is the number of target isotopes in the sample, Δt is the live-time, and ε is the detection efficiency. In the denominator, $\mathcal{B}(\Delta t)$ is the total number of background counts and $\mathrm{UL}_{90}(\mathcal{B}(\Delta t))$ is then the upper limit on signal count at confidence level 90%, using the "Unified Approach" of interval estimation of Feldman and Cousins [20, 21]. The half-life limit scales with time as $\frac{\Delta t}{\mathrm{UL}_{90}(\mathcal{B}(\Delta t))}$, and so it is desirable to limit UL_{90}, and hence backgrounds, by as much as possible. For minimal backgrounds, UL_{90} is essentially constant and the half-life sensitivity scales with Δt. Increasing $\mathcal{B}(\Delta t)$ results in decreased half-life sensitivity, underscoring the need to understand and eliminate backgrounds by as much as possible.

1.4 The Majorana *Experiment*

The Majorana Demonstrator is a next-generation search for the neutrinoless double-beta decay $^{76}\mathrm{Ge}\rightarrow^{76}\mathrm{Se} + 2e^-$. The overall design of the experiment represents the natural evolution of detector and materials technology applied to previous-generation experiments. This is in contrast to the GERDA experiment, which is discussed in the next section and presents some fundamental changes in design.

1.4.1 $0\nu\beta\beta$ and Backgrounds in HPGe Detectors

In 1967, Ettore Fiorini *et al.* pioneered the technique of using the detector as the source in a double-beta decay search. Using a small Ge diode, the group were able to set a half-life limit for $0\nu\beta\beta$ in ^{76}Ge of $T_{1/2} > 3 \times 10^{20}$ years [22]. Since then, the use of ^{76}Ge has consistently given the most sensitive half-life limits. The current limit, $T^{0\nu}_{1/2}(^{76}\mathrm{Ge}) > 1.9 \times 10^{25}$ years (90%C.L.) [23], was achieved by the Heidelberg-Moscow collaboration with 10.96 kg of ^{76}Ge. The International Germanium Experiment (IGEX) collaboration has published a similar measurement, $T_{1/2} > 1.6 \times 10^{25}$years (90%C.L.) [24]. These two measurements represent not only the best half-life limit for ^{76}Ge, but for any $0\nu\beta\beta$ isotope. As always for low-background experiments, further progress requires lowering backgrounds. For completeness, it is important to note that there is a claim of discovery of observation of $0\nu\beta\beta$ in ^{76}Ge by a subset of the Heidelberg-Moscow Collaboration. They claim a value of $T^{0\nu}_{1/2} = (2.23^{+0.44}_{-0.31}) \times 10^{25}$ y [25, 26]. This is not without controversy, as it does not have the backing of the full Heidelberg-Moscow Collaboration and questions have been raised about the understanding of backgrounds near the ROI [27]. Suffice it to say, the claim needs to be either confirmed or refuted, and this is precisely what the current round of $0\nu\beta\beta$ experiments intend to do.

The emission of 2 electrons in $0\nu\beta\beta$ occurs within a small region of the detector, and so the decay classifies as a "single-site" event. In contrast, many backgrounds will simultaneously deposit energy in multiple portions of a detector (or even multiple detectors). Many background-rejection techniques rely on distinguishing these "multi-site" events from single-site events.

$0\nu\beta\beta$ experiments in general, are designed around the concept of maximizing the possible signal while minimizing backgrounds. Experiments using ^{76}Ge accomplish this in several ways:

Source as detector – Any material within an experiment will contribute backgrounds at some level, thanks to the ubiquitousness of ^{238}U and ^{232}Th . By using the detector as the source, $0\nu\beta\beta$ experiments with ^{76}Ge minimize the amount of non-active mass that makes up a detector.

Enrichment – HPGe detectors can be isotopically enriched to 86% ^{76}Ge. This is another method of adding active mass without adding backgrounds.

Energy resolution – The resolution for HPGe detectors at 2039 keV is 0.16%, resulting in a region-of-interest (ROI) of less than 4 keV. This minimizes backgrounds, including the otherwise unescapable $2\nu\beta\beta$ signal.

Background rejection – Analysis techniques using HPGe detectors are well-established, allowing multi-site events (like most backgrounds) to be distinguished from single-site events such as $0\nu\beta\beta$.

Intrinsic Purity – HPGe detectors are intrinsically pure — they wouldn't work as semiconductors if they weren't. This reduces the amount of ^{238}U and ^{232}Th within the crystal.

All of these capabilities are taken advantage of in the Majorana Demonstrator.

1.4.2 The MAJORANA DEMONSTRATOR

The goals of MAJORANA are aimed at pursuing the development of R&D toward a tonne-scale $0\nu\beta\beta$ experiment using ^{76}Ge in HPGe detectors [28]. The technical goal is to demonstrate that backgrounds are low enough to justify building a tonne-scale experiment, and the science goal is to test the claim of observation of $0\nu\beta\beta$ in ^{76}Ge by Klapdor *et al.* [25, 26]. These goals will be accomplished by building the MAJORANA DEMONSTRATOR. The DEMONSTRATOR will consist of 40 kg of HPGe detectors, mounted in ultra-clean copper cryostats. Somewhere between 20 and 30 kg of the detectors will be enriched to 86% ^{76}Ge, while the remainder will consist of natural germanium[3]. The design of the DEMONSTRATOR was chosen to facilitate background reduction by using ultra-clean materials and the ability to veto multi-site events. $0\nu\beta\beta$ is fundamentally a single-site event, so any event that can be shown to be multi-site can be vetoed.

Modified BEGe Detectors

The MAJORANA DEMONSTRATOR will be used to study different technologies of HPGe detectors. One of these technologies is a type of P-type HPGe detector, modified with a point-contact (P-PC). It is this type of detector that will populate the first module of the DEMONSTRATOR. These detectors are made by Canberra[29] and are a modification to a standard line of detectors known as BEGe detectors (short for Broad-Energy Germanium). Standard BEGe detectors have a special thin n^+ deadlayer on their top cylinder surface, whereas the modified BEGe detectors have a uniform n^+ layer of 0.5 mm. P-PC detectors like these BEGe's have shown excellent pulse-shape discrimination results in distinguishing single-site from multi-site events [30].

Background Model for the MAJORANA DEMONSTRATOR

Minimizing backgrounds in an experiment requires understanding what those backgrounds are and where they come from. The MAJORANA background model has been constructed to summarize the expected source of backgrounds to the DEMONSTRATOR, tak-

[3] The isotopic abundance of ^{76}Ge in natural germanium is 7.4%

Table 1.3: Background budget for the MAJORANA DEMONSTRATOR

Component	Source [Isotope]	Background Cnts / ROI / t-y	
		DEMONSTRATOR	Tonne-Scale
Germanium Crystals (enriched)	^{68}Ge	0.38	negligible
	^{60}Co	0.03	negligible
	U/Th	0.3	0.3
Cryostat, Inner Cu Shield	^{208}Tl, ^{214}Bi	0.91	0.48
Outer Cu Shield	^{208}Tl, ^{214}Bi	0.4	0.02
	^{60}Co	0.02	1×10^{-3}
Pb Shield	^{208}Tl, ^{214}Bi	0.4	negligible
Prompt Cosmogenics	(n,*)	~ 1	negliglble
All Others		0.38	0.27
Total:		3.81	1.07

ing into account what we know of the materials that the DEMONSTRATOR will comprise and in what environment it will operate. Table 1.3 presents a short summary of expected backgrounds, both for the DEMONSTRATOR and for a tonne-scale experiment (as described in the next section). The largest sources of background arise, unsurprisingly, from the materials closest to the crystal detectors, i.e. the cryostat and inner copper shielding.

1.4.3 Beyond the DEMONSTRATOR

The MAJORANA DEMONSTRATOR is not the only next-generation $0\nu\beta\beta$ using ^{76}Ge under construction. The GERDA Collaboration (GERmanium Detector Array) is a European experiment installing a $0\nu\beta\beta$ experiment in Gran Sasso (Laboratori Nazionali del Gran Sasso, or LNGS) near Aquila, Italy [31]. The fundamental difference between MAJORANA and GERDA is that GERDA is eschewing the tried-and-true copper cryostats and will instead house the bare crystals within liquid Argon. This represents a large difference from previous $0\nu\beta\beta$ experiments. Phase-I of the GERDA experiment will use the enriched HPGe detectors from the IGEX [24] and Heidelberg-Moscow [23] experiments with an exposure goal of 30 kg-y. Phase-II will include additional detectors with a goal of 100 kg-y of exposure. Like MAJORANA, GERDA is actively pursuing different detector technologies.

The MAJORANA and GERDA Collaborations have agreed to combine into a single, future, tonne-scale experiment. The technology used in this future experiment will represent the best of both MAJORANA and GERDA. Indeed, the two collaborations have already co-operated to build a joint Monte Carlo package, MaGe (Chapter 3).

Chapter 2

ALPHA BACKGROUNDS IN HIGH-PURITY GERMANIUM DETECTORS

Alpha particles, specifically those coming from the ^{238}U and ^{232}Th decay chains, are emitted with initial kinetic energies between 3.9 and 8.8 MeV. The Q-value for $0\nu\beta\beta$ in ^{76}Ge is 2.039 MeV, so alphas only pose a background if they are “degraded” and deposit only a fraction of their energy in the active region of the detector. The susceptibility of a $0\nu\beta\beta$ experiment to backgrounds from alphas depends on the type of HPGe detector and the mechanism of energy degradation.

2.1 HPGe Detectors

2.1.1 Surface Types

HPGe (High-Purity Germanium) detectors are semiconductor crystals formed of high-purity germanium. They are essentially diodes, or p–n junctions (Figure 2.1), and require two electrical contacts at the surface: a p^+ layer and an n^+ layer. During operation as a detector, the crystal is reverse biased (with several kV), resulting in a depletion region between the contacts. This depletion region constitutes the active portion of the crystal, i.e. energy deposits will liberate electron-hole pairs which will be swept to the contacts and read out by the Data Acquisition system (DAQ). This depletion region does not extend all the way to the surface, and the p^+ and n^+ layers constitute a “dead” region in which kinetic energy deposited in interactions within these regions is not registered.

Thick Contact The n^+ contact is created by evaporating and diffusing lithium into the detector surface. This surface is typically $\sim 500\ \mu$m thick and is “ruggedized,” i.e. it can be easily handled without too much fear of damage to the crystal surface.

Thin Contact The p^+ contact is produced by implanting boron ions, accelerated to a

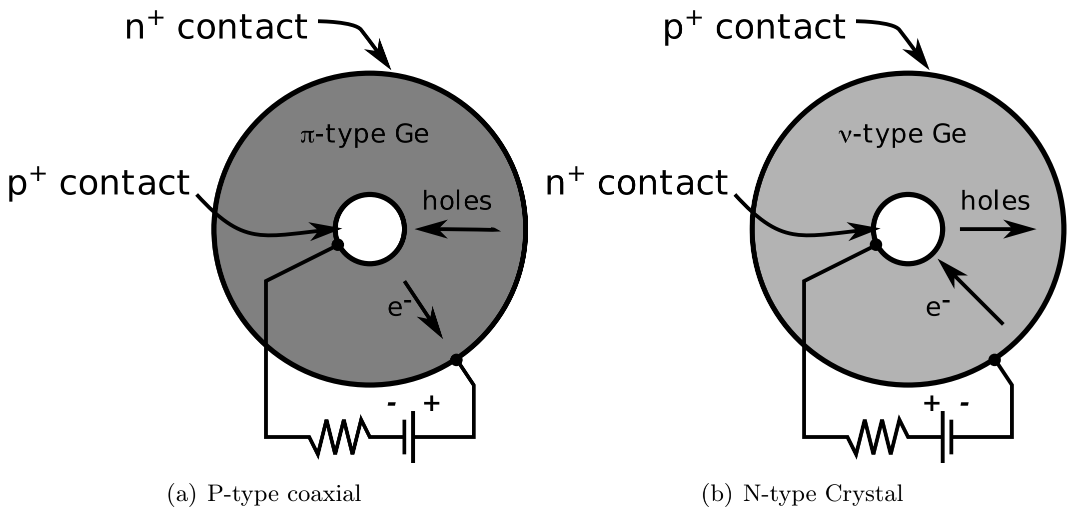

Figure 2.1: Circuit schematic showing electrical contacts for a P-type (a) and an N-type (b) detector. Figure modified from [32].

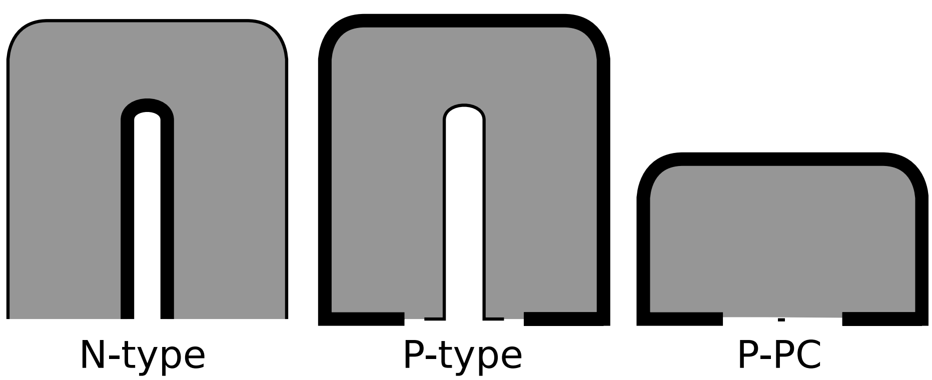

Figure 2.2: Cartoon of surface layout of different detector types. The thin black lines correspond to the p^+, or "thin" dead layer (0.3 μm). The thick lines are the n^+ layer, or "thick" dead layer ($\sim 500\mu$m). The areas at the bottom of the crystal separating the n^+ and p$^+$ contacts are passivated and are represented without any outline.

kinetic energy of 20 keV, into the surface of the crystal. Such contacts are only a few tenths of a micrometer in thickness.

Passivated Surface The region of surface between the p^+ and n^+ region is typically passivated to insulate the two contacts, often with GeO_2 [32]. The depth of this layer is $\sim 0.1\ \mu$m, although this region is also characterized by incomplete charge collection[33].

These dead regions are important for alpha backgrounds. First, alphas can lose energy within the p^+ (thin) layer and still make it into the active region of the crystal. The range of a 5.3 MeV α (e.g. from ^{210}Po) is $\sim 20\mu$m in Ge, and the range of an 8.8 MeV α (from ^{212}Po, the highest energy α in the U and Th decay chains) in Ge is $\sim 40\mu$m. Second, the thick dead layer of an HPGe detector is $\sim 500\ \mu$m and alphas cannot traverse this thick n^+ layer. In this sense, the n^+ surface is also ruggedized against alpha backgrounds.

2.1.2 Detector Types

There are two types of HPGe detectors: N-type and P-type. These are named from the intrinsic charge carrier concentration within the Ge. Figure 2.1 shows the two types as coaxial detectors, with the proper bias signs and carrier mobility directions indicated. The outer layer is the blocking contact, N-type detectors have the p^+ contact on the outside, while P-type detectors have the n^+ contact on the outside. Figure 2.2 is a cartoon showing examples of semi-coaxial N-type and P-type detectors with typical dimensions. HPGe detectors are made in coaxial and semi-coaxial geometries to take advantage of the uniformity of electric field lines between the outer surface and the inner core. The surface thickness in the cartoon is exaggerated to demonstrate the surface types. The thick, ruggedized n^+ layer, being 0.5 mm in depth, makes up nearly all of the P-type surface area, but only the inner core of the N-type detector. The N-type has mostly p^+ surface area. Recently, a modified P-type detector has become more widely used, in which the inner contact has been shrunk to the size of a small "point" (a typical size is 5 mm in diameter). This modification would normally affect the internal electric field so as to cause charge trapping, but the impurity gradient within the crystal is also modified to avoid this. The thick, outer surface on the P-type and P-PC detectors wraps around the bottom and inward, providing even more protection against alphas. The surface area between the p^+ and n^+ surfaces is the passivated region. For P-types, this region is confined to a small, annular ditch on the bottom of the crystal, whereas the entire bottom portion is passivated for N-types. For P-PC detectors, specifically the modified BEGe detectors from US Canberra used in the MAJORANA DEMONSTRATOR, this region consists of an annular ditch and the annular area on the bottom of the crystal not covered by the point contact. This region is typified by incomplete charge collection. The p^+ area also contains a metallized surface layer, consisting of 300 Å of gold (0.03 μm).

2.2 Energy-Loss Mechanisms for Alphas

To deposit 2039 keV in an HPGe detector, an alpha must lose multiple MeV's of kinetic energy before entering the active region. The ways this can happen can be organized into two categories: surface-alpha events and external-bulk alpha events.

2.2.1 Surface Alphas: Daughters of Radon

Surface-type alpha events are characterized by decays at the surface of the crystal, with energy loss happening only within a dead region inside the crystal. Only alphas at extremely shallow incidence angles (thus traveling through more dead region) will lose an appreciable amount of energy within this region; most deposit nearly all of their energy within the active region of the crystal, resulting in a peak structure when measured by the detector. The classic example of this background arises from exposure of ^{222}Rn (a noble gas). The decay of ^{222}Rn (3.8 day half-life) and its subsequent daughters ^{218}Po, ^{214}Pb, ^{214}Bi, ^{214}Po eventually lead to ^{210}Pb. Along the way, these daughters of ^{222}Rn can implant onto surfaces[34]. ^{210}Pb decays to ^{210}Bi, and then ^{210}Po, which emits a 5.3 MeV alpha upon its decay. The relatively-long half-life of ^{210}Pb (22 years) means that even a brief exposure of a detector or its surroundings can lead to a steady supply of 5.3 MeV alpha backgrounds[35, 34].

The susceptibility of an HPGe detector to surface alphas depends upon the size, type, and configuration of the detector. HPGe detectors can range from 10's of g to 2 kg. Table 2.1 shows three types of detector — N-types, P-types, and P-PC — in terms of mass and surface area. To compare different styles of detectors, a factor, λ, is defined as the ratio of

Table 2.1: Surface areas broken down by surface type for a typical N- and P-type detector, and the P-PC used in the Majorana Demonstrator

Detector Type	Mass	Surface Area [cm^2]				λ
	[kg]	passivated	p^+	n^+	Total	[cm^2/kg]
N-Type	1.1	30.4	177.5	31.8	239.7	161.4
P-Type	1.1	1.8	35.4	202.6	239.8	32.2
P-PC	0.579	1.9	0.2	104.5	105.6	0.35

p^+ area to mass. This number serves as a susceptibility factor to surface alpha backgrounds and provides a method of direct comparison between different detector types.

2.2.2 Alphas from Bulk Materials

The other category of alpha backgrounds, external-bulk type events, originate in bulk materials external to the crystal, e.g. a contact pin or detector mount. Energy loss of the alpha occurs in this bulk material before it hits the detector surface and depends on the amount of external material the alpha travels through. The result is a broad continuum of events with no alpha-peak structure.

2.3 Simulation and Experimental Path Forward

The rest of this dissertation addresses this question: how will the backgrounds associated with alpha decays impact $0\nu\beta\beta$ experiments using HPGe detectors? The answer to this question requires several steps. Simulations are used to determine efficiencies for alpha decays to populate the $0\nu\beta\beta$ region of interest (ROI, 1.3.1) for different detector types and energy-degradation mechanisms (Chapter 3). A separate analytic model is also constructed for the same purpose and to provide a separate predictive strategy (Chapter 5). These two models are compared with data from a test stand that was built to characterize the HPGe detector response to alpha decays (5). Thirdly, background data from a low-background, underground HPGe detector is analyzed with respect to alpha backgrounds (Chapter 6). Finally, a correspondence between alpha activity and backgrounds is established, and expected background rates for alpha activity are compared with the Majorana Demonstrator background model (Chapter 7).

Chapter 3

ALPHA SIMULATIONS

The MAJORANA background model relies on efficiencies of a given background decay to deposit energy in the region of interest (ROI). This often requires the use of simulation to perform a Monte Carlo calculation. This chapter details simulation work that has been performed for estimating surface alpha backgrounds.

3.1 MaGe: A Monte-Carlo Package for the Majorana and GERDA collaborations

The current round of $0\nu\beta\beta$ experiments using ^{76}Ge as target isotope (MAJORANA and GERDA) will be using $\sim$ 100 kg of material. Due to the costly nature of experiments such as this, it is expected that the next generation would be a single, international, tonne-scale experiment. With this in mind, MAJORANA and GERDA have agreed to merge in the not-too-distant future to combine resources and experiences in the pursuit of such a tonne-scale experiment. The first fruits of this cooperative agreement have already borne fruit, as both collaborations decided in 2004 to share Monte Carlo code. Both collaborations contribute to MaGe, a simulation package based upon Geant4 and ROOT libraries. Both collaborations are ^{76}Ge experiments and therefore share common simulation needs.

3.1.1 MaGe Overview

MaGe is built upon the Geant4 framework [36], an object-oriented set of libraries used to simulate the physics of particles interacting with material in detector geometries. A typical Geant4 program (executable) requires a geometry (the world, shapes, and materials in which the relevant simulation will take place), a generator (an initial particle with an initial momentum), and a physics list (detailing the particular interactions that the simulation will keep track of). These three inputs are required for a Geant4 program to compile:

Geometry – the physical layout of the experiment. The geometry includes the physical dimensions of objects (described using the `G4VSolid` class), the arrangement and nesting of objects (via the `G4VPhysicalVolume` or its derived `G4PVPlacement` class), and the makeup / material / density of objects (`G4LogicalVolume`).

Generator – i.e. the "particle gun." The generator is responsible for creating an initial (or set of initial) particles with initial (4) momenta. The particle then traverses the geometry, subject to interactions as specified in the physics list.

Physics list – details how the particle will interact with its surroundings. The physics list ties the traveling particle to the geometry that it is passing through. Examples of this include electromagnetic interactions for charged particles and gammas, or radioactive decay for heavier isotopes.

A fourth category, while not strictly required by Geant4, is useful for actually extracting information from a simulation:

Event-Action Class – allowing access to the event. An event-action class allows the recording of any and all information generated during an event, including energy deposit(s), position and momentum information for each particle, and the physical processes enacted.

A usual Geant4 program includes only one geometry, one physics list, one generator, etc... MaGe is different in this respect, in that it incorporates many different choices of input into a single executable package. It currently bundles more than 70 geometry classes, 50 event-action classes, and 50 generators. The choice of each input type is left to a user, and is enabled via macro commands.

3.2 Alpha Simulations in MaGe

Simulations were used at several points in studying alpha decays as backgrounds for $0\nu\beta\beta$ in HPGe detectors. Specifically, alpha simulations were used to quantify the amount

Table 3.1: Efficiencies for a surface alpha (5.3 MeV) to deposit between 2037 and 2041 keV of energy within a detector, for various simulated dead layers around the nominal 0.3 μm.

Dead Layer [μm]	Efficiency
0.28	$(1.04 \pm 0.05) \times 10^{-5}$
0.29	$(1.14 \pm 0.05) \times 10^{-5}$
0.30	$(1.16 \pm 0.05) \times 10^{-5}$
0.31	$(1.21 \pm 0.05) \times 10^{-5}$
0.32	$(1.27 \pm 0.05) \times 10^{-5}$

of alphas present in a detector (Chapter 6) as well as to predict the backgrounds to $0\nu\beta\beta$ (Chapter 7).

3.2.1 Dead-Layer Effects

The detector response to surface alphas is dependent upon the depth of the dead layer. As shown in Fig. 3.2, the amount of deposited kinetic energy of a surface alpha is dependent upon incidence angle. In particular, the loss of kinetic energy within the dead region only becomes appreciable above incidence angles of 80° or so. This is also dependent upon the depth of the dead region. Table 3.1 tabulates the efficiencies for a range of dead layers between 0.28 and 0.32 μm (centered around the nominal 0.3 μm).

3.2.2 Efficiencies for Time-Correlation Studies

A powerful tool for analyzing event information makes use of the characteristic decay times of successive particles in the ^{238}U and ^{232}Th decay chains. Just as the efficiency for a background decay to be observed by the detector is a function of placement, so is the efficiency for measuring two such decays. An alpha decay within an HPGe crystal would have an efficiency of 100%, while a decay at the surface would have an efficiency somewhat less than 50%. An alpha emitted within an external bulk material will have even less chance of making it into the active region of a crystal. The efficiency to measure two alphas within

Isotope	Energy (MeV)	Surface Efficiency
^{216}Po	6.778	0.488 ± 0.002
^{224}Ra	5.685 / 5.449	0.460 ± 0.002
^{222}Rn	5.489	0.484 ± 0.002
^{220}Rn	6.288	0.489 ± 0.002
^{214}Po	7.686	0.489 ± 0.002

Table 3.2: Efficiencies to measure surface alphas on a p^+ surface of an HPGe detector. These alphas are used in Chapter 6 in a timing-correlation analysis.

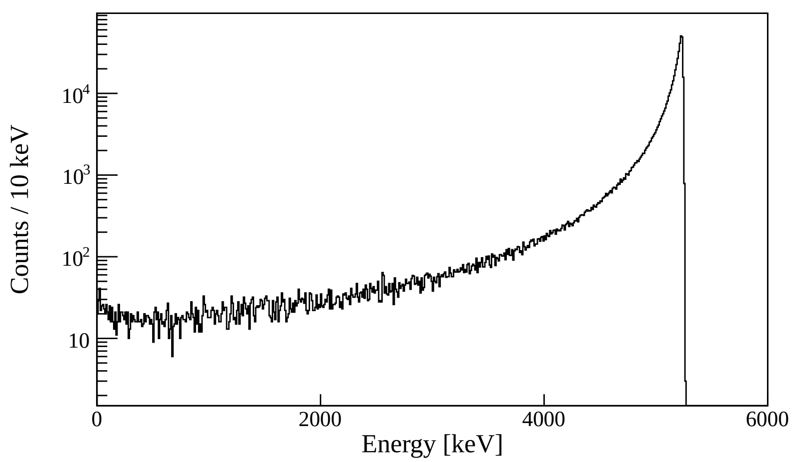

Figure 3.1: Simulated surface-alpha energy spectrum of 5.3 MeV energy alphas.

a short period of time should be the product of the two individual efficiencies[1]. MaGe was used to simulate the alphas in the ^{232}Th decay chain, decaying from the p^+ surface of an HPGe crystal. The calculated efficiencies for energy deposits greater than 2700 keV are tabulated in Table 3.2. As explained in Chapter 6, the number of counts below 2700 keV makes a coincidence analysis like this impractical, and so a threshold cut of 2700 keV was established to look for double events at higher energies.

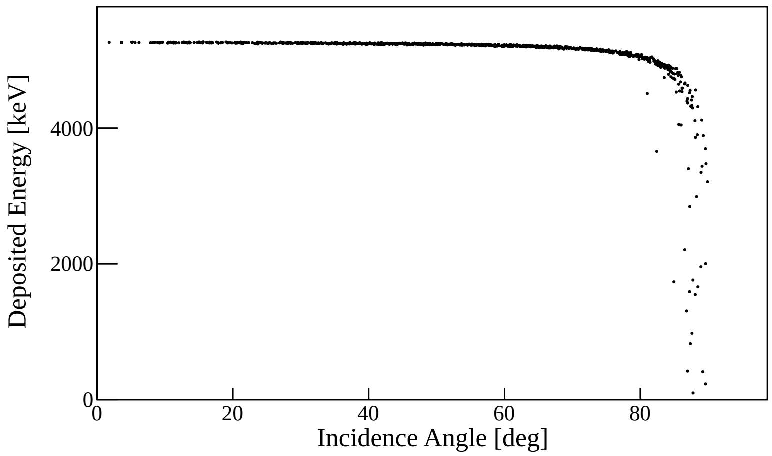

Figure 3.2: Relationship between incidence angle and deposited energy of a 5.3 MeV surface alpha.

3.2.3 Efficiencies for the $0\nu\beta\beta$ ROI

Simulations were performed to establish the likelihood that a decay of an alpha-emitter on the surface of an HPGe crystal — ^{210}Po for example — would result in a background count in the region of interest around 2039 keV. Isotopes of ^{210}Po were simulated on the p^+ surface of an HPGe detector and allowed to decay, using Geant4's `G4GeneralParticleSource` class[37]. The energy spectrum is shown in Fig. 3.1. The resultant 5.3 MeV alpha is emitted isotropically in 4π. Of the half that enter the crystal, most will pass through the dead layer with a minimum of energy loss and therefore will deposit most of their energy in the crystal. At higher incidence angles (with respect to the normal), the alpha loses more and more energy within the dead region. Figure 3.2 shows the relation between deposited alpha energy and incidence angle for a simulated 5.3 MeV surface alpha. The dead layer used in this simulation was 0.3 μm.

[1] There is a small correction due to the deadtime inherent in measuring the first event, and this is discussed in Chapter 6.

Chapter 4

ACQUISITION AND ANALYSIS OF HPGE DETECTOR DATA

Alpha data were taken on two separate detector systems, one located underground at WIPP (an N-type detector, named WIPPn, Chapter 6) and the other located at Los Alamos National Laboratory (a Surface Alpha N-type Testing Apparatus, or the SANTA detector, Chapter 5). This chapter describes the detector and acquisition hardware setups and the software tools used in analyzing alpha data. The specifics related to the two detectors are detailed in Chapters 6 and 5. While they were manufactured by different companies (Princeton-Gamma Tech for WIPPn, ORTEC for SANTA), their operation and data acquisition are quite similar, and one set of software tools was designed to handle the different analyses for both systems.

4.1 Data acquisition

The WIPPn detector, located underground at the Waste Isolation Pilot Plant (WIPP), is operated remotely via secure connection to the WIPP subnet. The liquid nitrogen level is monitored by a fill probe and liquid level controller from American Magnetics Inc. (Model 186 Liquid Level Controller). A liquid nitrogen (LN) fill monitor probe is inserted into the detector's dewar and connected to an automatic-fill system. Preamp power, high-voltage bias, and digitization of the analog preamp output is all provided by the Polaris DGF (Digital Gamma Finder), manufactured by XIA LLC (formerly X-ray Instrumentation Associates). The Polaris interfaces with a laptop running Windows 2000 via a USB connection. The interface is controlled by a proprietary program, written in Igor Pro by XIA. The remote connection allows for runs to be started and stopped, data acquisition parameters to be set, and run data to be transferred offsite. Fig. 4.1(a) shows the data acquisition chain for the WIPPn detector.

The SANTA detector, built and run at Los Alamos National Lab, is operated on-site

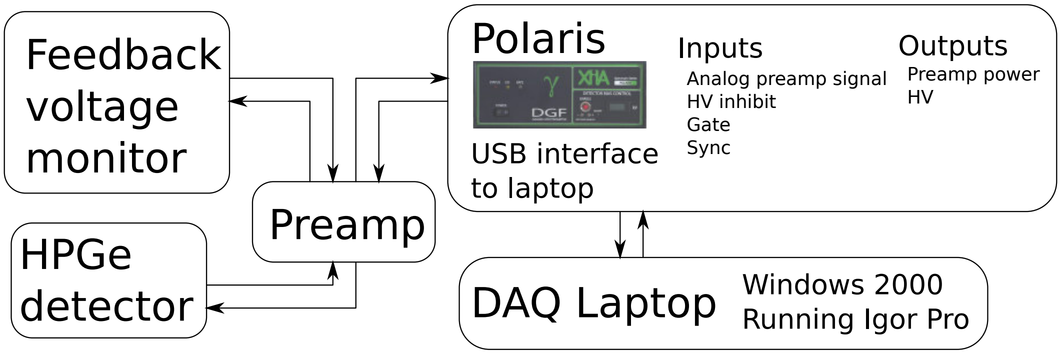

(a) Polaris data-acquisition chain

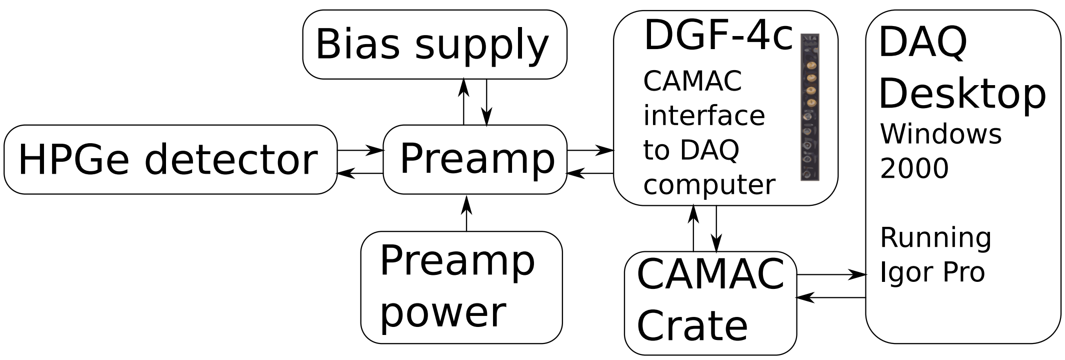

(b) DGF-4c data-acquisition chain

Figure 4.1: Data acquisition chain for the two detector systems. The WIPPn detector is located underground at WIPP and digitized by the Polaris. The SANTA detector is located at LANL and digitized by the DGF-4c.

at LANL. The detector's dewar is manually filled with LN on an as-needed basis. High-voltage is supplied by an ORTEC 660 Dual Channel 5 kV bias supply (only one channel is used). Power for the preamp is supplied by an ORTEC 672 Spectroscopy Amplifier module. Digitization was performed by a DGF-4c, a CAMAC-based digitizer card manufactured by XIA. The CAMAC crate connects to a DAQ computer, running Windows 2000, via a CAMAC PCI card. An Igor PRO-based program interfaces with the digitizer. This program was written by XIA and is similar to the one that runs the WIPPn detector. The DAQ chain for the SANTA detector is schematically drawn in Fig. 4.1(b).

Aside from the built-in bias supply and the USB connection, the Polaris is very similar to the DGF-4c. The internal shaping and event discrimination parameters are identical. Both can be run in MCA mode (histogram) or in full event mode (record full event information such as event time and waveform). The event-mode data binary files written by the two Igor PRO programs have an identical format and the control software is similar. The DGF-4c has 4 input channels and can also be run in more restricted event modes, recording energy and time stamps, but not full waveforms. In this document, *MCA mode* is the energy histogram mode, *event mode* is any mode where information for each event is recorded. *Event mode* can either be *list mode*, where only energies and time stamps are recorded, or *waveform mode*, where the waveform ADC values are recorded in addition to the *list-mode* data.

Within this chapter, it should be understood that references to *the DGF* apply to the behavior of both the DGF-4c and the Polaris. The text will refer to either the DGF-4c or the Polaris in cases that are unique to that particular system.

4.2 Data pre-processing

Data acquisition with the DGF (for the SANTA and WIPPn detectors) is fundamentally different than acquisition for the rest of the Majorana Collaboration. The Majorana Collaboration is using ORCA (Object-oriented Real-time Control and Acquisition) [38] for data acquisition, and much of the software analysis efforts are pushed at that format. The ORCA file format records, in addition to the data, a bevy of meta-data such as run-start time, crate and card information, and livetime. A complementary software package, OrcaROOT, was written to process ORCA files, extract the binary data and meta-data, and store the results in ROOT files as histograms (`TH1D`) and trees (`TTree`). The end result of the ORCA→OrcaROOT process is a ROOT file with a `TTree` of data objects, each entry in the `TTree` encapsulating all of the relevant information for a particular physics event (energy, time stamp, hit pattern, etc...). This data object inherits from MGDO (Majorana-GERDA Data Object), a set of libraries designed to provide an encapsulation of data for data analysis. This same format is also used for simulated data, allowing data and simulation to be treated on the same footing. MGDO is developed jointly by the Majorana and GERDA collaborations.

The complexity of the XIA-DGF series of digitizers has hampered efforts toward a reliable ORCA implementation for that family of digitizers. Hence, the data from the WIPPn and

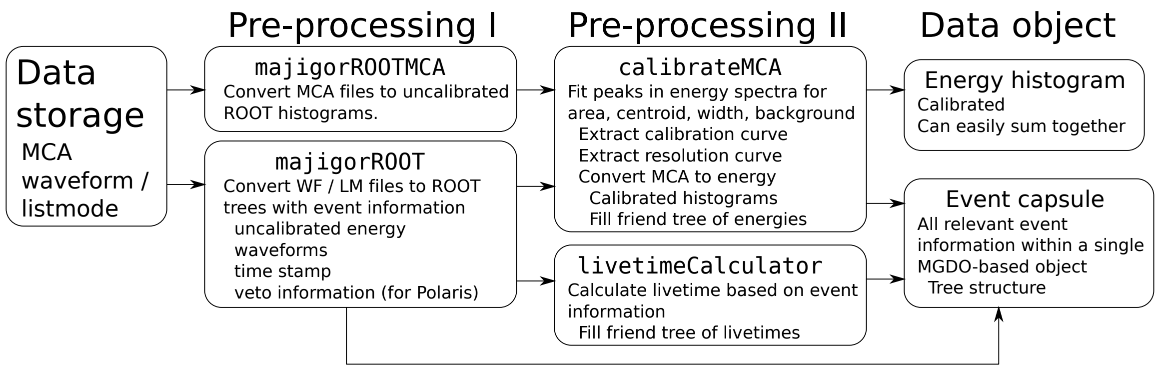

Figure 4.2: Data pre-processing chain for the DGF Polaris and DGF-4c digitizers. The programs `majigorROOTMCA`, `majigorROOT`, `calibrateMCA`, and `livetimeCalculator` are written in a combination of C^{++} and Python, with Python also used to control and direct the input/output of each individual program. The chain processes Igor DGF binaries into ROOT files with calibrated energy histograms and ROOT trees of encapsulated event information.

SANTA detectors were taken with the Windows-based Igor program provided by XIA. One issue that arises from this is translating Igor binary data files into ROOT-readable files that are ready for further analysis. The binary data files themselves do not contain meta-data from the run, but that data is recorded manually in the respective experiment log books and also in separate files written upon completion of a run by Igor Pro. A suite of programs were developed to convert the raw Igor binary files into ROOT files with encapsulated event information. This pre-processing chain is shown in Fig. 4.2.

4.2.1 Pre-processing I: Igor binary to ROOT conversion

Each of the DGF systems creates so-called MCA histogram files. These binary files are packed with 32-bit words, each word corresponding to an MCA bin with a maximum of $2^{32} \sim 4.29 \times 10^6$ counts/bin. The DGF-4c MCA files always have 32K word records per file (file size = 131072 bytes), while the Polaris can record histograms with a variable number of bins (from 2^{10}–2^{16}, or 1024–65536). The Polaris was always run utilizing 65536 bins (file size = 262144 bytes). The full pulse-shape mode is identical for both, with 16-bit words packed into buffers. The first six words of a buffer or “spill” constitute a buffer header. Events are packed in after the buffer header, each event beginning with a three word event header.

Table 4.1: Comparison of detector acquisition for the WIPPn detector and SANTA. Descriptions marked with a † are only used by the DGF-4c, while those marked with a ‡ are only used by the Polaris. Words marked with a * are not use by either system.

Buffer Header Words		Event Header Words		Channel Header Words	
0	No. of words in buffer	0	Hit pattern†	0	No. of words for this channel
1	Module No.†	1	Event time (mid)	1	Channel time (low)
2	Run format	2	Event time (low)	2	Energy
3	Buffer time (high)			3	XIA Pulse-Shape value*
4	Buffer time (mid)			4	User Pulse-Shape value*
5	Buffer time (low)			5	Unused
				6	Unused
				7	Veto hit‡
				8	Channel time (high)

This is then followed by blocks of channel data (one block for the Polaris's one channel and a possibility of one to four blocks for the DGF-4c, depending on how many channels are in use). Each channel block starts with a header — composed of nine words — followed by words corresponding to the ADC values from the channel waveform. The buffer, event, and channel words are defined as in Table 4.1, and a graphical representation of the packing structure is shown in Fig. 4.3. While the Polaris has only MCA mode and full waveform mode, the DGF-4c can also run in "list-mode," where the event and channel headers are recorded but not the full waveform. Regardless of the format, the buffers for list-mode / pulse-shape files include 8102 words, and so the number of events per buffer depends on the length of the waveform and how many channels are recorded (for the DGF-4c). Each digitizer samples at 40 MHz, so each waveform word corresponds to a 25 ns clock tick. Waveforms recorded for WIPPn and SANTA were 2.5 μs long, or 100 words.

The OrcaROOT libraries were used as a starting point for developing an offshoot for the pre-processing of Igor binaries (a branch, in revision control speak). This branch, named IgorROOT, utilized a separate file reading function that was written to parse the Igor binary information into the same format as ORCA. The same processing and output functions as OrcaROOT were then used. Two programs were written to directly convert an XIA-DGF binary into a ROOT file. `majigorrootMCA` reads in any number of MCA binary files,

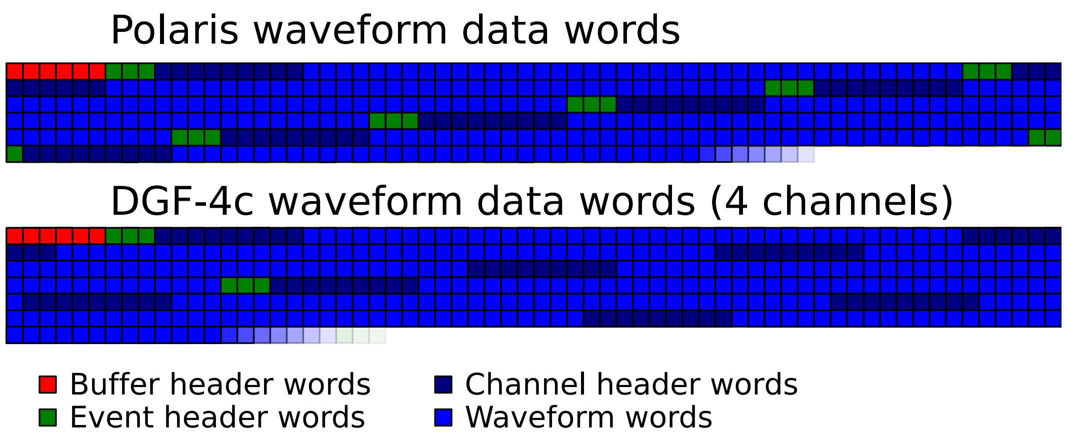

Figure 4.3: Cartoon representing packing of 16-bit words in a buffer by the DGF Polaris (1 channel) and the DGF-4c (4 channel). Only the first few events are shown (in this case there are seven one-channel events for the Polaris and two four-channel events for the DGF-4c). The number of words in the buffer, event, and channel headers is always 6, 3, and 9 respectively for data discussed in this work. The number of words in the waveform depends on the length of pulse that is recorded. Descriptions of what each word in the buffer,event, and channel headers are in Table 4.1. Each buffer is 8102 words long, so the number of events depends on the number of channels written (for the DGF-4c) and the waveform length.

converts the runs into `TH1D` histograms, and saves the histograms to an output ROOT file. `majigorroot` reads in a list-mode or pulse-shape binary, extracts the header and any waveform data from each channel hit, and stores it as an entry in a `TTree`. The DGF-4c, having 4 separate channels, is capable of recognizing hits in separate channels that are coincident in time as belonging to the same event. `majigorroot` will write each channel hit as its own event, also noting the channel number and event number. The SANTA detector was only run in single-channel mode, so each event corresponds to a single-channel hit and the coincident-event feature was not used. A separate table of runs, with entries for filename and start/stop date, was kept as a `.txt` file. The program `majigorroot` checks this table, checks for the existence of the current run in the table, and fills in the date information as an entry in the `TTree`. `majigorroot` is based upon `majorcaroot`, an OrcaROOT application that extracts data from a Gretina digitizer card into similar encapsulated trees.

The resultant ROOT files now serve as complete records of the data. Further pre-processing and analysis will act on these files, while the original binaries are kept safely untouched in a separate write-restricted directory.

4.2.2 DGF event-mode data

The DGF-Polaris system for the WIPPn detector was operated in MCA-mode only in 2006, recording only histograms. Starting in January, 2007, the Polaris was run in waveform mode, recording event and waveform information. It continued recording in this mode until March, 2007, when the Polaris system crashed and had to be sent back to XIA. The system was up and running again in May, 2007, and has since then been run exclusively in waveform mode. This mode also produces an MCA file, storing just the MCA spectrum. Running the DGF in event mode has significant advantages over the simple MCA mode, for analysis of both waveforms (pulse-shape analysis) and event data (energy, time stamps, veto stamp). The energy for the event-mode data is calculated by the DGF using the same trapezoidal filter as for MCA mode, and this has been verified by comparing the MCA spectrum from that of the event mode file. The drawbacks of running in waveform mode are increased file sizes and increased dead time. These drawbacks were easily overlooked for the WIPPn detector, due to its low event rate. These drawbacks were not negligible for the SANTA detector, where the large background creates very large data sets and the actual duty cycle of data taking is a much-smaller fraction than for WIPPn.

The DGF does not write a single "time stamp" for each event. Instead, there are seven separate 16-bit words written in the buffer, event, and channel headers that can be combined to form different time stamps. Each word corresponds either to a "low," "middle," or "high" word, and three of the words can be concatenated into a 48-bit number that maps to the DGF's internal clock. Each increment in this number signifies a 25 ns clock "tick" (40 MHz sampling). Hence, the low word rolls over every $2^{16} \cdot 25\text{ns} \sim 1.639$ ms. Similarly, the middle word rolls over every $2^{32} \cdot 25$ ns ~ 107.37 s, and the high word every $2^{48} \cdot 25$ ns ~ 703687 s, or 81.45 days. As shown in Table 4.1, the timing words are split up amongst the buffer, event, and channel headers, and the different combinations of mixing low, middle, and high words give slightly different time stamps:

Buffer Time: consists of the three buffer-time words. This time represents when the current buffer began.

Buffer-Event-Channel Time: consists of the buffer high word, the event middle word, and the channel low word. Subject to inaccuracies (see text)

Event Time: consists of the two event-time words (low and middle) and the high-channel word.

Channel Time: or channel-event time, consists of the channel low word, the event middle word, and the channel high word. This is only different than the event time if the DGF has multiple channels (as in the DGF-4c) and triggers from multiple channels are processed in the same event.

A problem with the DGF Polaris software was noticed in June, 2007. All of the timing words were being written correctly *except* the channel high word and the buffer low word. The buffer low word is only used for the buffer time stamp, and its loss means the buffer time is only known to within 1.64 ms. The loss of the channel high word is more problematic. While high event-rate systems might be able to use the buffer high word as a substitute, the WIPPn detector has a low-enough count rate that ensures that middle-word rollovers (every 107 seconds) will occur quite often between two events. Thus, the time stamp of any given event might be off by 107 seconds when using the buffer high word for an event time stamp. This firmware issue was raised with XIA, and a subsequent version had fixed the problem. Event-mode data taken since November, 2007 includes the correct, useful time stamp. This was not an issue for the DGF-4c.

Word #7 in the channel buffer of the DGF Polaris event-mode data is a veto flag. The Polaris includes a veto GATE BNC input, designed for the current output of a PMT. If a GATE pulse occurs within 1 μs of an event, the DGF tags the event with a veto flag. The original software did not include this event-by-event veto flag, and instead simply vetoed the event outright and did not write it to disk. Through conversations with XIA, we were able to convince them to implement the event-by-event feature. The new software from XIA was installed for the Polaris at WIPP in December, 2008. This should have allowed a “flag-veto” setting, placing a "1" in the at channel word #7 if a veto signal was detected, and a "0" otherwise. It was found that rather than simply flagging the event, it was also setting the energy to zero. Subsequent conversations with XIA resulted in a software upgrade, fixing the problem. This was installed in January, 2009, and veto-flag data were collected between 5 January, 2009 and 19 February, 2009. At that time, a reboot of the Polaris resulted in a use of the previous software (with energies of flagged events set to zero). While inconvenient, there is a work-around to recover the energies of the "lost" events. Only the energy of the lost events was set to zero. The rest of the event information was recorded, including the waveform data.

To calculate the energy of an event, the DGF applies a trapezoidal filter to the ADC values of the charge pulse. The simplest trapezoidal filter is characterized by two parameters, a length L and a gap G[1]. The trapezoidal filter transform acts on a waveform (let V_k be the value of the kth point), producing a trapezoid-shaped peak. The height of this peak is proportional to the height of the pulse (and therefore the amount of energy deposited in the crystal). The output waveform is calculated via

$$LV_k = -\sum_{i=k-2L-G+1}^{k-L-G} V_i + \sum_{i=k-L+1}^{k} V_i. \tag{4.1}$$

Each output point V_k is the difference of two averaged regions of length L, separated by the gap G. More complicated versions of the filter incorporate weights to the summed values, but the DGF uses Eq. 4.1 [39].

Applying the same trapezoidal filter as the DGF to the recorded waveforms should reproduce the same calculated energies (with a multiplicative factor). This turns out not to be the case, as the stored waveforms from the WIPPn detector are only 2 μs long, while the DGF calculates the energy using the entire trace in FIFO memory[2]. The filter used by the DGF for energy resolution uses a length $L = 1.2\mu$s (48 clock ticks) and a gap $G = 0.35\mu$s

[1]Actually, the *simplest* trapezoidal filter is only characterized by L, with G is set to zero. This is a triangular filter.

[2]The FIFO buffer is 4096 words long, or 100 μs of trace. This can all be recorded, but requires significantly more hard drive space to store data files. We did not envision having to redo the energy calculations off-line and the 2 μs trace length is sufficient for pulse-shape studies

(14 clock ticks). For a waveform as in 4.4(a), the output of the filter transform gives 4.4(b). The peak height (proportional to the energy) is unknown because the filter settings are too wide for the trace length. Shortening the rise of the filter (e.g. setting $L = 0.35\mu$s) produces a valid output peak, but at the cost of energy resolution.

The question is, how well can we do in recovering the lost energy values? To answer this, a trapezoidal filter transform was applied to a data set from WIPPn. Waveforms from the dataset were first extracted from the data files. To apply the trapezoidal filter, transform modules from MGDO were used. A smoothing transform, `MGWFSavitzkyGolaySmoother`, was applied to the waveform, followed by a baseline remover, `MGWFBaselineRemover`. A trapezoidal filter transform, `MGWFTrapezoidalFilter`, was then applied to the resulting smoothed, baseline-subtracted waveform. Values of $L = 0.5\mu$s and $G = 0.35\mu$s were used in the transform. The resulting peak heights were stored in a `TTree` along with the energy values as calculated by the DGF (hereby denoted E_{X}). The energy values calculated by the trapezoidal filter (denoted $E_{\mathrm{T}F}$) were found by dividing the peak heights by a constant to bring the ratio $E_{\mathrm{T}F}/E_{\mathrm{X}} \simeq 1$. Figure 4.5 compares the two energies, first plotting the residual $(E_{\mathrm{T}F} - E_{\mathrm{X}})/E_{\mathrm{X}} = \Delta E/E$ against E_{X}, and then histogramming $\Delta E/E$. Agreement is extremely poor at lower energies, so an energy cut of $E_X > 100$ keV was instated. Above this, analyzing the histogrammed residuals reveals that 93.25% of events are within 1%, 98.31% are within 2%, and 99.48% are within 10%. While this would certainly not be sufficient for gamma peak spectroscopy, it is good enough for looking at the cosmic spectrum, as will be discussed in Section 6.3.1.

4.2.3 Pre-processing II: Calibration and livetime

Calibrations

The MCA spectrum — stored as `TH1D` histograms from an MCA file or filled into a `TH1D` histogram using `TTree::Draw()` from the event-mode files — represents an uncalibrated energy spectrum. Conversion of an MCA value, M, to an energy in keV, E, requires a calibration transformation using an N^{th} degree polynomial, i.e.

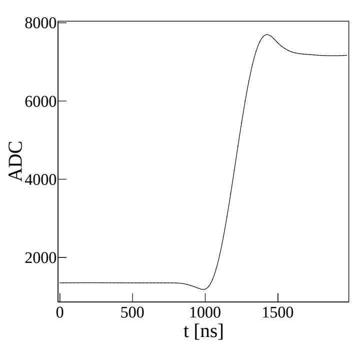

(a) Waveform with trace length $= 2\mu$s

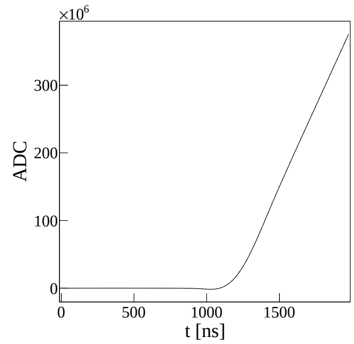

(b) Filter length too long

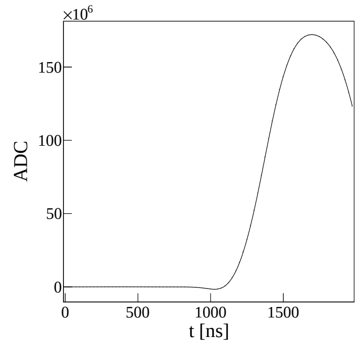

(c) Filter length short enough, but with poor energy resolution

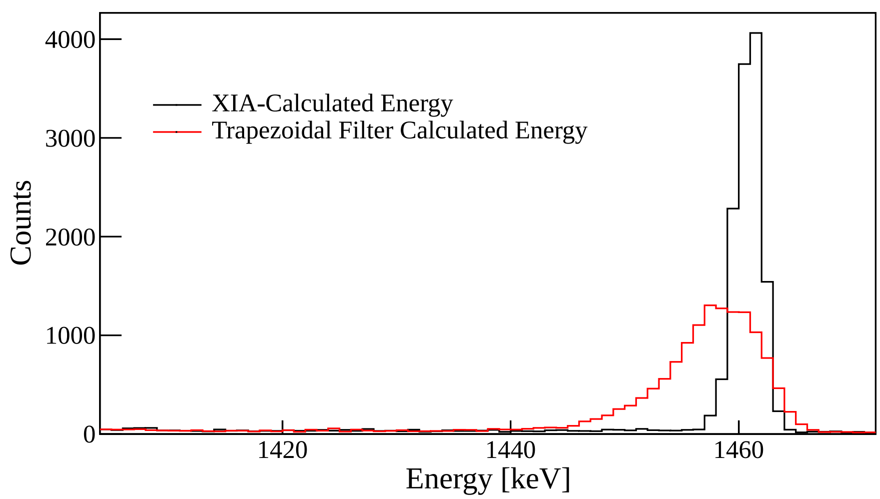

(d) Energy resolution comparison

Figure 4.4: The length of trace recorded (2μs) is insufficient to perform a proper offline trapezoidal filter energy measurement. The recorded waveform is shown in (a). The trapezoidal filter with values of $L = 1.2\mu$s and $G = 0.35\mu$s for the length and gap parameters, as used by the DGF during real-time processing, is shown in (b). The peak maximum is not even visible because the trace length is too short. (c) uses $L = 0.35\mu$s and $G = 0.35\mu$s. The trapezoidal filter output peak is visible, but the shorter shaping time results in poorer resolution (d).

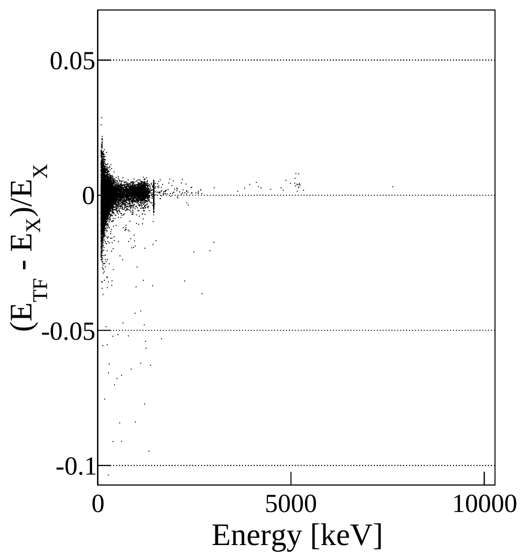

(a) Deviation by energy

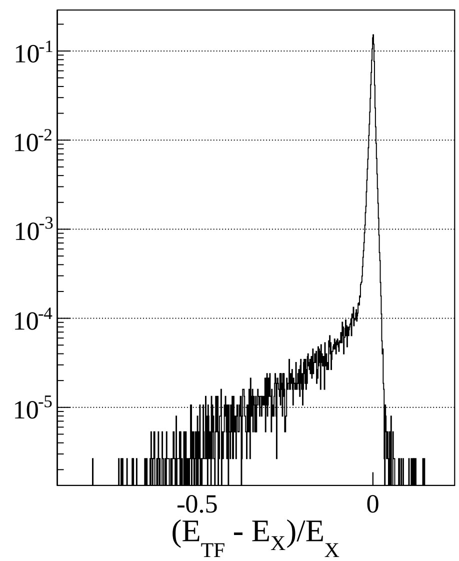

(b) Histogrammed deviations

Figure 4.5: Deviations of energy ($\Delta E/E$), comparing energy values calculated by the DGF and by trapezoidal filter.

$$E = \sum_{k=0}^{N} c_k M^k, \tag{4.2}$$

where the coefficients c_k are determined by a least-squares fit of gamma peak MCA centroids to known energy values. The measured centroid values either come from multiple background runs that have been summed together, or else from dedicated source runs. Source runs for both WIPPn and SANTA were performed by using a thoriated welding rod held adjacent to the detector's cryostat. In the case of WIPPn, this entailed removing a portion of the lead shield to set the rod placement.

Peaks are fit with a Gaussian + quadratic polynomial background in ROOT (Fig. 4.6). For a peak to be used for calibration, the fit must have a P-value higher than 0.05 and `MINUIT` must be able to calculate an accurate covariance matrix and exit with no warnings or errors. The MCA spectrum of an HPGe detector should be linear in energy. Any non-linearity in the system can be accommodated by a calibration function with polynomial terms of order

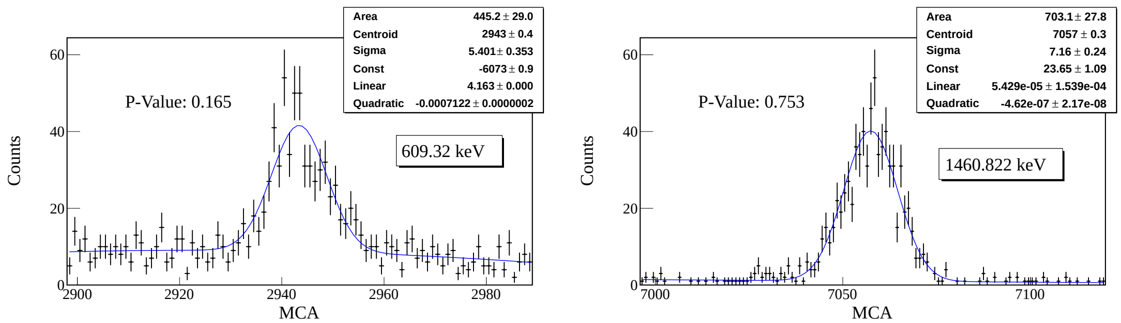

(a) (b)

Figure 4.6: Example fits to peak shapes in MCA data.

higher than 1 (see e.g., [32]). This is safe for extracting energies within the range of the calibration points (interpolation). The fitted peaks act as anchors in a sense, keeping the extracted energy value close to the true value. But this is not so safe for energies outside of this range; small deviations in a value that have negligible effect near the points (at lower energies) can cause drastic changes away from the calibrated points (at higher energies). The higher the polynomial order in the calibration curve, the greater this difference[3]. A representative example is shown in Fig. 4.7. This situation manifests itself when looking at alpha decays from ^{232}Th and ^{238}U. Alphas at these energies (3.9 - 8.8 MeV) are substantially higher than the highest energy gamma in the decay chains, 2614.51 keV from ^{208}Tl. The non-linearity of the detector and its calibration result in a small, systematic uncertainty (energy offset) for higher-energy events. This will be discussed in Section 6.3.

The gain of the Polaris is adjustable, and there have been several different gain settings used over the years. There are therefore several calibration conversion curves for this detector, depending on when data were taken. Even when gain settings are not changed, there is an observed "drift" in the MCA values. This is shown in Fig. 4.8. MCA histograms are summed together by month for runs between November, 2007 and February, 2009. The peak in the MCA spectrum corresponding to the 1460.82 keV gamma from ^{40}K is fit with the same `TF1` fit function as above. The centroids with associated errors are plotted as a

[3]To put it cartoonishly, adding higher terms adds wiggles, and those wiggles have to show up somewhere.

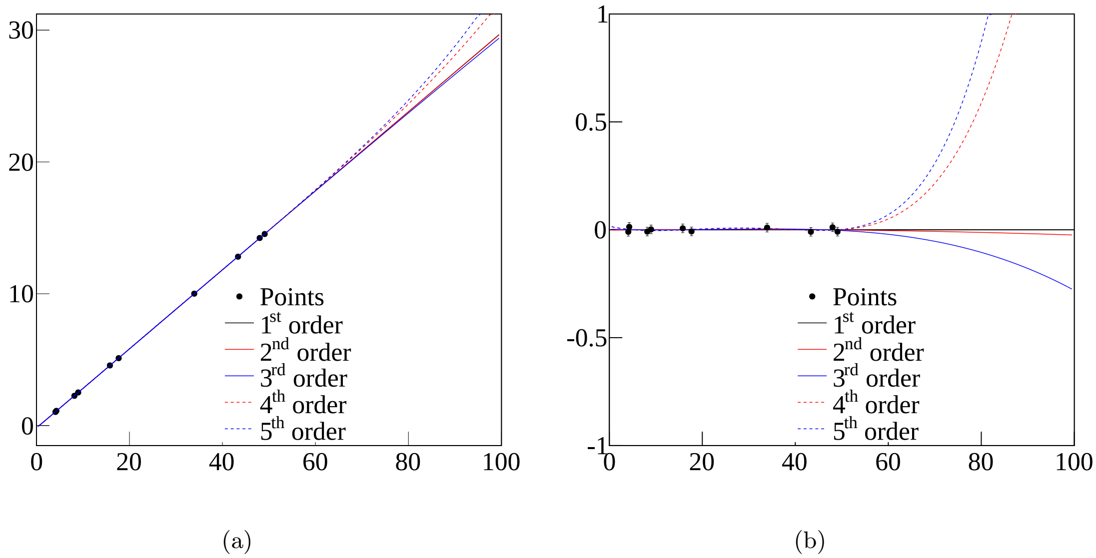

Figure 4.7: A toy simulation showing the danger of extrapolation. A dataset was generated from a linear polynomial with a small random offset added to each point. The dataset was then fit with a series of polynomials, of order 1–5. The polynomial functions never stray far from the points, but begin to diverge at higher x-values. (b) shows the fits with the linear fit subtracted from each polynomial and the data points.

function of time. There are large swings in the centroid value over periods of time which are small compared with source runs, so calibrations were performed for monthly-binned runs using the integrated MCA spectrum and background peaks. The observed drift remains unexplained.

Data from the WIPPn detector have been taken in both pulse-shape (full waveform) mode and in stand-alone MCA mode. The MCA spectra taken from the Igor MCA files (or the equivalent data from the waveform files) is in ADC units and must therefore be converted to an energy spectrum. A thoriated welding rod has been used intermittently for calibration source runs with the WIPPn detector since late 2006. The top of the lead shield is removed for these runs, and the rod is inserted adjacent to the detector's cryostat. Runs taken prior to the use of the thorium rod (Setup I and II in Table 6.2) can be summed and calibrated using the gamma lines that are naturally present in the background (from ^{238}U,

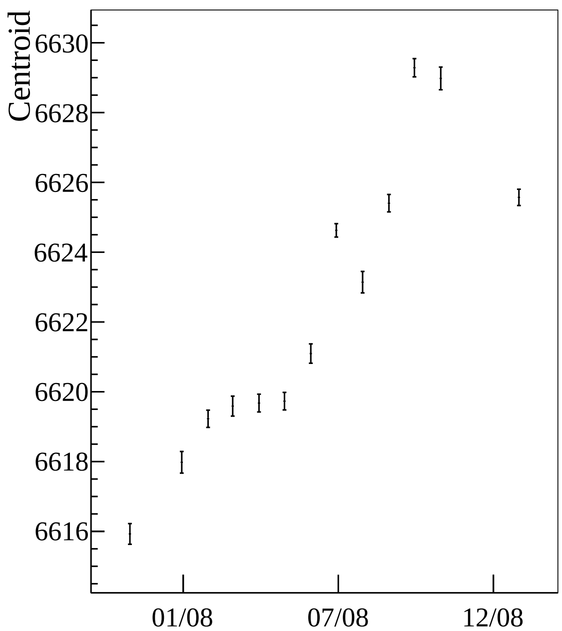

(a) Peak drift in the ^{40}K peak at 1460.8 keV

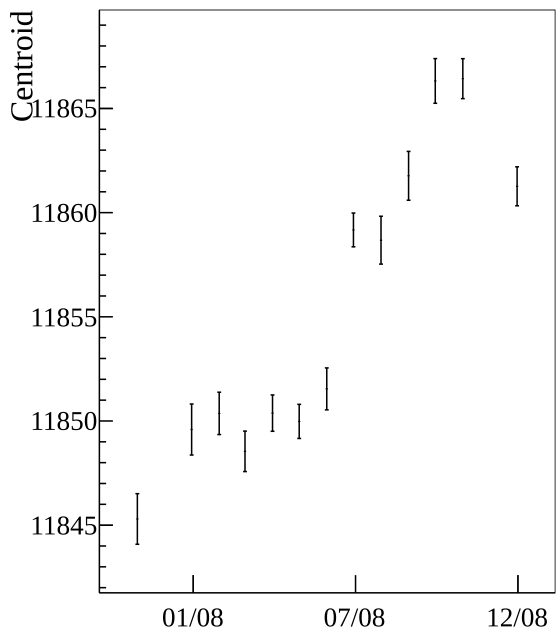

(b) Peak drift in the ^{208}Tl peak at 2614.5 keV

Figure 4.8: MCA centroids from the WIPPn detector, corresponding to the 1460.8 keV and 2614.5 keV peaks from ^{40}K and ^{208}Tl, plotted as a function of time. Runs were binned by month. As in all peak fits, values from a fit are only trusted if `MINUIT` returns an accurate covariance matrix with no errors.

^{232}Th, and ^{40}K). Peaks in the background spectrum are fitted with a `TF1` fitting function composed of a Gaussian peak and quadratic background. The fits extract the number of counts (signal and background), peak widths, centroids, and the significance and p-value of the fit. These values, as well as their associated errors, are stored in Python `pickle` files. Python's `pickle` format provides a useful, convenient method to organize and store data structures in a completely platform-independent, machine-readable format.

A Python/PyROOT module, `CalibrateMods.py`, and Python script, `calibrateMCA.py`, were written for the purpose of MCA spectrum calibration. The `CalibrateMods.py` module contains a list of known gamma peaks that are often used for calibration, where values for the energy centroids and uncertainties were taken from the Nuclear Data Sheets[40, 41, 42, 43, 44]. One of the arguments to `calibrateMCA.py` is a numerical "guess" for the linear calibration coefficient (c_1). The script reads in the desired MCA histogram and loops over its internal list of known gamma peaks. The guess is used to zoom in on the desired peak, and the script attempts a preliminary fit. The user then has control to set different limits, fix or free parameters, and in general make sure that the fit is satisfactory. The parameters of the fit are written (including the p-value) and the process is repeated for the next gamma line.

Once all peak fits are completed, all of the fit values are written to a `pickledIgorPeakFit` file. The gamma energies and errors can then be collated with the fitted peak centroids and uncertainties into a `TGraphErrors` object. The graph is fit with polynomials of order 1-5, and the best fit is used to obtain a calibration curve. As discussed above, the MCA output from the detector is linear, at least to first order. Using higher-order terms in the calibration curve will generally result in better fits, but the improved $\Delta\chi^2$ comes with the cost of an additional model parameter. Because these calibrations will be used to examine higher-energy data, the choice was made not to use a fitting polynomial higher than 2 to avoid problems with extrapolation. Examples of these polynomial fits to the peak centroids for two separate data sets are shown in Fig. 4.9 and Fig. 4.10, where the residuals are shown for polynomial fits order 1–6. The p-value, χ^2, and number of degrees of freedom are also shown for each fit. In both cases, a linear polynomial was chosen to represent the calibration curve.

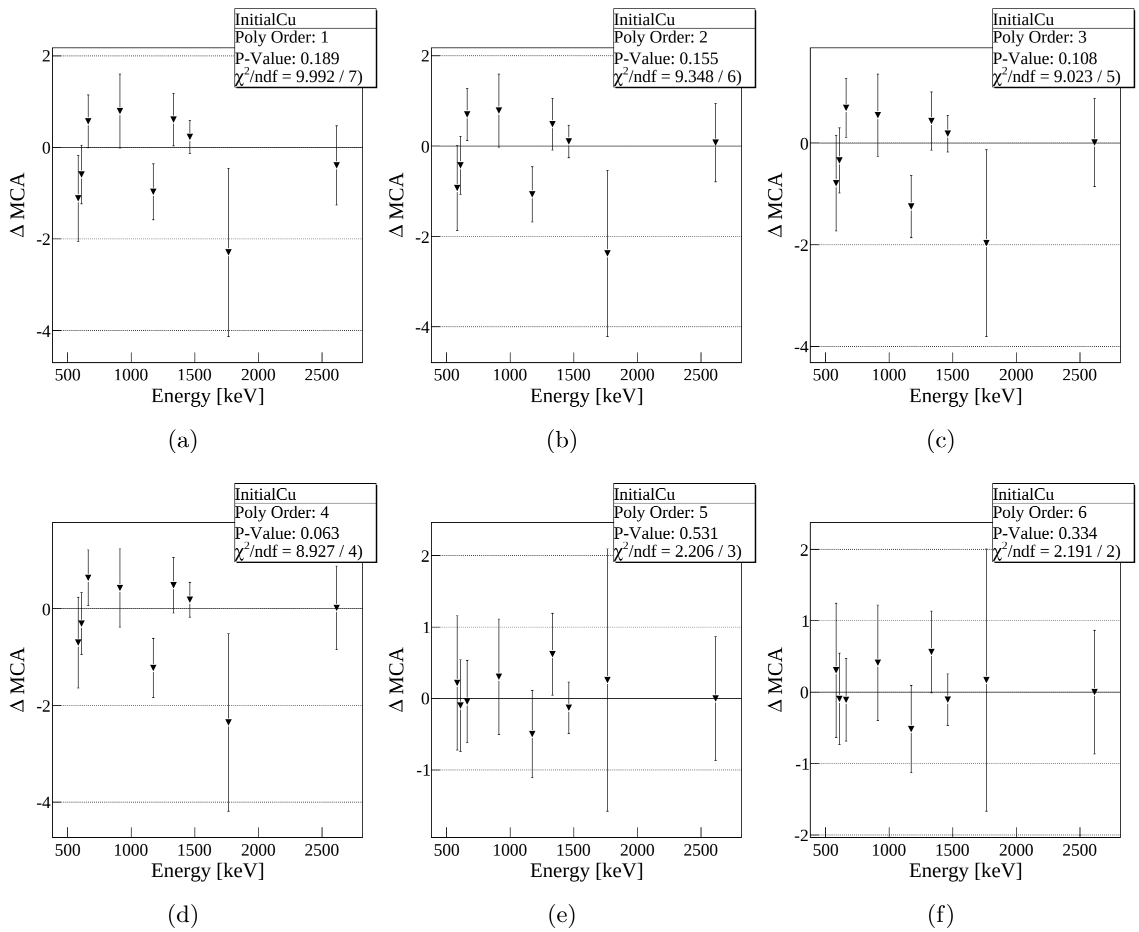

Figure 4.9: Polynomial fits to determine calibration coefficients. The centroids and errors of fitted peaks are plotted against their known energies and fitted with polynomials. The residuals of the fits are shown. In this case, there is no reason to choose a polynomial fit higher than order 1 (linear).

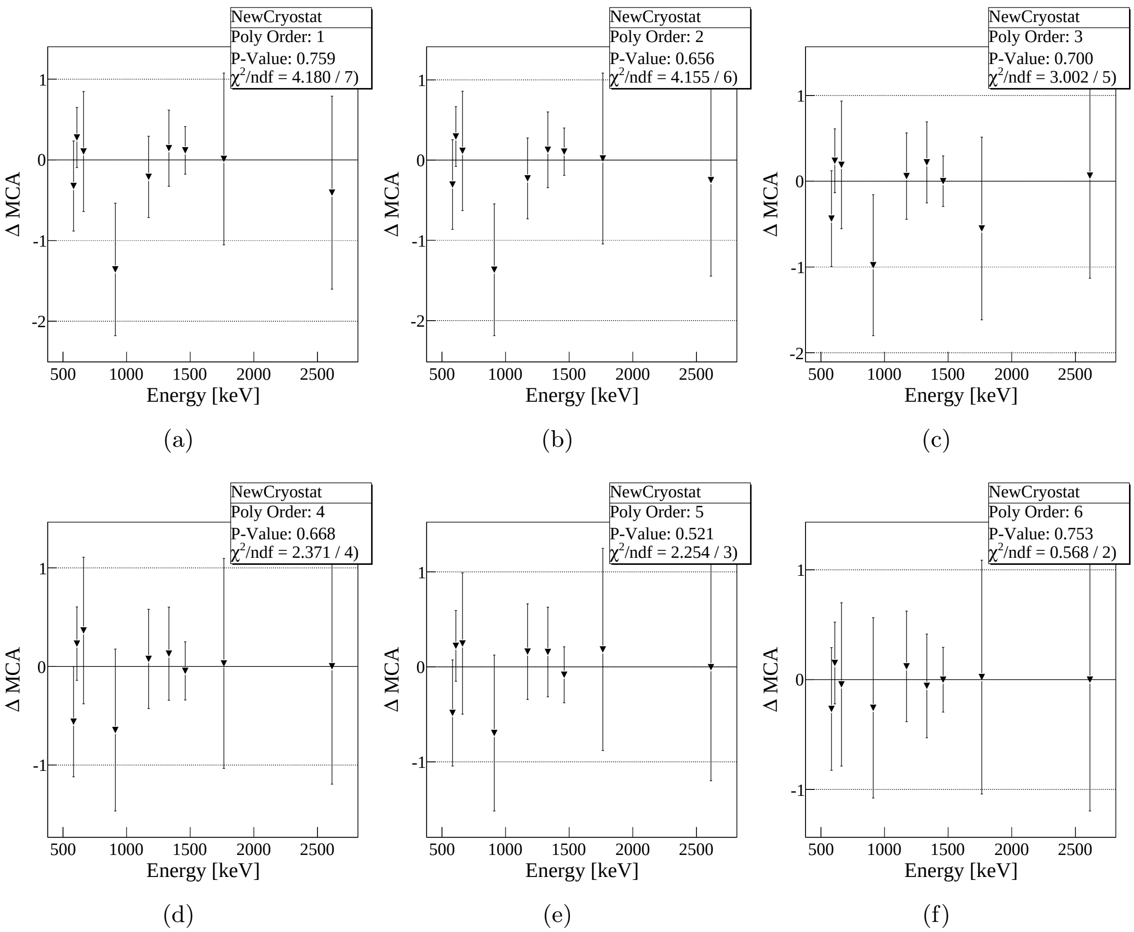

Figure 4.10: Polynomial fits to determine calibration coefficients. The centroids and errors of fitted peaks are plotted against their known energies and fitted with polynomials. The residuals of the fits are shown. In this case, there is no reason to choose a polynomial fit higher than order 1 (linear).

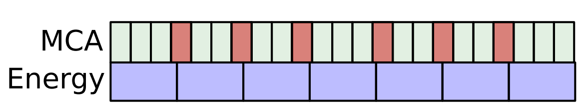

Figure 4.11: Converting MCA bins to energy bins. MCA bins (green and red) do not map neatly onto energy bins (blue). MCA bins that do not map to a single energy bin are marked in red.

The final conversion of MCA histogram to energy histogram depends on the desired binning; MCA spectra for WIPPn and SANTA were converted to energy spectra with 1-keV wide bins. A problem arises from the conversion of discrete MCA values to discrete energy bins. There will not be a one–to–one or even many–to–one correspondence between MCA and energy bins; rather there will be MCA bins that will not map to a single energy bin (see red bins in Fig. 4.11). Performing a straight conversion from one binning to another will result in aliasing, and the number of events in a bin will no longer be distributed according to a Poisson distribution. One method of circumventing this is to convert the MCA values from discrete to continuous. This can be done (and was for data from the DGF) by adding a random number between 0 and 1 (or -0.5 and 0.5) to the original MCA value for each event. This would in principle contribute some excess smearing to the energy spectra. In practice, the number of MCA bins corresponding to 1 keV is 4-5, and peaks have widths of several keV, and so this smearing is negligible.

It is useful to understand the peak width as a function of energy. The information stored in `pickledIgorPeakFit` files includes all fit parameters, including the width (standard deviation, σ) of the peaks. The full-width at half-max (FWHM) is related to σ via (assuming Gaussian peaks)

$$\mathrm{FWHM} = 2\sqrt{2\log 2}\sigma \simeq 2.35\sigma. \tag{4.3}$$

As explained in Section 2.1, the resolution of a detector is dependent upon several parameters. Electronic noise from the preamp and digitizer add a constant term to the noise, σ_e. A second term comes from charge-carrier statistics; it costs $\varepsilon = 2.96$ eV to liberate an electron-hole pair, so the deposit of energy E would ideally correspond to a number of such electron-hole pairs, $N_{e-h} = E/\varepsilon$. The variance in N_{e-h} would be equal to N_{e-h} if the process were truly Poisson-like, and this would give $\sigma^2_{e-h} = \varepsilon E$. The process is not exactly random, however, and in practice a coefficient called the *Fano factor* is added. The variance is then given as $\sigma^2_{e-h} = \varepsilon EF$. The two noise contributions are completely uncorrelated and add in quadrature, leading to a combined

$$\sigma = \sqrt{\sigma_e^2 + \varepsilon FE}. \tag{4.4}$$

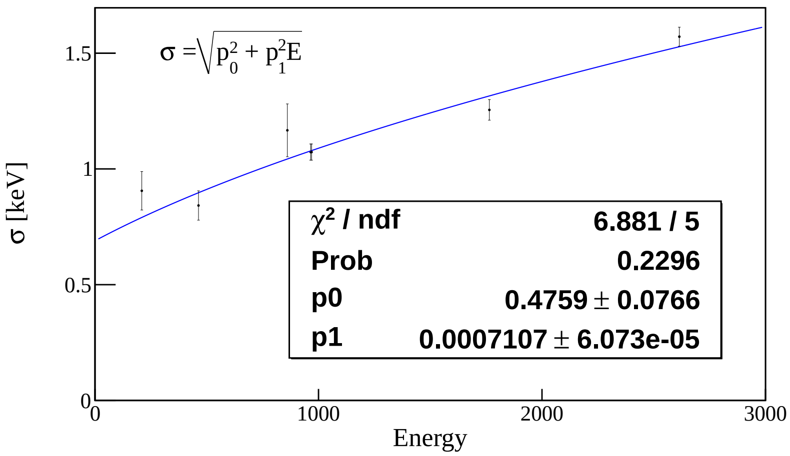

Figure 4.12: Measured peak widths fit with a resolution function.

In practice, the terms σ_e^2 and εF are determined via a fit of equation 4.4 to the measured peak widths as a function of energy. An example of this is in Fig. 4.12, where a multi-source (^{232}Th , ^{238}U) calibration sample was measured with the WIPPn detector. The peak widths and errors are then plotted and fit with Eq. 4.4.

Livetime calculation

The livetime of a run is not equivalent to the time difference between the start and stop of that run. Rate calculations are only valid and useful if the livetime is known. The DGF is not a dead-time free digitizer, and each event contributes a small dead time (trigger dead time) as well as a dead period at the end of each buffer as the buffer is written to disk (buffer dead time). The trigger dead time is imposed as a pile-up rejection mechanism; the DGF sets a time window after each event in which any further energy deposits are recognized as pileup and the event discarded. Figure 4.13 plots the time difference of successive events for a WIPPn source run. The trigger time window of 23 μs is visible in Fig. 4.13(a) as the gap between $\Delta t = 0$ and $\Delta t \simeq 23\mu$s. Figure 4.13(b) shows the time differences for all events in the run. There are 199 events between 0.058 and 0.1 s, corresponding to the extra dead time between spills (there were 200 spills for this run). The dead time for writing a buffer spill to disk, evidenced by the gap below this bunch, is approximately 60 ms.

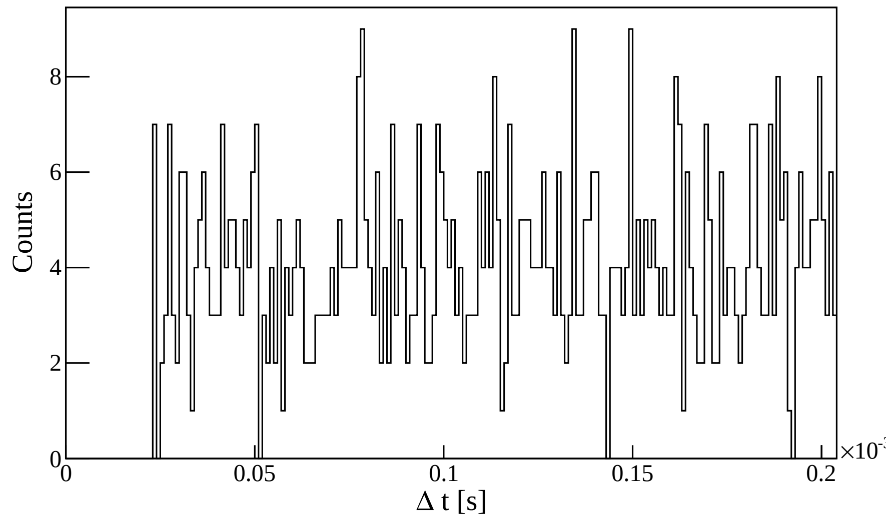

(a) Livetime: trigger dead time

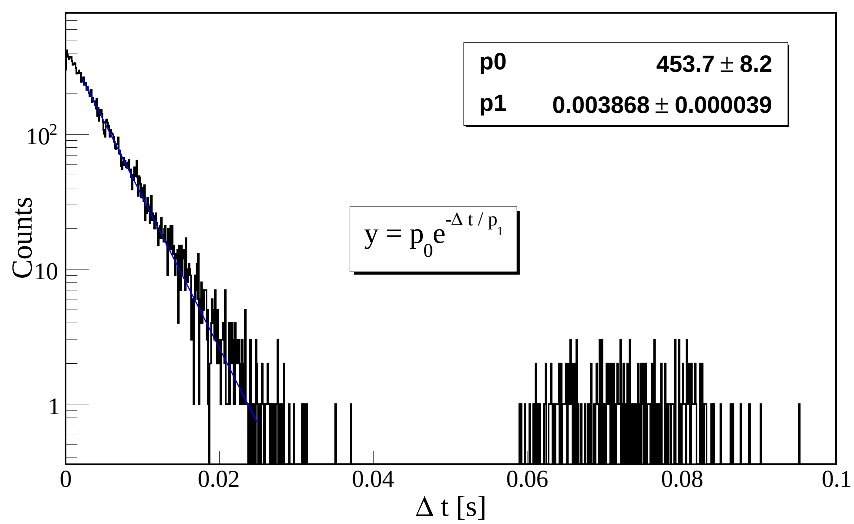

(b) Livetime: buffer dead time

Figure 4.13: Time differences of subsequent events for WIPPn source run. (a) is zoomed in, showing the gap between 0 and 24 μs, corresponding to the dead time from forced by a valid event trigger. The range is expanded in (b), showing the exponential shape (expected from Poisson events). The events above 0.05 s correspond to the time between buffers. This time is not included in the runtime, so it does not need to be explicitly removed for the livetime calculation (see Eq. 4.5 and text).

The DGF attempts to calculate the livetime and deadtime, but close inspection has revealed that the calculated parameters are suspect. As an example, two runs with similar elapsed clock times under identical conditions and with similar numbers of counts will have wildly different livetimes, as calculated by the DGF. XIA has also recently confirmed that prior firmware versions (prior to September, 2009) of the DGF-family of digitizers included an ill-defined definition of livetime [45, 46].

All data in this work were taken prior to September, 2009, and so lifetime estimates calculated by the DGF are considered suspect. Instead of using them, livetimes can be calculated directly from the data using event and buffer time stamp information. For explanatory purposes, some definitions are in order. The walltime is defined as the wall-clock time that elapses between a run being started and stopped. The DGF records these start and stop times in an external meta-data file, and they are also entered manually into the experiment logbook. Each run is typically composed of multiple buffers or "spills," and the end of these spills is marked by the DGF writing the buffer to disk. The buffer time stamp is always the time the buffer starts taking data. This is not the same as the first event in the buffer. The last event in a buffer is immediately followed by the data dump, and so the time length of a buffer may be defined as the time difference between the buffer time stamp and the last event time stamp. The runtime of a run is this time difference, summed over all the buffers in a run. Each event, as explained above, includes a dead period from the trigger. If a buffer contains $N_{e/b}$ events (88 events/buffer is typical of WIPPn data), there are $N_{e/b} - 1$ of these dead periods per buffer. This trigger deadtime (Δt_T) needs to be subtracted from the runtime (Δt_{rt}) for each buffer. The livetime is then defined as the sum of all trigger deadtimes subtracted from the total runtime, or

$$\begin{aligned} \Delta t_{lt} &= \Delta t_{rt} - \sum_{buf=1}^{N_b} \left(N_{E/B}\right) \Delta t_T \\ &= \Delta t_{rt} - \left(N_b + N_e\right) \Delta t_T, \end{aligned} \tag{4.5}$$

The total runtime Δt_{rt} is calculated by looping over all buffers and events in a run's `TTree`, and the total livetime Δt_{lt} is calculated via Eq. 4.5.

Once energy calibrations and livetime calculations have been concluded, these values can be stored in a `TTree`, DGFCalibTree, with each row of the `TTree` corresponding to a row in the DGFTree. The new information can then be easily collated with the existing DGFTree via the `TTree::AddFriend()` method, allowing the DGFTree to access the branches of DGFCalibTree.

4.3 Germanium Analysis Toolkit (GAT)

As the collaboration has settled on a data structure, efforts have recently gone into creating a uniform analysis toolkit. Analysis efforts by individuals and groups have by and large been home-grown, disjoint, and specific. The need for a more generic toolkit that works with plug and play modules is of great importance.

4.3.1 Analysis framework

The first (preliminary) version of the Majorana Collaboration's Germanium Analysis Toolkit (GAT) was in production from Fall 2007 through Spring 2008. The general guidelines for this project were to formulate a generic analysis framework, based upon MGDO data objects, that would allow a user to read in OrcaROOT-style data files, perform processing tasks upon the data, and write out the output files. Specifically, a user could write a class that inherits from a virtual processor class, i.e. GATVProcessor. Such a class would have access to all of the information from an event. An example of such a class would be to read in the waveform, calculate desired moments (RMS, skew, kurtosis) that might be useful for pulse-shape analysis, and then write this output to a `TTree` and histograms.

This toolkit was used in preliminary data analysis for both WIPPn and SANTA data. The collaboration has since that time decided to pursue a separate analysis toolkit structure, so GAT-I has been relegated to the revision control attic.

Many of the problems with GAT-I concern the need for parallel analysis. To first order, an analysis program would consist of a module that opens up a data file, some number of modules that perform various analysis on the data (processors), and modules that write the processed data in a useful format. Things become more complex when the processors

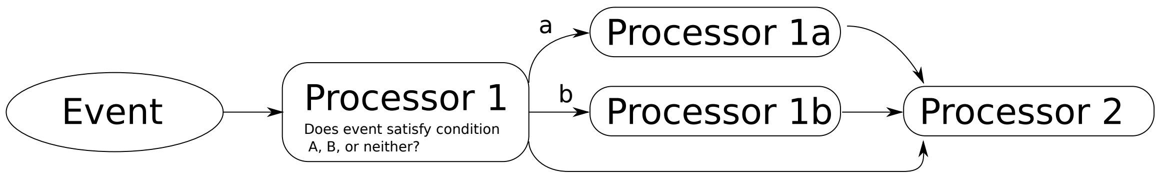

Figure 4.14: Example of a parallel processor chain. Processor 1 checks to see whether an event satisfies condition a, condition b, or neither. If a or b, the event is sent for further processing that depends on those conditions and is then sent on to Processor 2. If a or b are not satisfied, the event is just passed to Processor 2.

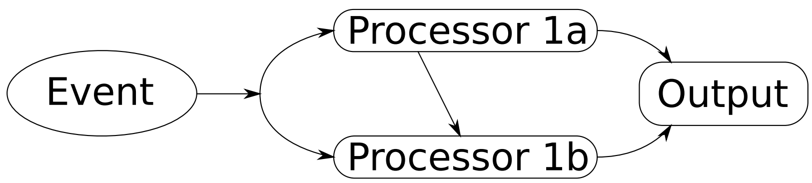

Figure 4.15: Example of a parallel processor chain where Processor 1a calculates a quantity for each event that Processor 1b requires to process the same event.

have to communicate amongst themselves. An example of this can be seen in Fig. 4.14: A processor is fed an event, calculates a value for some parameter, and determines whether that parameter satisfies condition A, B, or neither. Depending on that decision, the event is either sent to Processor 1A, Processor 1B, or is sent ahead to Processor 2. A separate type of analysis chain is shown in Fig. 4.15: Processor 1b requires the results of Processor 1a in order to proceed. The initial version of GAT had no mechanism to generically take into account this sort of behavior.

TAM, or Tree Analysis Modules, is a general, modular framework for analyzing data in ROOT trees[47]. It was written by Maarten Ballingtijn, Constantin Loizides, and Corey Reed at MIT. TAM is generic enough to be suitable as a base for a Germanium Analysis Toolkit. In particular, it natively handles all input/output and allows for an intelligent schema for a processing network. It also allows the passing of objects between processor modules.

The building block of TAM is the TAM processor module. Each module is expected to interact with the framework in the same manner, i.e. through overloaded methods. These

Table 4.2: Class methods that a TAM module can overload to plug into a TAM analysis framework. Descriptions and specific examples from the simple pulse-shape analysis processor are given. While not used in the example, there are three other overloaded class methods: `Begin()`, `Terminate()`, and `Notify()`. These are used for parallel processing large numbers of files via a client–master–slave hierarchy.

Method	Description	Example
`SlaveBegin()`	Allocations at beginning of run	Create `TTree` and `TH1D` objects
`Process()`	Process an event	Read (charge) waveform from event Create current waveform Calculate mean, variance, skew, kurtosis Fill histograms and tree
`SlaveTerminate()`	De-allocations	delete `TTree`, `TH1D` objects

methods are given in Table 4.2.

4.4 TAM Example: A simple pulse-shape analysis module

The discrimination of single-site vs. multi-site events is key in reducing backgrounds for $0\nu\beta\beta$ experiments. The emitted betas in $0\nu\beta\beta$ share 2.039 MeV of energy, losing it within a very short distance of the decay site within the germanium. This single-site event is contrasted with, for example, a gamma that Compton scatters several times at different points within a detector. The pulse shape of an event is affected by where in the detector the deposit occurred, and so events with multiple deposits within a crystal will have what looks like a superposition of events. Figure 4.16 shows two separate events from the WIPPn detector. Both deposited nearly the same amount of energy (4560 keV), but the topology of the two events is quite different. The current pulse in Fig 4.16(a) is indicative of a single-site event: mostly symmetric with a single peak. In contrast, the current pulse in Fig. 4.16(b) has three distinct peaks, separated in time. The human brain is quite adept at picking out differences and patterns in objects, but it is also subjective and state-dependent, and not necessarily reproducible. Pulse-shape analysis instead depends on a quantitative deconstruction of a pulse, attempting to separate pulses into different categories by comparing calculated parameters. Much work has gone into developing sophisticated pulse-shape

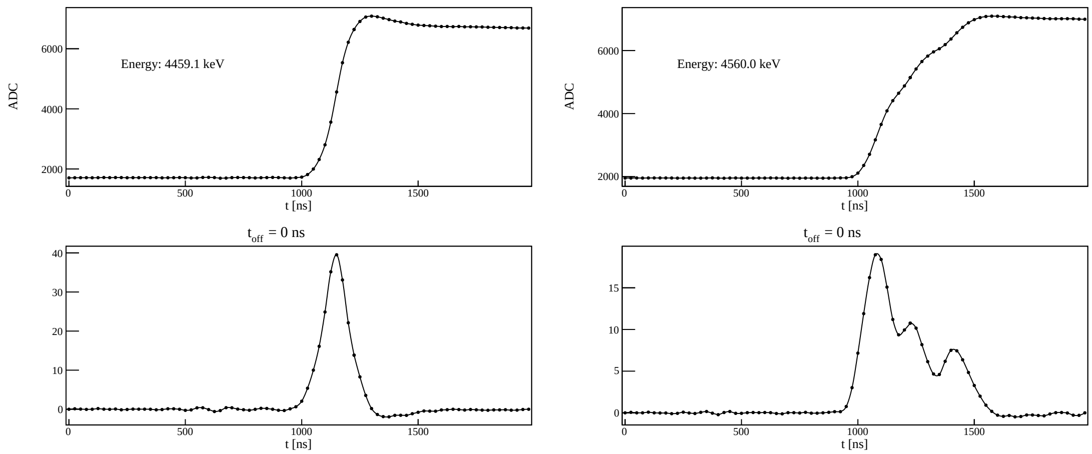

(a) Single-site pulse shape

(b) Multi-site pulse shape

Figure 4.16: Charge and current pulse shapes from the WIPPn detector. While both events deposited nearly the same amount of energy within the detector, the pulse-shapes are quite different: pulse (a) shows characteristics of a single-site event, while pulse (b) is multi-site.

analysis techniques in the Majorana Collaboration (see e.g. [48, 49]). Here is presented a simple model of pulse-shape analysis that will be applied to the WIPPn data to address the feasibility of PSA against alpha backgrounds.

The digitized waveform signal corresponds to integrated charge, as discussed in Section 2.1. The current pulse, calculated as the time derivative of the charge pulse, resembles a peak and looks vaguely Gaussian for simple, single-site events (as in Fig. 4.16(a)). One method of extracting information from a peak is by calculating its moments. For discrete distributions such as digitized current pulses, the n^{th} moment is

$$\langle t^n \rangle = \frac{\sum_{k=1}^{N} t_k^n}{N}, \tag{4.6}$$

where N is the total number of points in the distribution and t_k is the k^{th} point. The most familiar example is the expectation value for a parameter t, $\langle t \rangle = \mu = \frac{1}{N}\sum t$, and describes the sample mean of the distribution. When one is only interested in the properties of a pulse, and not the offset, one can calculate the *moments around the mean.* The second such moment, $\sigma^2 = \frac{1}{N}\sum(t-\mu)^2$, is the variance, giving a sense of the width of the distribution. The square-root of the variance, σ, is the standard deviation. For a Gaussian distribution, the value of σ tells how far one must integrate out from the mean ($[\mu-\sigma, \mu+\sigma]$) to encompass 68.6% of the area. One can calculate $\langle \mu - t^n \rangle$ for any n, but only the first few have obvious significance to the shape of a pulse and so we use the first four. Whereas μ and σ have units of $[t]$, it makes sense to "normalize[4]" further moments and divide the nth central moment by σ^k, thus making them unitless. The skewness, $\gamma = \frac{1}{N}\frac{\langle(\mu-t)^3\rangle}{\sigma^3}$, gives a sense of a peak's asymmetry. The final moment to consider is the kurtosis, $\kappa = \frac{1}{N}\frac{\langle(\mu-t)^3\rangle}{\sigma^4} - 3$. The kurtosis is a measure of whether a distribution is skinny or squat, relative to a Gaussian. The number 3 is subtracted from the usual normalized central moment so that the kurtosis of a Gaussian is equal to zero.

A TAM module, named `PSA4Dummies`, was constructed along the TAM guidelines to serve as a simple example of performing pulse-shape analysis of germanium data. The TAM framework is given the file(s) containing the `TTree` with data. The events are fed to the PSA4Dummies processor, where the waveform is read out and transformed into a current pulse via the `MGDO` waveform transform `MGWFTransformDerivative()` class. The moments (mean, variance, skew, and kurtosis) of the pulse shape are calculated, histogrammed, and stored in a `TTree`. Table 4.2 provides a short explanation of what happens at each stage of processing. The feasibility of using pulse-shape analysis for discriminating alpha events is discussed in Sections **??**.

[4]Not normalized in the usual sense of setting equal to one. The word is still valid, as the definitions are set such that the next two moments are equal to zero for the normal distribution

Chapter 5

VALIDATION OF ALPHA SIMULATIONS: THE SANTA DETECTOR

The need for a test stand with an active, controllable alpha source resulted in the Surface Alpha N-type Testing Apparatus, a.k.a. the SANTA detector. This test stand was designed, constructed, and run with the goal of characterizing the response of an N-type HPGe detector to alpha decays impinging on the p^+ surface, and also to validate alpha simulations in MaGe. The test stand was run in two separate modes, measuring both surface-type and external-bulk type alphas.

5.1 A Modified N-Type HPGe Detector

Rather than design and build an entirely-new test stand, it was decided to purchase and modify an existing commercial detector. In particular, the mounting of the HPGe crystal and the signal extraction electronics would be left in place. This commercial detector was an N-type HPGe detector from ORTEC of the "PopTop" variety [50]. Table 5.1 details the detector dimensions and characteristics as determined by the quality-assurance data sheet provided by ORTEC with the detector. Figure 5.1(a) is a photograph of the full detector assembly, with the dipstick inserted into a liquid nitrogen dewar. Figs. 5.1(b) and 5.1(c) show a photograph and schematic of the innards of the detector.

5.1.1 Initial Runs

The PopTop detector was first partially disassembled within a glovebox at Los Alamos National Laboratory in January, 2008, The primary goals of this inspection were to determine the ease of disassembly / assembly and to make measurements for a future modification. It was learned that the outer can is quite difficult to remove from the capsule, due to the piston-style O-ring seal at the base of the capsule and the lack of grip by which to pull the can off the base (this O-ring seal is visible in Fig. 5.1(b) and 5.1(c)). With this in mind,

Table 5.1: Detector characteristics of the original ORTEC PopTop detector, as referenced from the product's data sheet. The original outer can (cryostat) was fitted with a beryllium window on the face. All specifications and dimensions were measured by ORTEC for this specific detector except for the inactive germanium (outer dead layer thickness). This 0.3 μm value appears on all such quality assurance data sheets. The performance specifications were measured at a nominal rate of 1000 counts/s, with an amplifier time constant of 6 μs. The peak-shape parameters FWTM and FWFM stand for full-width, third-max and full-width, fourth-max.

Cryostat and Preamp Properties			
Detector Model No.	*GMX50P4-ST*	Preamp Model	*A257N*
Configuration	*PopTop*	Preamp Serial No.	*7171142*
Serial No.	*47-TN22205B*	H.V. Filter Model	*138EMI*
Ship Date	*7-31-07*	H.V. Serial No.	*7207158*
Dimensions			
Crystal Diameter	*64.0 mm*	Crystal Length	*72.3 mm*
End Cap to Detector	*4 mm*	Be Window Thickness	*0.50 mm*
Inactive Germanium	*0.3 μm*	Detector Geoemtry	*Semi-coax*
Performance Specifications			
Attribute		**Warranted**	**Measured**
FWHM at 1.33 MeV, ^{60}Co		*2.2 keV*	*2.11 keV*
Peak-to-Compton Ratio, ^{60}Co		—	*55:1*
Relative Efficiency at 1.33 MeV, ^{60}Co		*50%*	*54.5%*
Peak Shape (FWTM/FWHM), ^{60}Co		—	*2.27*
Peak Shape (FWFM/FWHM), ^{60}Co		—	*4.29*
FWHM at 5.9 keV, ^{55}Fe		*800 eV*	*713 eV*
Recommended operating bias		*-4800 V*	

the internal measurements that were taken were used to design an outer can replacement.

5.1.2 Outer Can Replacement

Ideally, the test stand would not need to be opened very often, as each breaking of vacuum is a chance for H_2O or other contaminants to plate out on the crystal and for the detector to lose performance. However, the reality of a test stand likely requires multiple tinkerings, and so the first criterion for a new outer can was ease of opening. The second requirement was the ability to maneuver an alpha source close to the crystal by external control (i.e.

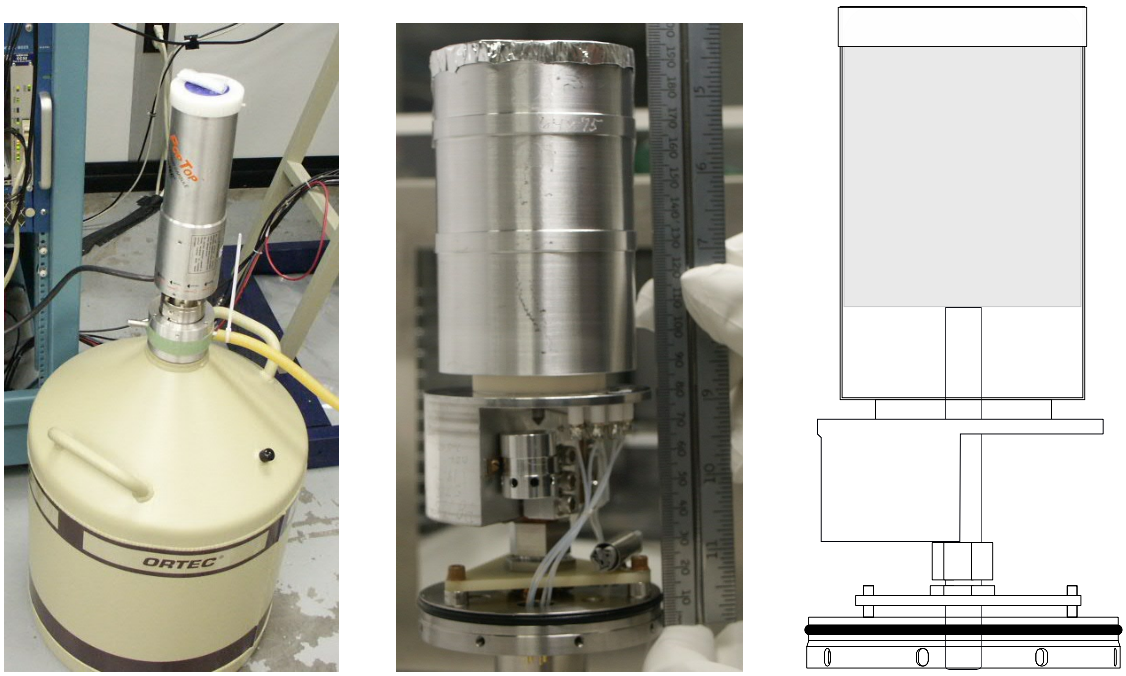

(a) (b) (c)

Figure 5.1: The PopTop detector, unmodified and inside of its dewar (a), with the "outer can" removed and showing the innards (b), and a schematic of the innards showing the HPGe crystal (shaded gray) nestled inside of the mounting cup (c). The O-ring makes a piston-type seal and can be seen at the bottom of the opened capsule in (b) and (c).

being able to manipulate an internal alpha source from outside the vacuum can). The can was also designed to be modular, both for ease of working within a constrained glovebox and to anticipate future design changes.

Figure 5.2 shows the new outer can as designed and built. The can separates into three pieces. The bottom piece was designed to mount to the difficult O-ring seal on the capsule, and as such should only have to be installed once. This piece is short in height so that a break in the vacuum can be made near the bottom of the can, but with an easier seal. The faces of the outer-can pieces were machine-polished flat, and the seal was made using lead-wire seals. Twelve 10-24 threaded bolts around the circumference of the can connect the two faces which sandwich the lead seal in between (Fig. 5.2(a). Using metal seals allows for an easier time when breaking vacuum and accessing the detector. The middle portion of the can is a cylinder 13" tall with an outer diameter of 4.5" and an inner diameter of 4.2". Two separate tops were created for the outer can. One is a simple blank-off piece (Fig. 5.2(a), while the other includes a rotational feedthrough (shown in Fig. 5.2(b)). This "top-hat" design allows external manipulation of an alpha source.

5.1.3 Rotational feedthrough, source arm, and discrete collimation plate

Collimation of the alpha source was accomplished by use of a metal cap sitting atop the detector mounting cup (Fig. 5.3). This cap, made from aluminum, was drilled through with a succession of collimation holes (Figure 5.4). The holes were set such that an ideally placed source, centered at a radius of 0.6" from the center of the crystal and at a height of 0.1" above the collimation plate, would have a direct shine path down the middle of the hole. Figure 5.4(a) shows a top-down view of the plate, and Fig. 5.4(b) is a side view showing the source placement and a representative alpha-shine path through a collimation hole.

5.1.4 Slit collimation plate

A separate configuration for the SANTA detector involved replacing the top-hat with a simple blank-off, and replacing the discrete-collimation cap with a continuous-collimation cap. This cap has identical dimensions to the first cap, but contains a long slit from the center to the edge instead of individual collimation holes (Fig. 5.5).

5.2 Surface-Alpha Backgrounds

5.2.1 Discrete hole data and the ^{241}Am source

A windowless alpha source from Isotope Products [51] was procured for use with SANTA. The activity of this ^{241}Am source was 161.9 Bq (as measured by Isotope Products on 1 September, 2007. The decay of $^{241}\text{Am}\rightarrow^{241}\text{Np}$ (Q-value: 5637.82 keV) results in the emission of an alpha particle 100% of the time. The five main alpha branches are noted in Table 5.2. There is also a gamma emission with non-negligible branching ratio that occurs with the 5485.56 keV alpha. Some fraction of decays will deposit both an alpha and a gamma in coincidence, and so the energy spectrum as measured by the HPGe detector will reflect

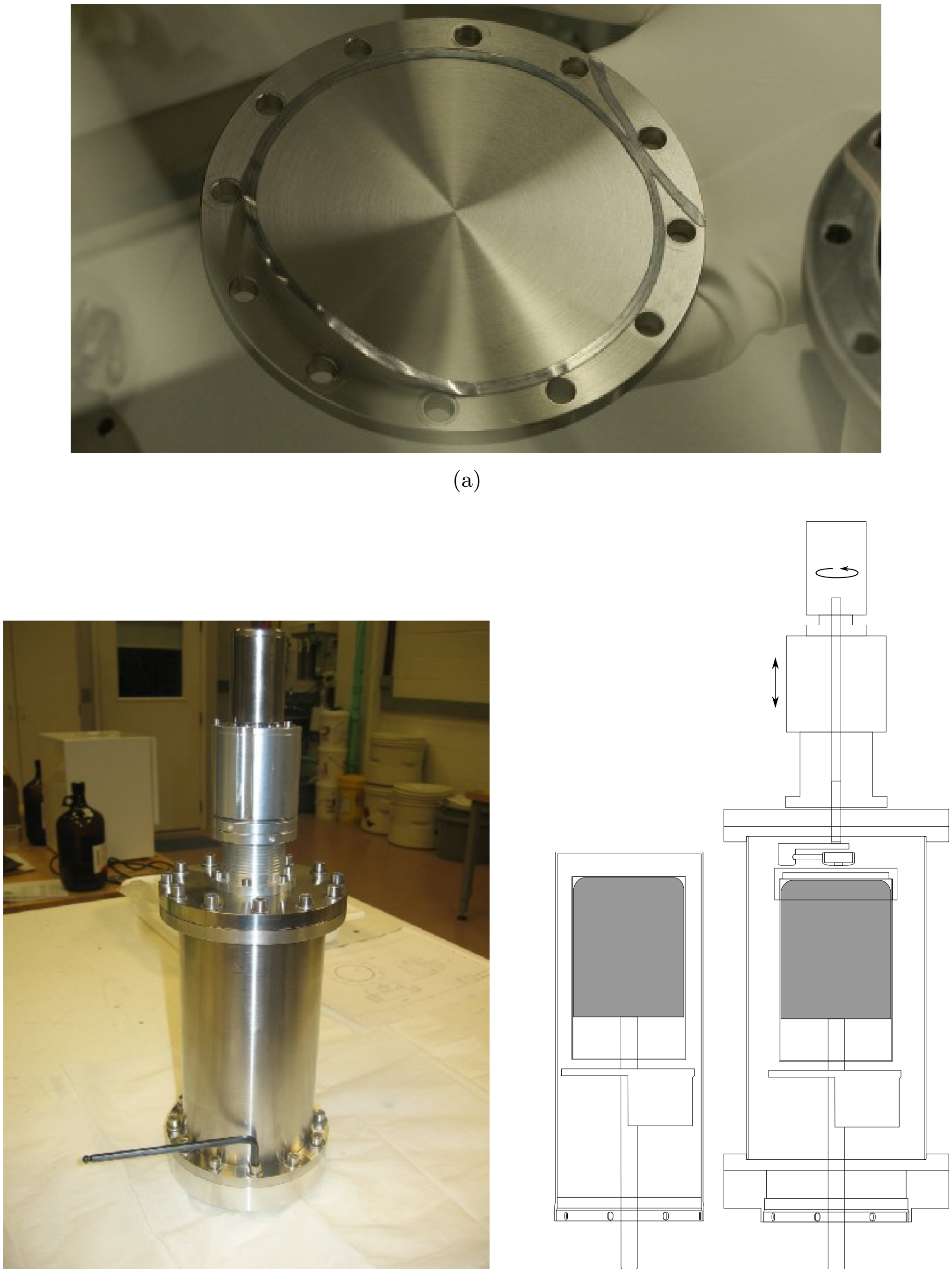

(a)

(b) (c) (d)

Figure 5.2: The outer can for the SANTA detector. (a) shows the blank-off top and a used lead-wire seal. (b) is a photograph of the new can. (c) shows a schematic of the initial (PopTop) can compared with the new can (d). The top of the can includes a rotational feedthrough in this configuration. The rotational manipulator is noted in (d), as well as the barrel height adjuster.

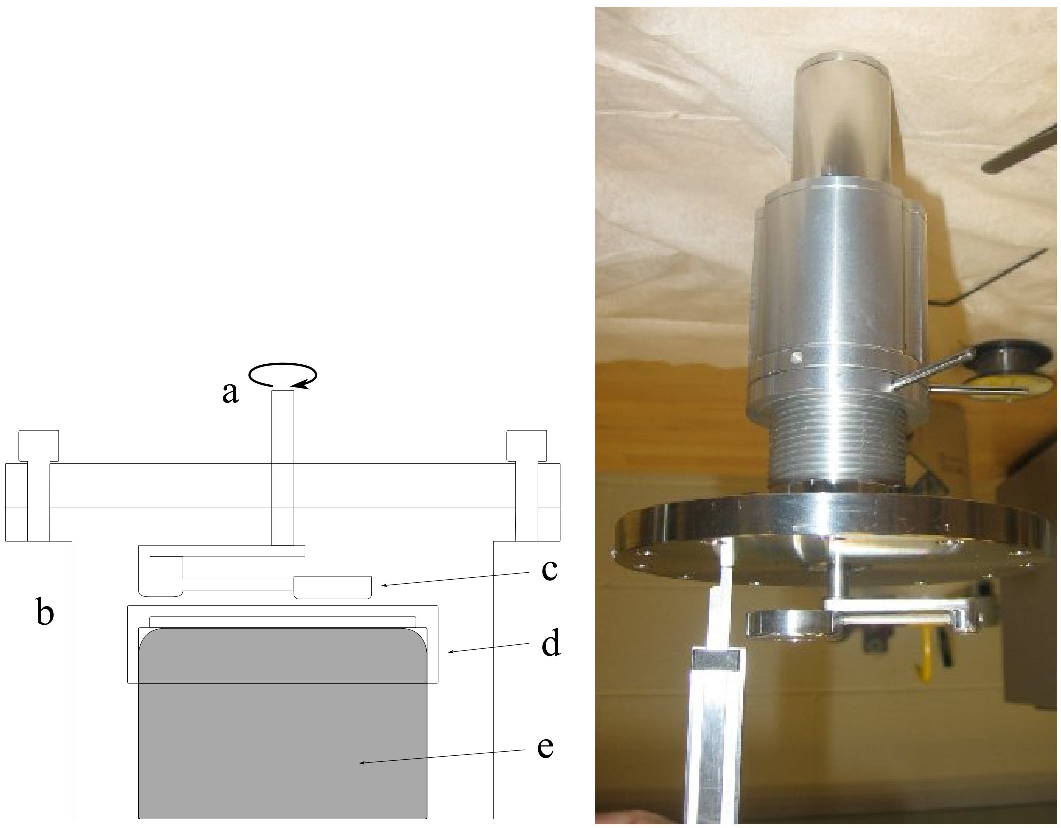

(a) (b)

Figure 5.3: Side-view of SANTA source and collimation setup. (a) shows an inside view of the outer can, with **a:** rotational feedthrough, **b**: new outer can, **c**: alpha-source, **d**: collimation cap, and **e**: the HPGe crystal inside of its mounting cup. (b) is a photograph of the “top hat” without the rest of the outer can. The feedthrough manipulator and source-arm and source are shown (the photograph is inverted). The source arm can be raised or lowered via the barrel adjustor in the picture.

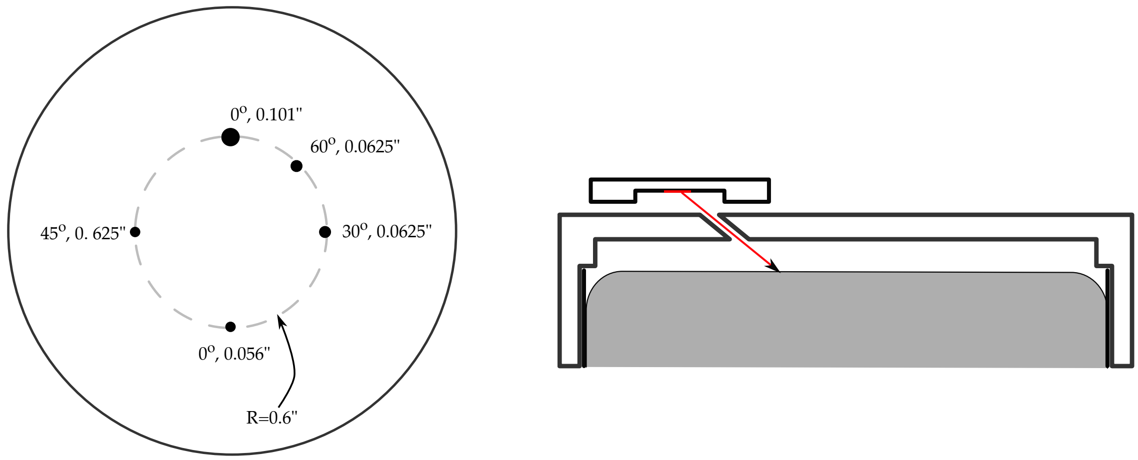

(a) (b)

Figure 5.4: SANTA collimator plate, top-down (a) and side-view (b). The dashed circle in (a) represents the track the alpha source traverses above the collimation holes. The geometry is such that the alpha source can only shine through at most one collimation hole at a time. The holes are marked with hole-angle (with respect to normal) and hole diameter (in inches). (b) shows a representative cross-section for one of the collimation holes with the alpha source aligned above it.

(a) (b)

Figure 5.5: Bottom-views of the continuous-collimation (slit) cap. A surface- or bulk-alpha source can be affixed to the top, allowing alpha shine with a continuous spectrum of angles. (a) is a photograph, and (b) is the cap as simulated.

Table 5.2: The five prominent alpha lines and the prominent gamma line from the decay of $^{241}\mathrm{Am} \rightarrow {}^{237}\mathrm{Np}$. They are numbered for reference in the text. The gamma line occurs only in coincidence with the α A-III. Values of energy and branching ratio are taken from [41]

	Energy	Branching Ratio
	α	
A-I	5388 keV	1.66%
A-II	5442.8 keV	13.1%
A-III	5485.56 keV	84.8%
A-IV	5511.5 keV	0.225%
A-V	5544.5 keV	0.37%
	γ	
G	59.541 keV	37.9%

this with some of the events from A-III going into a higher energy peak. The deposited energies of alpha A-III with a gamma coincide with the energy of alpha A-V.

The test stand was run with the ^{241}Am source attached to the rotational feedthrough arm (Fig. 5.3). Manipulation of the feedthrough allowed placement of the source above the holes in the collimation plate (Figures 5.4 and 5.3). In these figures, and elsewhere in this dissertation, the angle is defined with respect to the normal of the crystal surface, i.e. $0°$ would be straight down. It was found that the size requirement of the holes was larger than desired, due to the high cosmic-event rate at LANL. This added a slight wrinkle in the analysis that is explained in the next section. The collimation holes were drilled at the angles and diameters shown in Fig. 5.4(a).

5.2.2 Response Model for Surface Alpha Energy Spectra

For fitting purposes, it is useful to come up with a physically-motivated model to describe the energy spectra of surface-alpha events.

Peak shape and position

A mono-energetic beam of alpha particles incident on a "perfect" detector, one with no dead region and with perfect charge collection, would result in narrow Gaussian peak at the energy of the alpha. The width of the Gaussian would be determined by the Fano statistics of the number of charge carriers (electron-hole pairs) liberated by the alpha. Such a "perfect" detector does not exist, at least not as a germanium diode. Losses of charge carriers, both within the bulk of the detector and at the surface dead region, serve to modify the energy spectrum by pushing it lower in energy resulting in a low-energy tail. The stochastic nature of energy loss within the dead region also leads some alphas to lose more energy than others (see e.g. [32]). This energy straggling adds a separate and independent source of variance to the deposited energy spectrum, and so serves to broaden the peak more than charge-carrier statistics alone. An exponentially-modified Gaussian (EMG), i.e. a Gaussian curve convolved with an exponential, can qualitatively describe the energy peak of a mono-energetic beam of alphas at a single angle. The normalized form of the function is derived in Appendix A.2, and is

$$\mathcal{S}(E,\mu,\sigma,\tau) = \left(\frac{1}{2\tau}\right) \exp\left(\frac{E-\mu}{\tau}\right) \exp\left(\frac{\sigma^2}{2\tau^2}\right) \operatorname{Erfc}\left(\frac{E-\mu}{\sqrt{2}\sigma} + \frac{\sigma}{\sqrt{2}\tau}\right). \tag{5.1}$$

The variables μ and σ correspond to the mean and standard deviation of the unconvolved Gaussian. The variable τ corresponds to the exponential parameter as in $\exp\left(\frac{E-\mu}{\tau}\right)$. Qualitatively, τ is a measure of the asymmetry of the Gaussian, but it should not be confused with the skewness (i.e. the third normalized moment about the mean). The actual skewness of the EMG is derived in Appendix A.2 and is listed in Table A.1. Figure 5.6 compares a Gaussian ($\tau = 0$) with several EMGs that differ in the asymmetry parameter τ.

The additional variance of energy deposition can be calculated using a Bohr treatment of energy loss in matter [52, 53]. The treatment of ionized particles traveling through matter is a well-studied problem, particularly at the energies of alpha decays [1]. Unlike gamma interactions, charged ions undergo a continuous slow-down due to multiple-scattering interactions between the ion and the electron lattice. The question of energy loss in the dead layer maps directly to the question of energy loss of ions in a thin film. In particular, the energy loss an alpha undergoes while traveling through a particular thickness of material is governed by a distribution of either the Landau, Vavilov, or Bohr varieties. It will be beneficial to parameterize the problem in terms of variables describing the energy and charge

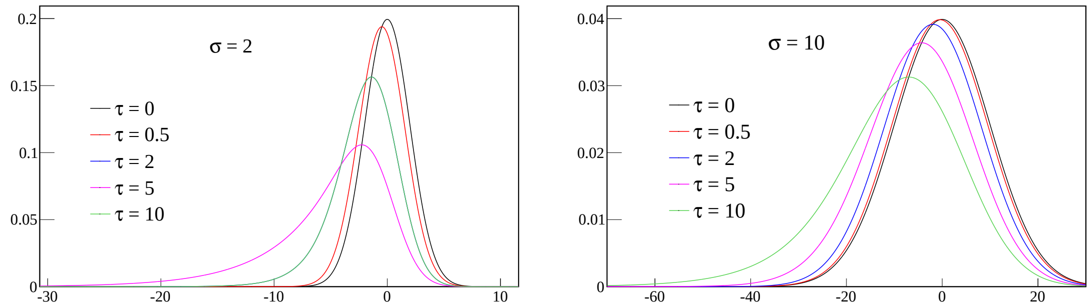

(a) $\sigma = 2$ (b) $\sigma = 10$

Figure 5.6: Comparison of Gaussian with exponentially-modified Gaussians. The $\tau = 0$ curves correspond to simple Gaussians.

of the ion and the properties of the absorber material.

First, let γ and β be the usual relativistic parameters describing the energy of the alpha, s.t. $E_\alpha = \gamma M_\alpha$ and $\beta = \sqrt{1 - \frac{1}{\gamma^2}} \sim v/c$ where the approximation is good for non-relativistic particles. Next we define

$$\epsilon_{max} = \frac{2m_e c^2 \beta^2 \gamma^2}{1 + 2\gamma m_e / M_\alpha} \simeq 4 m_e c^2 \frac{T}{M_\alpha} = 5.48 \times 10^{-4} T \tag{5.2}$$

as the maximum-possible transfer of energy in a single collision. T is the kinetic energy of the alpha, m_e is the mass of the electron (511 keV/c^2) and M_α that of an alpha (3727.4 MeV). The approximation used is accurate to 0.16% for an 8.8 MeV alpha. Then we define the variable ξ such that

$$\xi = \frac{4\pi N_A r_e^2 m_e c^2 z^2 Z x}{2A\beta^2} = 153.6 \frac{z^2 Z}{A\beta^2} \tau \text{ (keV)}, \tag{5.3}$$

where N_A is Avogadro's number, r_e the classical electron radius, $z = 2$ is the charge of the alpha, $Z = 32$ is the charge of the germanium absorber, $A = 72$ the atomic weight of a germanium isotope, and τ is the thickness of the absorber in units of g/cm^2. We are interested in a specific thickness of the absorber as a parameter, so we express it in terms of distance travelled (Δx) and density ($\rho_m = 5.3$ g/cm^3 for germanium and $\rho_m = 11.7$ g/cm^3 for thorium):

$$\tau = 10^{-4} \cdot \Delta x \rho_m. \tag{5.4}$$

The factor of 10^{-4} allows for Δx to be expressed in μm. Grouping terms, the expression for ξ then becomes

$$\xi = 1.145 \times 10^5 \left(\frac{Z}{A} \rho_m \right) \frac{1}{T} \Delta x (\mathrm{keV}), \tag{5.5}$$

where T is expressed in keV. The expression in parenthesis contains the parameters relevant to the absorber material, and is equal to 2.32 g/cm^3 for germanium and 4.54 g/cm^3 for thorium. The energy-loss regime is best characterized by the parameter κ, defined as $\kappa = \xi/\epsilon_{\mathrm{max}}$. For $\kappa < 1$, a Landau treatment is used. For $\kappa \in [1, 12]$, a Vavilov treatment can be used. For $\kappa > 12$, the straggling distribution approaches a Gaussian and the Bohr treatment is used. The dead layer of the crystal is given as 0.3 μm in the data sheet, which leads to a $\kappa \simeq 15$, and so a simple Bohr treatment should suffice. In such a treatment ([52]), the energy straggling caused by loss of energy within the dead region is modeled by

$$\begin{aligned} \sigma^2 &= \frac{\xi^2}{\kappa} \left(1 - \frac{\beta^2}{2} \right) \simeq \frac{\xi^2}{\kappa} = \xi \epsilon_{\mathrm{max}} = 62.75 \left(\frac{Z}{A} \rho_m \right) \Delta x \\ &= 145.6 \Delta x \qquad \text{(for germanium)} \\ &= 284.9 \Delta x \qquad \text{(for thorium)} \end{aligned} \tag{5.6}$$

with Δx in units of μm. The values for Z, A, and ρ_m are plugged in for germanium (as is the case with the dead region of a crystal) and for thorium (which will be used later in the chapter for the bulk-studies).

The position of the alpha peak, like the width, is affected by the absorption of kinetic energy in the detector's dead region. Specifically, the energy lost to the dead layer is

$$\Delta E = \int_0^{\mathcal{D}/\cos\theta} \frac{dE}{dx} (E) \, dx, \tag{5.7}$$

where θ is the angle of incidence, $\mathcal{D}$ is the depth of the dead region, and where dE/dx is a function of the energy of the alpha. The dead layer is treated as a step function with zero charge collection from the surface to a depth $\mathcal{D}$, and perfect charge collection beyond.

Putting the shape and position information together, the (normalized) pdf of a peak from a mono-energetic beam of alpha particles at incidence angle θ_c is then

$$\mathcal{G}(E, \mu_0, \sigma) = \frac{1}{2\tau} \exp\left(\frac{\sigma^2}{2\tau^2} + \frac{E - \mu_0}{\tau}\right) \mathrm{Erfc}\left(\frac{E - \mu_0}{\sqrt{2}\sigma} + \frac{\sigma}{\sqrt{2}\tau}\right), \tag{5.8}$$

where $\mu_0 = E_0 - \Delta E$, E_0 is the initial kinetic energy of the alpha, τ is the exponential parameter and quantifies the asymmetry of the peak, and σ and ΔE are functions of θ_c and are defined as above.

Tailoring Eq. 5.8 to the ^{241}Am source in the test stand requires summing 5 such peaks (Table 5.2) and also taking into account the background from cosmic ray-induced events. The cosmic background is well-described by a linear polynomial ($\mathcal{P}_1$) in the region around the peak structure (5100-5600 keV), and so the summed analytic model describing surface alphas from ^{241}Am at incidence angle θ in the test stand is

$$R(E, \theta, \mathcal{D}) = N_{\mathrm{Am}} \sum_{k=1}^{5} c_k \mathcal{G}(E, \mu_k, \sigma) + N_{\mathrm{Bg}} \mathcal{P}_1(E), \tag{5.9}$$

with $\mu_k = E_k - \Delta E$ corresponding to the centroid of the k^{th} alpha with original kinetic energy E_k. The coefficients c_k correspond to the relative areas of the 5 peaks and are normalized such that $\sum c_k = 1$. The first two of these coefficients (c_0 and c_1, corresponding to alphas A-I and A-II) are fixed, but the rest are allowed to float to account for the pileup of the gamma with the 5485 keV alpha. N_{Am} and N_{P1} are the number of signal (^{241}Am) and background counts, respectively.

Required modifications to the model

Equation 5.9 represents an idealized model of the ^{241}Am source with cosmic background. Several modifications to this model were required to deal with non-ideal realities of the test stand.

The model assumes that the angle of alphas impinging on the surface is a delta function with no spread. The collimation holes in the crystal cap, as described in Section 5.1.3, were wider than ideal due to the high cosmic-ray background at Los Alamos National Lab and the low activity of the source. This resulted in alphas through a given collimation hole having a wider than desired range of incidence angles (Fig. 5.7). This was accommodated by converting the response model to a sum of functions, each describing a single angle θ_j:

$$\tilde{R}(E, \theta_0, \mathcal{D}) = \sum_j w_j R(E, \theta_j, \mathcal{D}). \tag{5.10}$$

θ_0 is the nominal incidence angle, and the w_j coefficients are weights for a given θ_j that are required to reproduce the range of incidence angles through the collimator. These w_j coefficients depend on the source position with respect to the collimation hole, as well as the collimation hole angle and size. Ideally, an integral convolution would be used instead of a sum as in Eq. 5.10, but the extended nature of the source meant that an analytic form for the angle ranges as a function of source position remained elusive. The weights were calculated using the collimator dimensions and position of the source for a range of angles θ_j. These angles were chosen such that the path lengths that an alpha travels through the dead layer, $\Delta x_i = \mathcal{D}/\cos\theta$, result in constant offsets in energy between successive angles. In other words, $\Delta E(\Delta x_i) - \Delta E(\Delta x_{i+1})$ is a constant $\forall i$. This constant difference in deposited energy was chosen to be 2 keV, which is significantly smaller than the width of the alpha peaks given by energy straggling ($\sim$ 10 keV).

While Eq. 5.7 describes the energy loss of an alpha particle in the dead region, it does not represent the final offset in energy of the observed peak from the initial alpha's kinetic energy. There are two additional offsets that are not accounted for in Eq 5.7, and these represent a correction to the observed energy of an event and must be added to the model. This correction is parametrized as a floating parameter in the surface-alpha model.

As the alpha slows down and its kinetic energy approaches zero, the effects of nuclear recoil on the alpha become more pronounced compared to electron recoil. This results in some of the kinetic energy not being converted into electron-hole pairs and therefore not registering as deposited energy. This effect was calculated using Stopping and Range of Ions in Matter / Transport of Ions in Matter (SRIM/TRIM) software [54], and was found

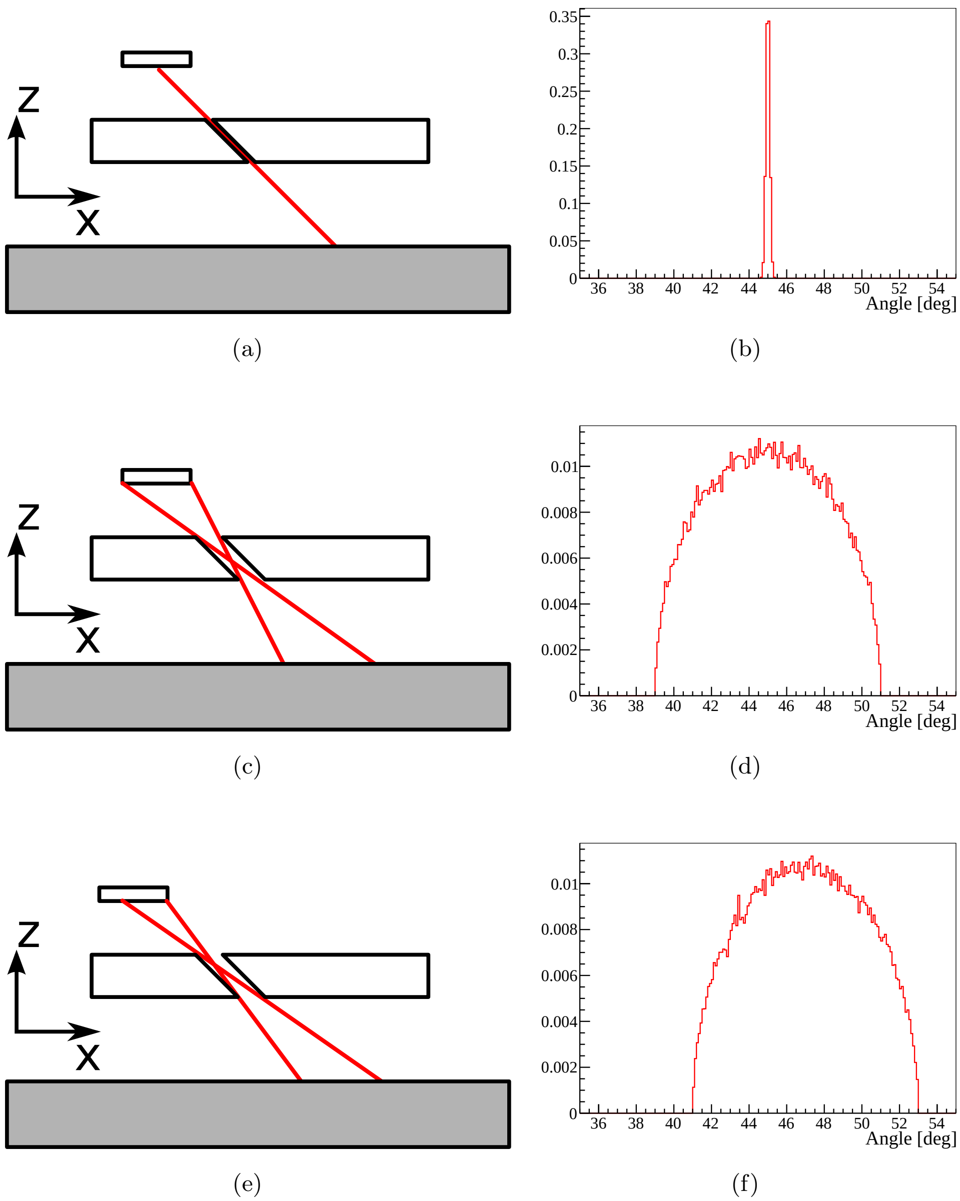

Figure 5.7: Ideally, the collimation holes would limit the alpha shine to a small range around the nominal incidence angle (a and b). The larger hole size causes the angular spread to be larger (c and d). If the source is offset, it affects the range of angles. For example, the source offset shown in (e) results in the spectrum of angles being shifted higher (f). The y-offset is perpendicular to x and z, and is symmetric about $\Delta y = 0$.

to be $\sim$ 10 keV. Because this "missing" energy is lost at the end of the alpha track, it is independent of both the initial kinetic energy and of energy loss within the dead region.

A second offset in the energy spectrum occurs due to energy calibration. As explained in Section 4.2.3, the energies used for calibration (0-2615 keV) are less than half of the energies of interest in alpha spectroscopy (in this case, 5 - 5.5 MeV). Any non-linearity in the detector, while unnoticeable below 2600 keV, could become non-negligible around 5 MeV (see e.g. Fig. 4.7). This offset should in principle be the same for all data from a given detector and is taken care of by the floating energy offset in the model. This is also a source of systematic uncertainty in efficiency calculations, and this will be addressed in Chapter 7.

Surface-Alpha Data and Model Fits

Data were taken with the SANTA detector in its surface-alpha configuration, using the discrete collimators at 0°, 30°, 45°, and 60°. The analytic model (Eq. 5.9 and 5.10) was fit to the data with the goal of extracting the dead layer. The fits were performed by minimizing a binned, extended-maximum likelihood function over the histogrammed surface-alpha data:

$$-\log L(\boldsymbol{\theta}) = N_{Am} + N_{Bg} - N + \sum_i n_i \log\left(\frac{n_i}{y_i}\right) \tag{5.11}$$

where N_{Am} is the number of signal counts, N_{Bg} is the number of backgrond counts, N is the total number of counts, n_i is the number of counts in the i^{th} bin, and

$$y_i = \int_{x_i}^{x_{i+1}} f(x, \boldsymbol{\theta}) dx \tag{5.12}$$

is the expected number of counts in the i^{th} bin. Minimization of $-\log L(\boldsymbol{\theta})$ was performed with `MINUIT`'s `MIGRAD` package [55]. `MINOS` was also used to estimate the parameter errors as a secondary check after `MIGRAD`. After a minimum is found, `MINOS` tracks the likelihood function away from that minimum and finds the values in $\boldsymbol{\theta}$ where $\Delta - \log L(\boldsymbol{\theta}) = -\log L_{min} \pm 1/2$. `MINOS` is more powerful than the usual `HESSE` routine which uses the covariance matrix to estimate the parameter intervals. Specifically, `MINOS` can handle non-parabolic likelihood

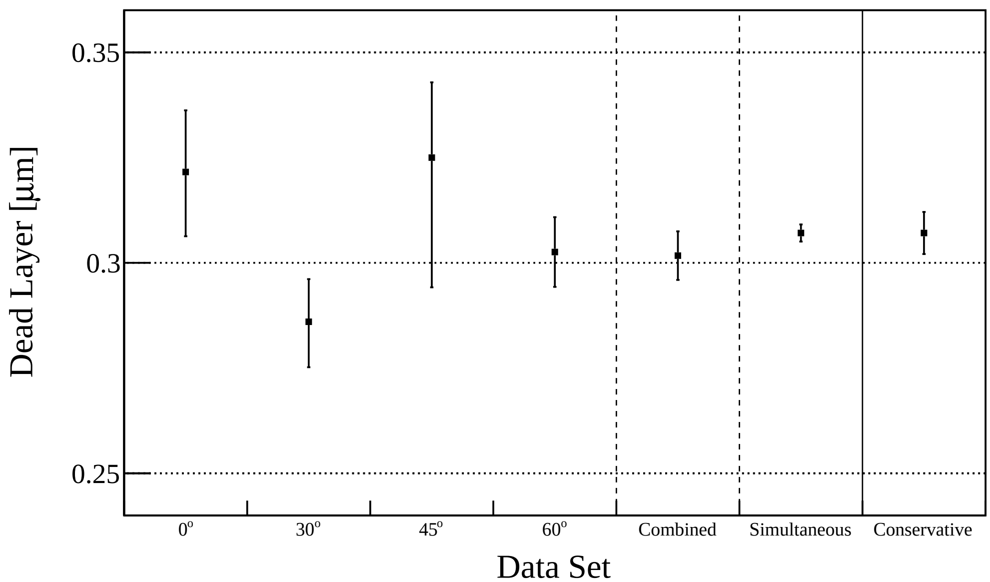

Figure 5.8: The dead layers extracted from the fits. The fits and errors for each individual data set are shown, as is the value from the combination of the separate fits. The simultaneous fit is also shown, both with the uncertainties as calculated in the fit (black) and the conservative uncertainties derived from the position-scan technique.

minima and calculate asymmetric error bars, although it is significantly slower than just using `MIGRAD` and `HESSE`.

The surface-alpha model was first fit to each data set independently. The extracted dead layers for each data set are shown in Fig. 5.8. The values and uncertainties do not reflect uncertainties in the source-position, however. These four values of the dead layer were combined to yield a best-fit value of $0.302 \pm 0.004\mu$m, also shown in Fig. 5.8. The surface-alpha model was also fit to the four data sets simultaneously by combining the four likelihood functions (one for each data set) and minimizing. The fits are shown in Fig. 5.9, and the residuals are plotted in Fig. 5.10.

The extracted dead layers and their uncertainties do not take into account possible uncertainties in the position of the source. Ideally, the source positions themselves could be used as variables for `MINUIT` to handle numerically. However, this proved impractical to implement. To see how the values of dead layer were affected by changes in source position,

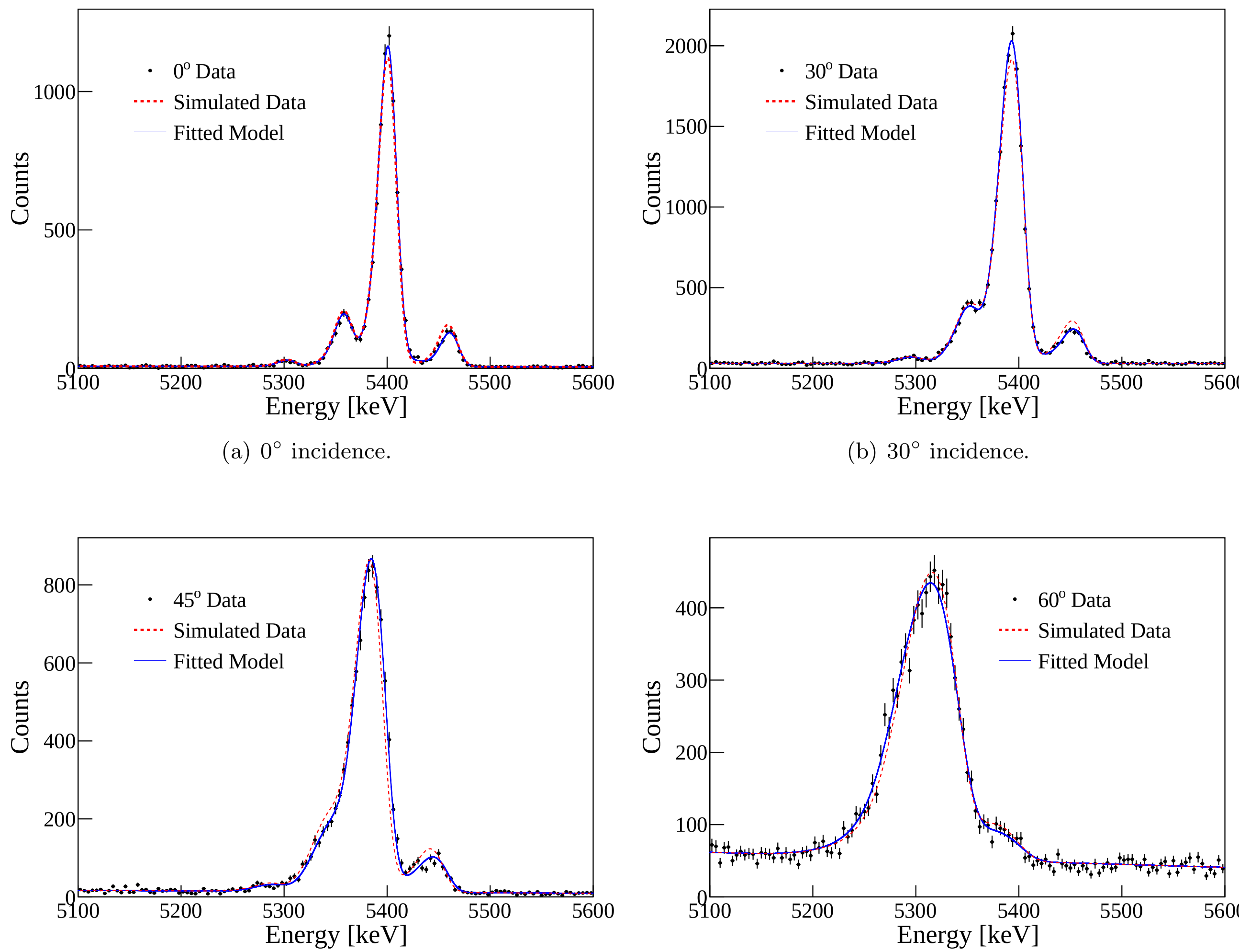

(a) 0° incidence.

(b) 30° incidence.

(c) 45° incidence.

(d) 60° incidence.

Figure 5.9: Surface-type alphas from ^{241}Am at incidence angles of 0°, 30°, 45°, and 60° with respect to the surface normal. Also shown are the analytic-model fits (solid line) and simulated spectra from Geant4 (dashed line). The simulated spectra have had an extra correction factor applied (Fig. 5.12).

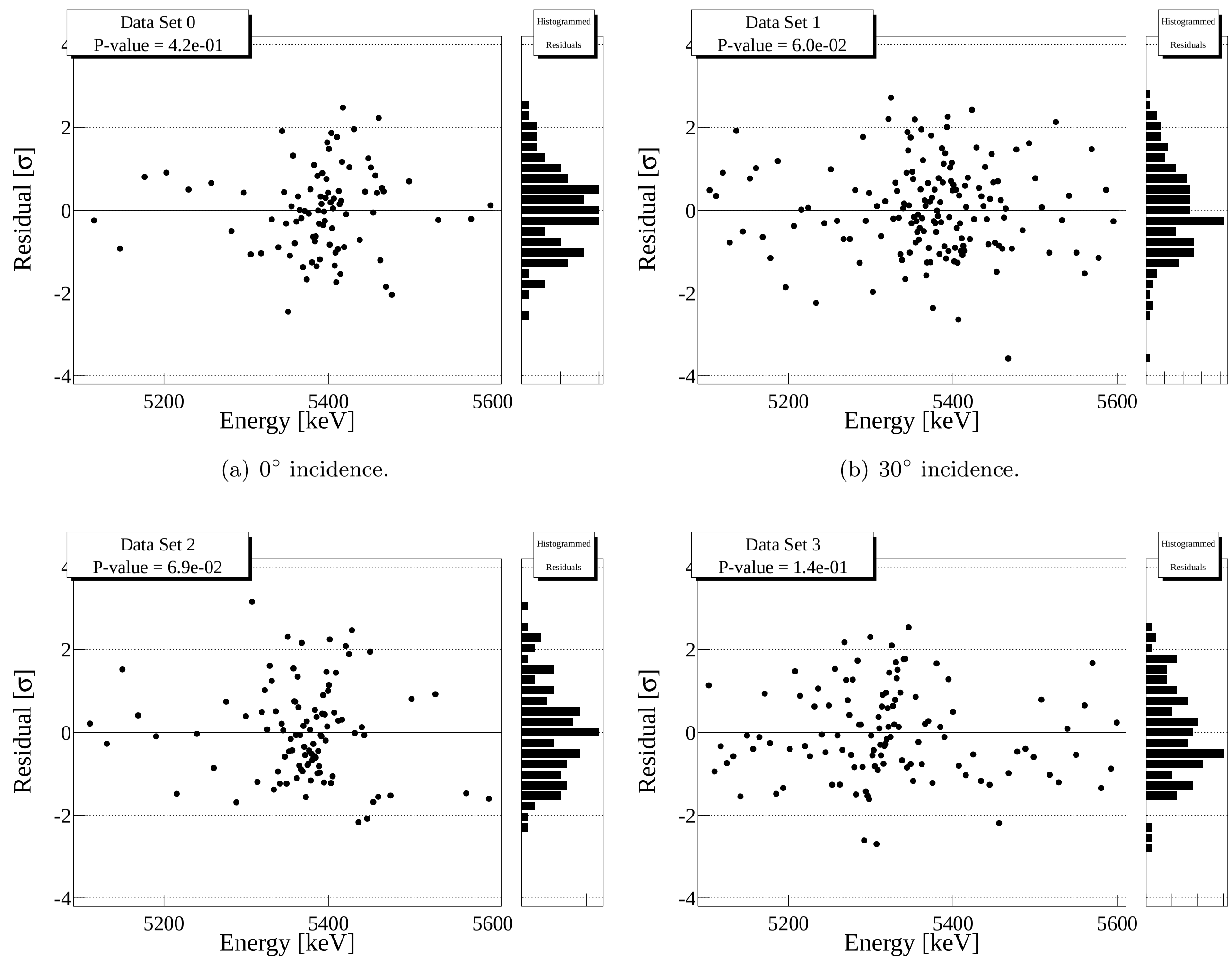

(a) 0° incidence.

(b) 30° incidence.

(c) 45° incidence.

(d) 60° incidence.

Figure 5.10: Residuals of simultaneous fit to surface-alpha data for four collimated-angle data sets.

an analysis program was written to loop over each position variable (e.g. height) and

- Scan the position variable over a range around the true value,
  - Fix the position parameter at that value
  - Perform the fit, letting everything else float,
  - Extract the dead layer,
- Plot the extracted dead layers as a function of source position.

Figure 5.11 shows an example of this plot, as well as the function $-\log L$ that was used to estimate the position uncertainty. The corresponding dead-layer uncertainties for each source position were then extracted by comparing the values within the position uncertainty interval, and these are tabulated in Table 5.3. A conservative total uncertainty from source position is shown in the table, assuming that all position uncertainties are uncorrelated. In reality, there is a large (negative) correlation between source parameters. For example, perturbing the collimation angle higher would nudge the dead layer lower, while perturbing the offset in the X-direction would require a larger dead layer. Perturbing the offset in the positive direction should require a larger collimation angle, and so the net effect on the dead layers will tend to cancel out somewhat. Adding the uncertainty from source position in quadrature with the uncertainty from the simultaneous fit results gives a conservative estimate of the uncertainty interval of the dead layer: 0.3071 ± 0.0054.

Both measurements of the dead layer are in good agreement with the value given by ORTEC in the detector's original detector specification and performance sheet.

5.2.3 Comparison With Simulation

The geometry of the test stand was imported into MaGe, a custom Geant4- and ROOT-based simulation framework developed by the MAJORANA and GERDA collaborations. A dead layer was simulated in the crystal surface as a step function, with any energy deposits within this dead region not collected (this assumption is the same as our analytic treatment). The simulated output consists of energy spectra for each of the collimated data sets. These

Table 5.3: Uncertainties in source-positions and the corresponding uncertainties in dead layer as extracted from the fits. The position offsets are as defined in Fig. 5.7. The uncertainties in position were translated into uncertainties in dead-layer as in Fig. 5.11.

Position Parameter	Position Uncertainty	Dead-Layer Uncertainty
	[mm]	[μm]
Δx_0	0.2	0.0008
Δx_{30}	0.04	0.000004
Δx_{45}	0.05	0.0004
Δx_{60}	0.04	0.003
Δy_{30}	0.01	0.00005
Δy_{45}	0.12	0.00003
Δy_{60}	0.01	0.0002
Δz_0	0.7	0.001
Δz_{30}	0.06	0.00001
Δz_{45}	0.08	0.0004
Δz_{60}	0.08	0.001
	[deg]	
$\Delta\theta_0$	2.41	0.0002
$\Delta\theta_{30}$	0.13	0.0002
$\Delta\theta_{45}$	0.13	0.0007
$\Delta\theta_{60}$	0.09	0.004
Total Uncertainty From Source Position		0.005

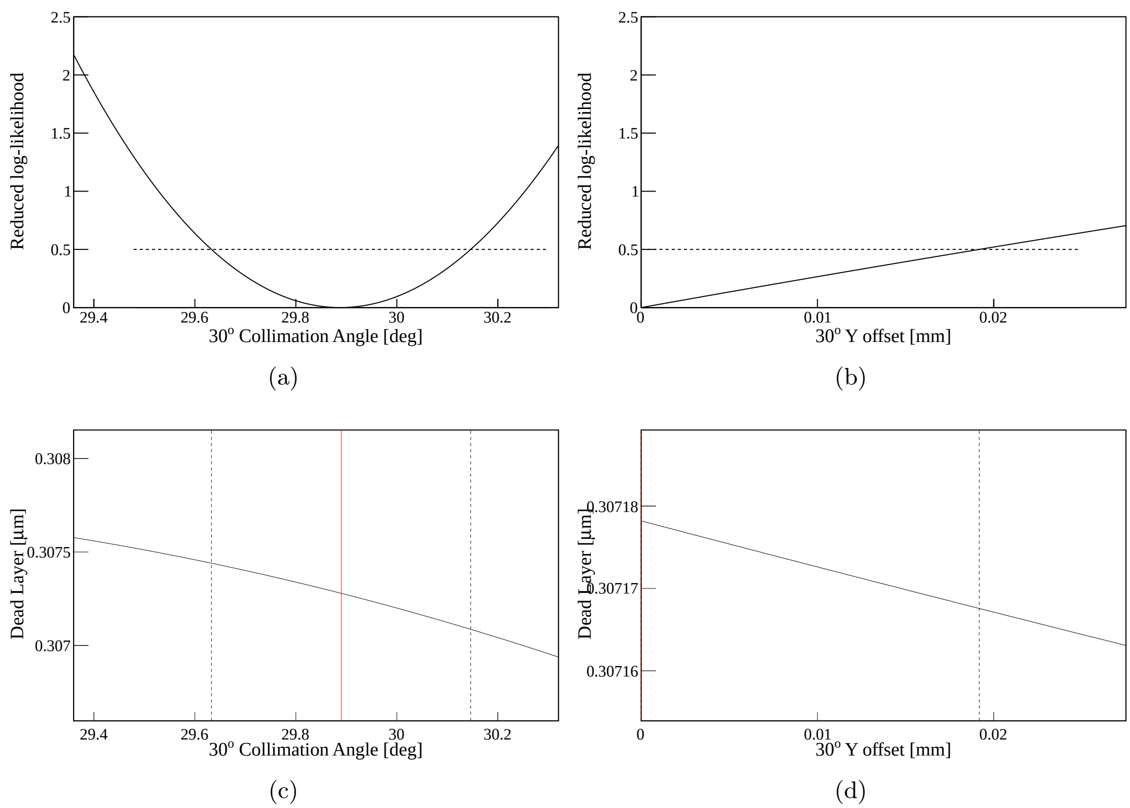

Figure 5.11: Dead-layer variation as a function of source position. These examples show the variation in collimation angle and y-offset (as defined in Fig. 5.7). The top plots show the reduced log-likelihood function at the minimum, with a dashed line at the min + 1/2 level (corresponding to the one-sigma uncertainty interval). The Y-offset is symmetric about zero, so only positive values are shown or allowed within the fit. The bottom plots show the variation in dead layer within the uncertainty intervals, with a red line indicating the most likely value and the black-dashed lines corresponding to the same uncertainty interval.

spectra were convolved with a detector-response function, i.e. a modified Gaussian incorporating the same skew parameter from the model fit. The width of the response function was determined by measuring the detector resolution from fits to gamma peaks in the detector (between 100 and 2600 keV), fitting the resolution values to a parameterized resolution function $f(E) = \alpha\sqrt{1 + \beta E}$ [32] (as in section 4.2.3), and extrapolating the resolution at 5.4 MeV from that function with the fitted values of α and β.

Comparing the simulations to the data reveal immediate discrepancies in both the width and energy offset of the peak structurer. The Geant4 simulation underestimates the width of an alpha peak. The difference in the energy offset is off by about 15 keV for alphas that do not travel through any dead layer. This is understandable, as nuclear recoil (as discussed above) was not built into the physics list used. Even taking this into account, there is still a large discrepency in ΔE that is largely linear in Δx. To quantify this discrepancy, a simulation of mono-energetic alphas incident on the surface was performed for a range of dead-layer traversals. The offset and width were compared with the prediction from the Bohr model. A second convolution was constructed — incorporating the differences in ΔE and σ — and applied to the simulated data. Figure 5.12 shows the extra energy offset and width parameter used in the convolution, as a function of length of dead layer traversed. These represent the amount of ΔE and $\Delta\sigma$ added to the simulation.

As derived in Equations 5.6 and 5.7, the energy offset and squared width (ΔE and σ^2) are proportional to the distance traveled within the dead region. It would seem that these discrepencies could come from a faulty value of dead layer then, either in the model or the simulation. This is not the case however; the correction terms in Fig. 5.12, particularly the linear terms (β in the figure), have opposite signs. Given the satisfactory fits of the model to the data, it seems most likely that the simulation is missing physics. The (corrected) simulated spectra for all four data sets are shown in Fig. 5.9 with the data and with the analytic fit.

The surface-alpha data taken with SANTA has provided the opportunity to test both a simple analytic model and a MaGe simulation. The fits of the model to the data were satisfactory, but the MaGe simulation required a correction factor in order to make it agree with the model and data. These model and simulations will be used in Chapter 7 to derive

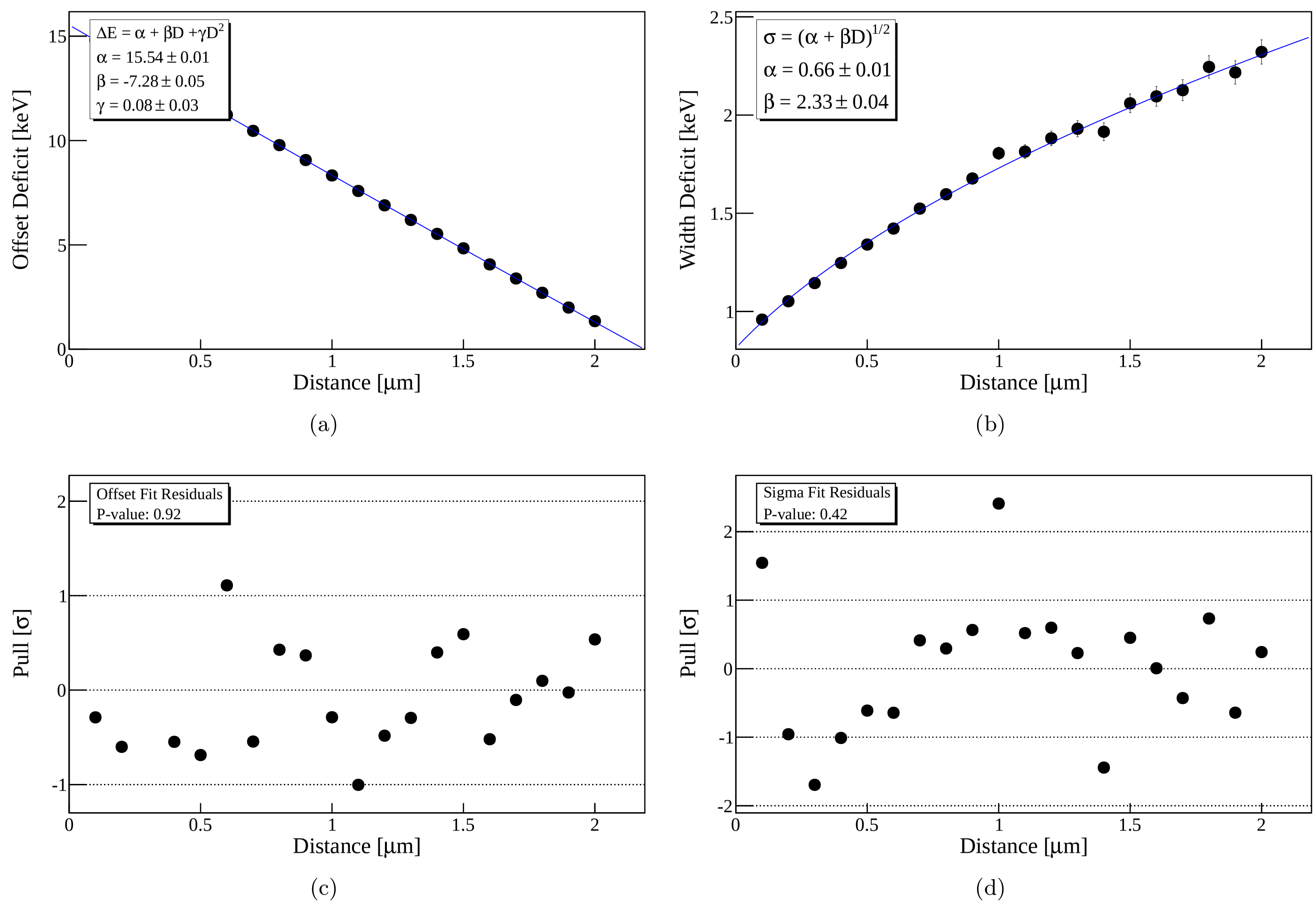

(a) (b)

(c) (d)

Figure 5.12: The deficits in energy offset and width from simulation, as compared with the data / model, were fit with a quadratic (for the energy offset) and a resolution function ($\sqrt{(\alpha + \beta D}$), as a function of distance the alpha travels through the dead region. These functions were then used to create a convolution function to correct the simulated data. The offset at zero distance is consistent with nuclear quenching for the alpha.

efficiencies for alpha decays in the $0\nu\beta\beta$ region-of-interest for ^{76}Ge.

5.3 Bulk-Alpha Backgrounds

The SANTA detector was used to take external-bulk alpha data as well as surface-alpha data. The goals of this were to compare simulations and an analytic model with bulk data.

5.3.1 Alphas from Thorium

The ^{232}Th decay chain (see Fig. 6.10 and Table 6.5) consists of 6 alphas between the energies of 4.01 and 8.79 MeV. Aside from the half-life of ^{232}Th (1.4×10^{10} y), the longest half-life in the chain is 5.76 y. Because of this, the chain is typically in equilibrium, particularly for the final 5 alphas in the chain. A thorium wire from Goodfellow [56] (0.22 mm in diameter, 4 cm long) was used as a source in the SANTA detector. The collimation cap in Fig. 5.5 was used, with the thorium wire coiled and anchored to the top of the cap and over the slit as in Fig. 5.13. This allowed alphas from within the bulk of the wire to have a free-shine path through the slit and onto the detector's face. The energy spectrum from these runs is shown in Fig. 5.14. The wire was $<$ 1 cm away from the detector's surface, and so there was substantial gamma pileup from ^{208}Tl and ^{228}Ac. This can be seen in the energy spectrum, particularly at 3126 keV (2615 keV + 511 keV), 3198 keV (2615 keV + 583 keV), and even 3709 keV (triple coincidence with 2615 keV, 511 keV, and 583 keV).

5.3.2 Analytic Model

A model, similar to that of the surface-type detector response, was constructed to describe bulk-type data on the detector. The typical range of an alpha in solid materials of interest (copper, lead, gold, germanium) is on the order 10's of μm. Thus only the outer portion of material facing the crystal will contribute alpha backgrounds. An alpha of original energy E_0, emitted in an external-bulk material at a depth d from the material surface at an angle θ with respect to the normal of that surface, will then lose an average energy similar to Eq. 5.7 where dE/dx is a function of the alpha's energy and distance traveled. Similarly, energy straggling will widen the resulting peak. The energy-straggling spectrum $f(E, E_0, d, \theta)$ from

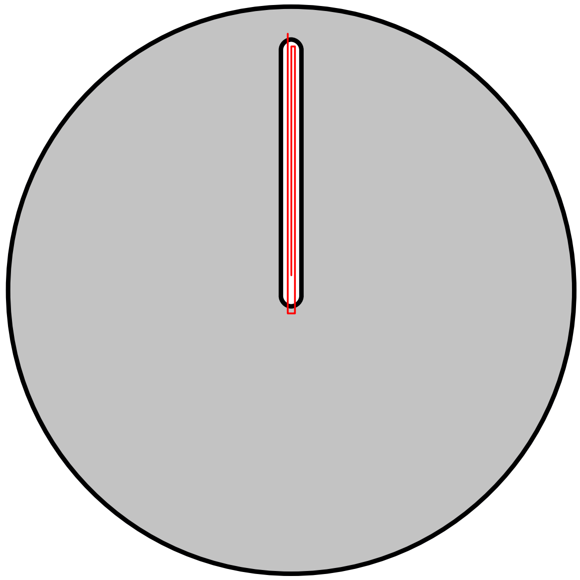

Figure 5.13: Top-down view of the slit-collimation cap. The thorium-wire (red line) is coiled and anchored above the slit on top of the plate, allowing direct-alpha (and beta/gamma) shine on to the crystal below.

an alpha of initial energy E_0 at a depth d (in μm) emitted at an angle θ would then be given as

$$
\begin{aligned}
f\left(E, E_0, d, \theta\right) &= \frac{1}{\sqrt{2\pi}\sigma} \exp\left(-\frac{E + E_0 - \Delta E(d,\theta)}{2\sigma^2}\right) \\
\sigma^2 &= 4\pi N_a r_e^2 (m_e c^2)^2 \rho \frac{Z}{A} \Delta x \\
&= 284.9 \frac{d}{\cos\theta} \quad \text{keV} \\
\Delta E(d,\theta) &= \int_0^{d/\cos\theta} \frac{dE}{dx} dx \quad \text{keV.}
\end{aligned}
\tag{5.13}
$$

where we once again assume a Bohr model of energy straggling and σ^2 is calculated using ρ, Z, and A of thorium. While f could be described with an exponentially-modified Gaussian as in Section 5.2, such details are washed out in practice because of the continuum nature of the energy spectrum as f is integrated over θ and d. A regular (non-modified) Gaussian was used instead. The model spectrum for a particular alpha with initial energy E_0 is

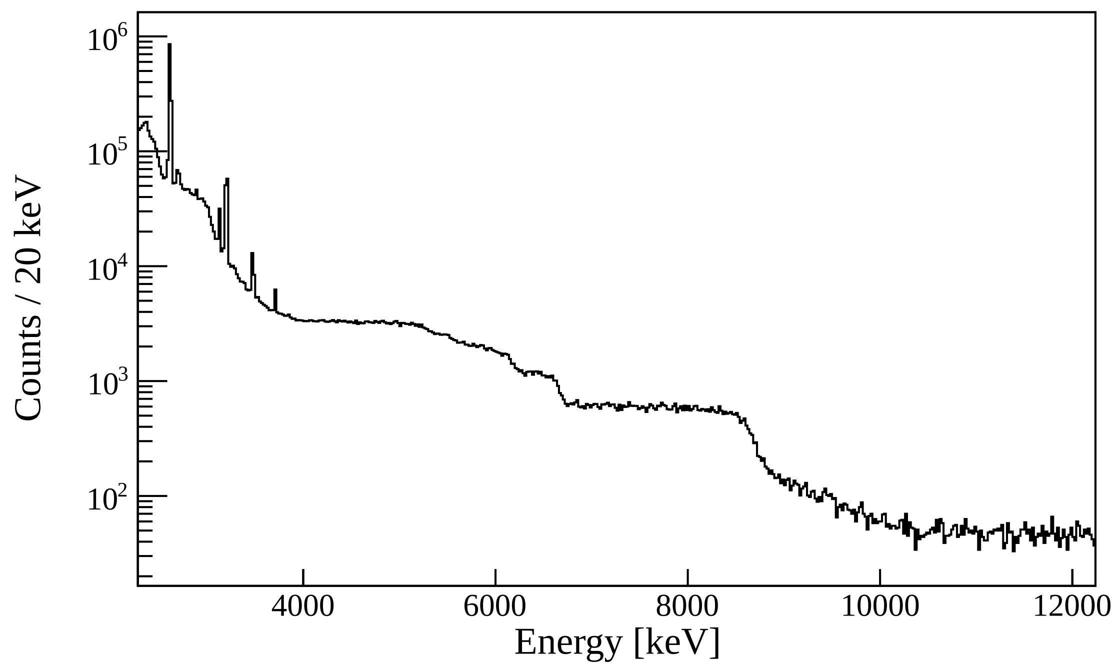

Figure 5.14: Energy spectrum from the thorium-wire run. The step-like structure is from thorium alphas. The extremely-close placement of the source next to the detector resulted in significant pileup of the ^{208}Tl gamma lines 511 keV, 583 keV and 2615 keV. There is also pileup between the ^{222}Po alpha (8.8 MeV) and ^{212}Bi beta, noticeable between the step at 8.8 MeV and 11 MeV. Counts above 11 MeV originate from cosmic rays.

then found by integrating Eq. 5.13 over valid values of θ and d (that is, θ and d such that $\Delta E(\theta, d) \leq E_0$). Values for dE/dx were taken from alpha stopping-power and range tables [57], and this integration was performed for all the alphas in the ^{232}Th decay chain. The corresponding energy spectra were then summed, assuming the chain to be in secular equilibrium. This assumption is valid in our comparison with our data because all alpha decays in the ^{232}Th chain, except the first, happen within days of each other (Table 6.5). The first alpha decay (^{232}Th) emits a 4 MeV alpha which is not discernible below the beta continuum in the data set (Fig. 5.14).

The fast alpha decay (300 ns) of ^{212}Po, coming after the beta decay of ^{212}Bi, occasionally results in pileup in the detector of the alpha (maximum energy deposited: 8.8 MeV) and the beta (endpoint: 2252 keV, intensity: 55.4%). To treat this, the modeled ^{212}Po alpha spectrum was convolved with the beta spectrum of ^{212}Bi. A fit was performed to the data consisting of a histogram with all of the alpha spectra except ^{212}Po, a histogram with an unmodified ^{212}Po spectrum, a histogram with a convolved ^{212}Po spectrum, and a background histogram taken with no source. The resultant model spectrum is compared with the data in Fig. 5.15. The fit is satisfactory everywhere except for at the "steps" corresponding to the initial kinetic energies of the alphas (particularly for ^{212}Po at 8.8 MeV. This results in a low P-value for the fit. The model does, however, capture the shape of the data quite well otherwise. The discrepency at 4 MeV is due to the gamma- and beta- pileup interactions from ^{208}Tl.

5.4 Conclusions

A test stand was built for the purpose of characterizing the response of an HPGe detector to surface- and bulk- alpha backgrounds. Analytic models were constructed to describe both the surface- and bulk-data, and the comparisons of model and data were satisfactory. The geometries used in the test stand were simulated in MaGe, and the resultant simulated energy spectra were not as satisfactory. An empirically-derived corrective convolution was applied to the surface-simulation data, resulting in satisfactory comparison between simulation and test-stand data.

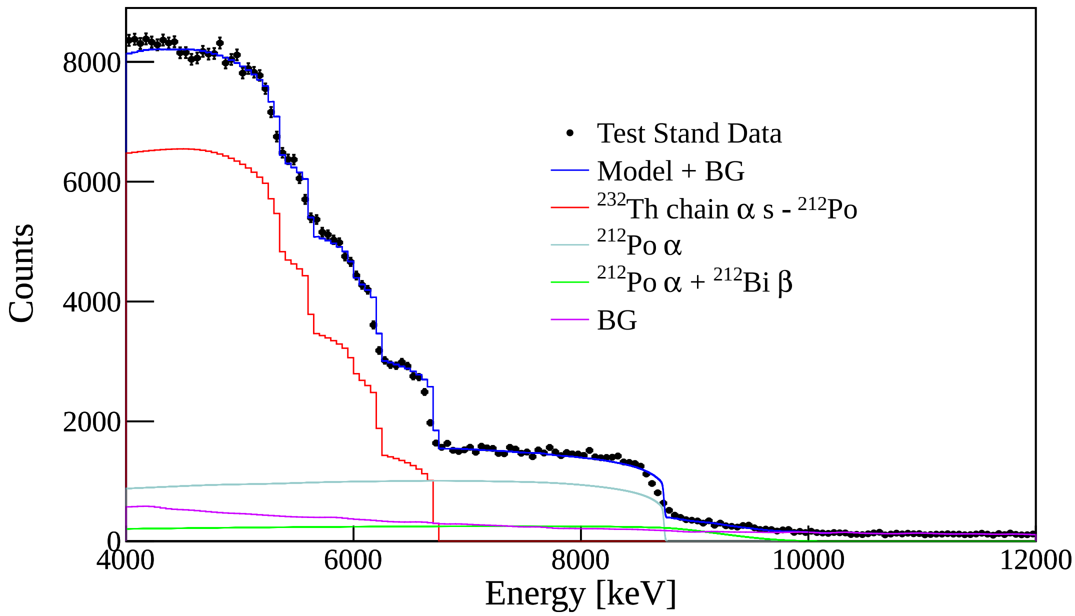

(a)

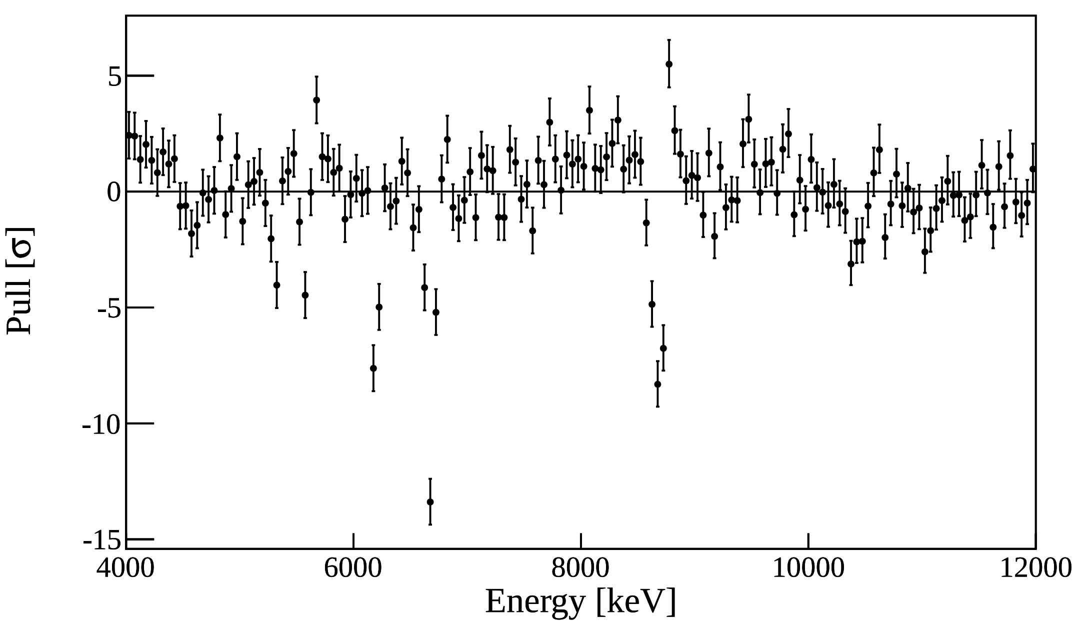

(b)

Figure 5.15: High-energy spectrum of alphas from thorium wire on the HPGe surface. The alphas were modeled as in Eq. 5.13. The ^{212}Po alpha was handled separately, as explained in the text. The background was taken from a non-source run with the same detector. The fit is satisfactory except for right at the steps.

Chapter 6

ALPHA BACKGROUNDS IN A LOW-BACKGROUND DETECTOR: WIPPN

The WIPPn detector is an N-type HPGe detector (Table 6.1), constructed by Princeton-Gamma Tech (PGT), that has been underground at the Waste Isolation Pilot Plant (WIPP) since 1998. Originally used underground in a dark matter background study [58], in 2005 it was resurrected, fitted into a new shield, and set up as a low-background counting facility. A prominent peak at 5.3 MeV in the energy spectrum is consistent with the alpha from ^{210}Po (Fig. 6.1). This detector has provided an opportunity to study backgrounds from alpha decays *in situ* in an established, underground HPGe detector.

6.1 Underground N-type HPGe detector

6.1.1 The Waste Isolation Pilot Plant (WIPP)

WIPP is a pilot project to address the long-term disposal and storage of transuranic ($Z > 92$), low-level, mixed, defense-related waste (e.g. contaminated tools, gloves, soil, etc...). It is located approximately 30 miles southeast of Carlsbad in southeastern New Mexico, USA. The site is on the edge of the Delaware basin, an area of 25,000 km^2 encompassing portions of western Texas and southeastern New Mexico. The basin filled with sediment and sea water during the Permian era (300 MYA - 250 MYA), forming the Delaware Sea. The basin was eventually cut off from external water sources at the end of the Permian, drying out into the arid basin it is today. Minerals precipitated out of the briny sea during evaporation, first gypsum and calcite, and later halite and potassium salts. These last precipitates became the Salado Formation, a 250 feet thick layer of salt. It is within this formation that WIPP was constructed. At 655 meters (2150 feet, 1585 m.w.e. [58]) below the surface, WIPP is a single-level salt mine where waste is stored in specially designed rooms or "panels" (Fig. 6.2). While all underground cavities will shift (eventually caving in), salt deposits are

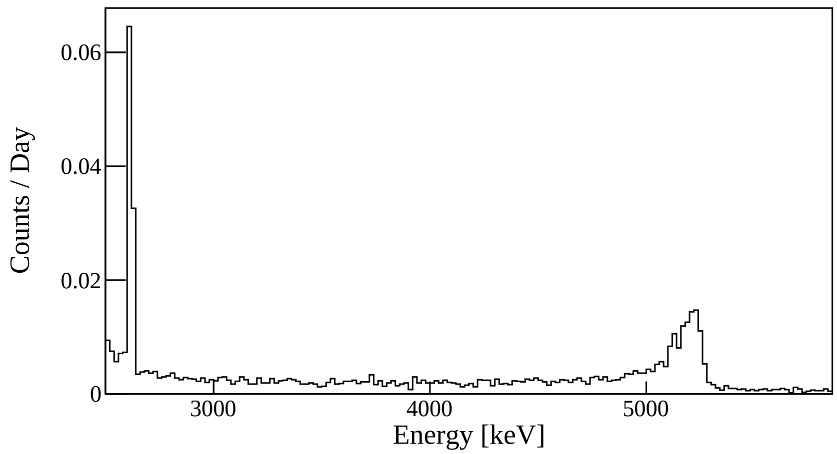

Figure 6.1: The 5.3 MeV peak in the high-energy spectrum from the WIPPn detector. Also shown is the 2615 keV gamma from ^{208}Tl.

particularly vulnerable to movement. A wall in a salt cavity will move ∼1-2 in/year without structural reinforcement, i.e. rock bolts. Left alone and unsupported, a salt cavity will eventually collapse and close in on itself. This property, combined with the lack of a nearby water table, makes salt a desirable candidate for deposition of radioactive waste. The Waste Isolation Pilot Plant was approved by the United States Congress in 1979, and construction was begun in 1981. Waste handling and deposition commenced in 2001, and waste-storage panels (see Fig. 6.2) have been continuously excavated and filled since.

WIPP is contracted to run by the Department of Energy, with a secondary mission to provide space and facilities support for science projects. As of this writing, there is space at WIPP utilized by the Majorana collaboration and by another $0\nu\beta\beta$ experiment using enriched xenon as source (EXO). The Dark Matter TPC (DMTPC) experiment is also using space at WIPP. Previous uses have included testing of the Sudbury Neutrino Observatory's Neutral Current Detectors (SNO NCDs). WIPP is also used for research in geology and biology[59].

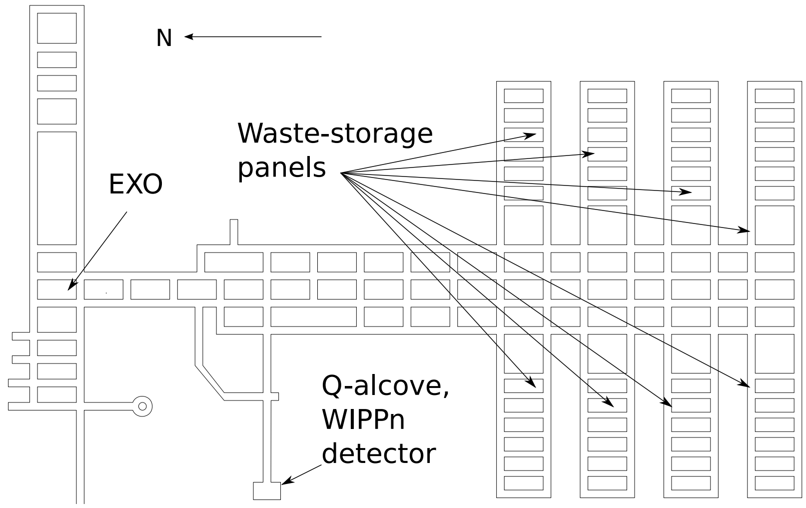

Figure 6.2: WIPP underground facility layout. The facility is approximately 1 mile in length, north-south.

6.1.2 Cleanroom, Detector, and Shielding

A cleanroom was constructed in the Q-alcove of WIPP in 2004 for the purpose of housing MEGA, a multiple-element gamma-counting facility [60]. An N-type HPGe detector, located underground at WIPP since 1998 and originally used in a dark-matter background testing experiment [2], was resurrected for use in MAJORANA as a low-background counting detector and installed in this cleanroom. The detector was first cooled and biased in July, 2005. Clean-lead bricks and a stainless steel radon-exclusion box were procured for the detector and were installed in August, 2005. The detector characteristics, as supplied by the manufacturer (Princeton Gamma Tech), are shown in Table 6.1.

The WIPPn detector has — as of 2010 — been run in two separate shield configurations since 2005 (Table 6.2). These shield configurations are shown in Fig. 6.3. Configuration I consists of, from outside in, a radon-exclusion box, 10 cm of lead, and 5 cm of copper. This was the original configuration, constructed in 2005, and is used for most sample counting. The detector cryostat (outer can) was replaced in June of 2006, and the shield was dismantled and reassembled into the same configuration at that time. The shield was again dismantled and reassembled — this time without the inside copper lining — in 2007 to study the efficacy

Table 6.1: Detector specifications of the WIPPn detector. [2]

Manufacturing Information			
Detector Model No.	*NIGC2020*	Cryostat type	*NPR30*
Serial No.	*1724*	Year of manufacture	*1985*
Dimensions			
Crystal diameter	*51.0 mm*	Crystal length	*44.2 mm*
Be window to detector	*5 mm*	Active volume (nominal)	*87* cm^3

Table 6.2: Shield configurations in which the WIPPn detector has been run.

Setup	Time Period	Notes
I	Feb 2006 - June 2006	Shield configuration I (Pb-Cu), original cryostat
II	July 2006 - Feb 2007	Shield configuration I, new cryostat
III	May 2007 - Sep 2008	Shield configuration II (no copper)
IV	Sep 2008 - Present	Shield configuration I
V	Dec 2008 - Present	Shield configuration I and muon-veto panel

of removing ^{60}Co by electroforming copper underground. The shield was reconstructed back into configuration I in September, 2008, and it is in this configuration that it remains today. A muon-veto panel was installed on top of the shield in December, 2008.

6.1.3 Data acquisition and bias monitoring

As explained in Section 4.1, the role of data acquisition, bias supply, and preamp power is handled by a DGF (Digital Gamma Finder) Polaris waveform digitizer and spectrometer, made by X-ray Instrumentation Associates (XIA). The Polaris supplies the bias voltage to the detector (-4000 V) with a logical inhibit input. The leakage current across an HPGe detector rises with temperature, and a custom feedback voltage monitor was built at Los Alamos National Lab to detect aberrant feedback voltage. The monitor reads the feedback voltage from the detector preamp (V_{fb}, Fig. 6.4). If V_{fb} goes above a prescribed limit for a long-enough time, the monitor sends an inhibit signal to the Polaris, indicating that the voltage to the detector should be cut. This detector shutdown is a safety mechanism against

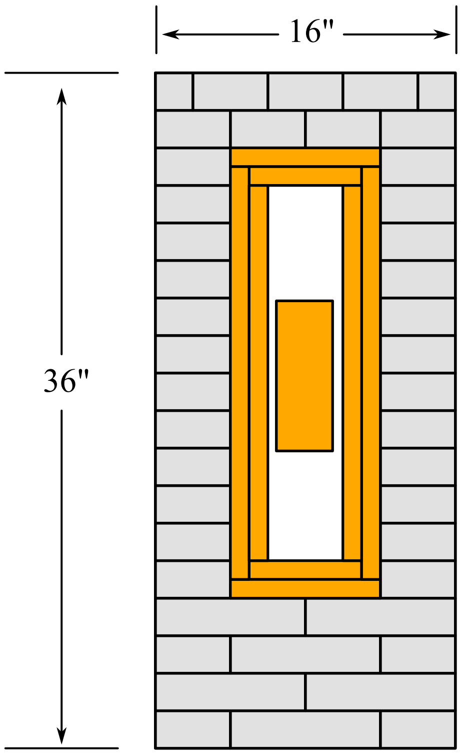

(a) WIPPn lead-copper shield configuration (Configuration I)

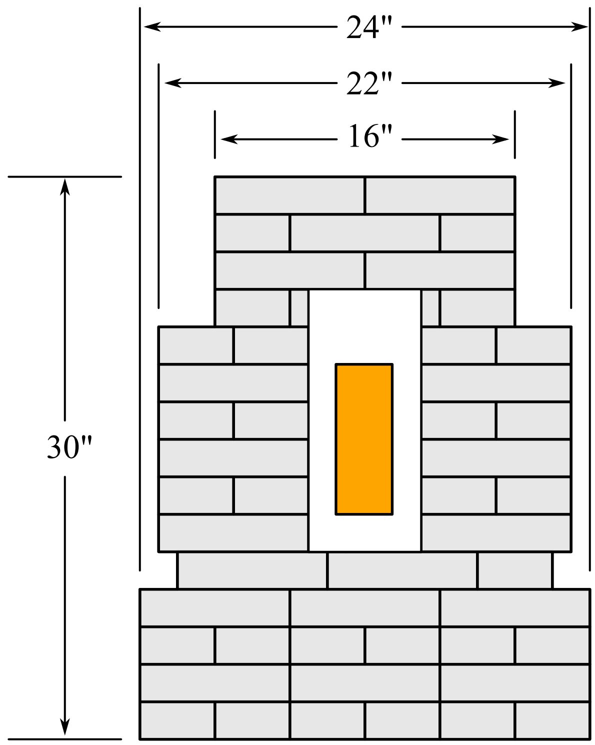

(b) WIPPn lead-only shield configuration (Configuration II)

Figure 6.3: WIPPn Shield Configurations. The shield configuration in (a) is the normal configuration. The configuration in (b) was constructed and used during a gamma-counting campaign looking at ^{60}Co in copper samples. The orange-shaded rectangle in the middle is the cryostat for the detector. Not shown is the arm connecting the bottom of the cryostat to the dewar outside of the lead shield. This arm also provides the routing for the detector's electronics.

excessive leakage current, e.g. from the warmup of the detector. The monitor has two modes: "on" and "standby." The detector is biased (voltage applied) in the standby mode, as the process of biasing a detector produces large potential differences across the detector that are not encountered in typical operation. These voltage swings allow for testing of the voltage-feedback monitor; a working monitor in the "on" mode will trip the bias inhibit if the bias is changed quickly.

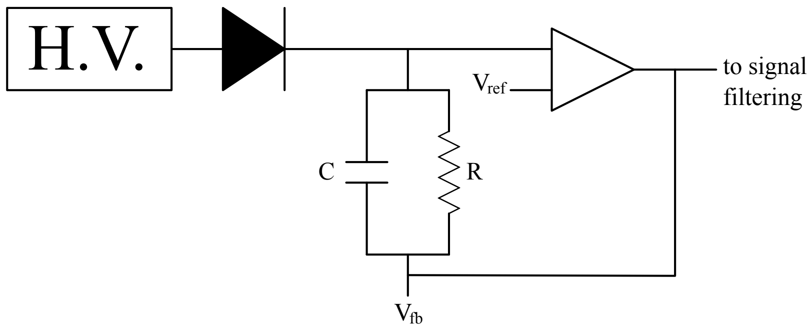

Figure 6.4: Simplified schematic of a preamplifier for an HPGe detector. The detector (diode) is reversed bias against the (negative) high-voltage. Excessive feedback current across the detector will result in a large difference between the inputs of the amplifier. The amplifier attempts to cancel this by increasing the feedback voltage (V_{fb}). This voltage is monitored to guard against excessive leakage current.

6.2 Low-energy background (E < 2700 keV)

6.2.1 Setup I: original cryostat and lead-copper shielding

After a first cool-down and biasing in July, 2005, the WIPPn shield was designed and built in summer and fall, 2005. The detector was cooled and biased again in November. During testing of the feedback-voltage monitor, it was discovered that the monitor failed to trip the bias inhibit function on the Polaris. The logical function of the monitor was working, but the output inhibit signal did not provide enough current to register with the Polaris. This was fixed in February, 2007 by inserting a simple transistor-resistor follower to the output of the monitor. This allowed enough current to successfully trip the Polaris bias inhibit in subsequent testing. Background data were collected in this original configuration (shield configuration I, original detector cryostat) from 9 February, 2006 through 30 June, 2006 The total livetime for these background runs is 40.31 days. No calibration runs were taken during this period because there was no available source yet. Calibration was performed using the background peaks present in the natural spectrum.

The dynamic range of these original background runs was set such that the highest energy events were around 7 MeV. The low-energy noise threshold was $\sim$ 80 keV. The average count rate was $\sim$ 6 counts/minute. There were prominent gamma lines from the ^{232}Th and lower

^{238}U decay chains, ^{40}K (1460.8 keV), ^{137}Cs (661.7 keV), and ^{60}Co (1173.2 and 1332.5 keV). There were also lines from ^{234m}Pa at 766.4 keV and 1001.0 keV. ^{234m}Pa is the second decay after ^{238}U, and so the existence of these gamma lines implies an upper ^{238}U chain source. This chain has several long-lived "bottlenecks" (^{234}U(2.45×10^5 y), ^{230}Th (7.54×10^4y), ^{226}Ra(1622 y)) as well as a natural break in the chain at ^{222}Rn. The result is that the ^{238}U chain is often found out of equilibrium. This is in contrast to the ^{232}Th chain, the longest half-life of which is 5.76 years (after ^{232}Th itself).

The energy deposits from betas and gammas in the ^{238}U and ^{232}Th decay chains go up to 2614 keV in the energy spectrum, above which is a significant drop in count rate.. There is also a prominent peak above this, just above 5 MeV (Fig. 6.1). This high-energy signature points to either alpha-related contamination or cosmic-generated events, and the peak structure strongly indicates an alpha source. Alphas from the decay chains with energies between 5 and 6 MeV are ^{222}Rn, ^{210}Po, ^{228}Th, and ^{224}Ra. The peak is unlikely to originate from ^{222}Rn because one would also expect alphas from ^{218}Po (6.02 MeV) — which follows within minutes — and possibly from ^{226}Ra (4.78 MeV), but no such peak structure can be found at those other energies. A similar argument applies to ^{228}Th and ^{224}Ra, as subsequent short-lived alpha decays of ^{224}Ra would produce comparable peaks at 6.3 MeV and 6.8 MeV. This leaves ^{210}Po as the only other candidate for this peak.

6.2.2 Additional Pb Shield: Bremsstrahlung from ^{210}Pb

A thin (1/4" thick) sheet of pliable lead was placed inside of the copper shielding and around the detector's cryostat. The purpose of the placement was to attempt to shield the detector from ^{60}Co gammas originating from the copper lining. The background-count rate jumped by a factor of 2 during this time. Figure 6.5 shows the initial background spectrum and the spectrum with the lead-sheet added. There is no qualitative difference above $\sim$ 1000 keV (Fig. 6.5), but there is definite disparity below this energy. The hypothesis was that ^{210}Pb in the lead sheeting was responsible. Specifically, ^{210}Pb decays to ^{210}Bi with a 22-year half-life. ^{210}Bi then decays with a short 5 day half-life, emitting a beta with a spectrum endpoint at 1.16 MeV. These betas are stopped in the lead, but the resultant bremsstrahlung

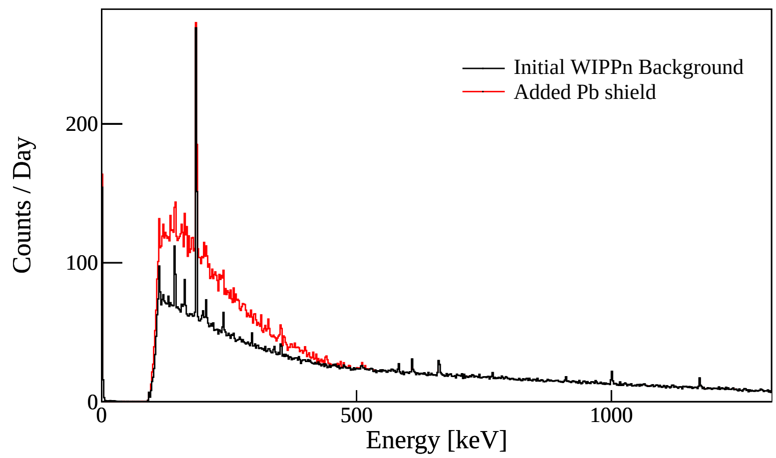

(a)

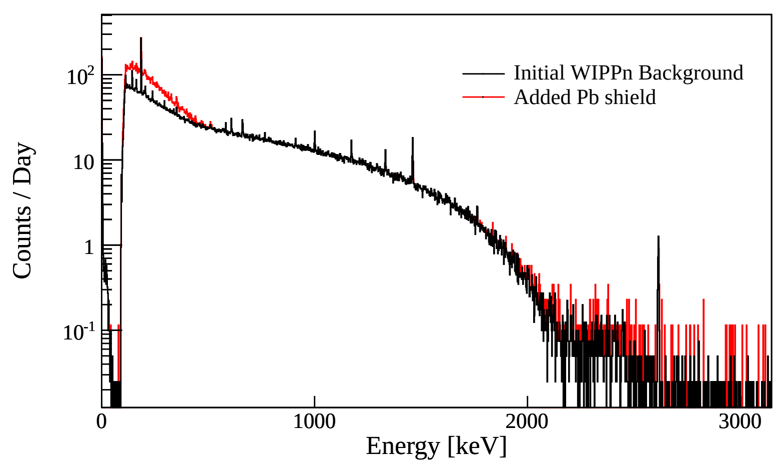

(b)

Figure 6.5: Comparison of the WIPPn background spectrum. The black histogram is the initial background spectrum and corresponds to 40.31 days of livetime. The red histogram is the background taken with an added sheet of lead and corresponds to 8.71 days of livetime.

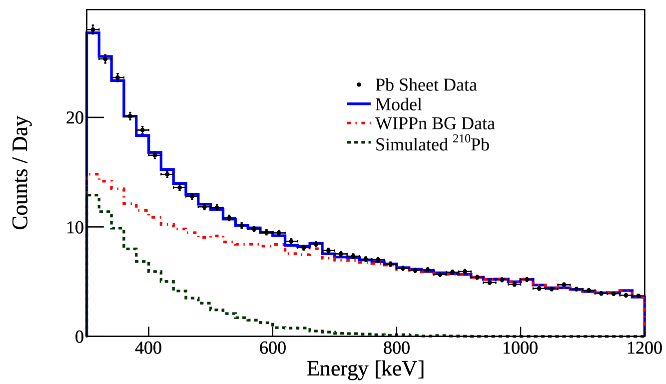

(a) Lower-energy fit

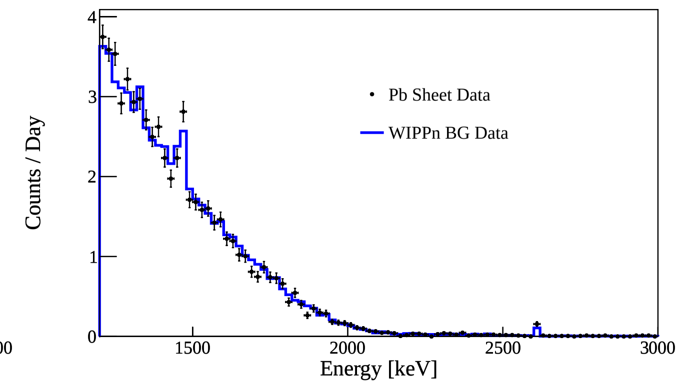

(b) Higher-energy fit

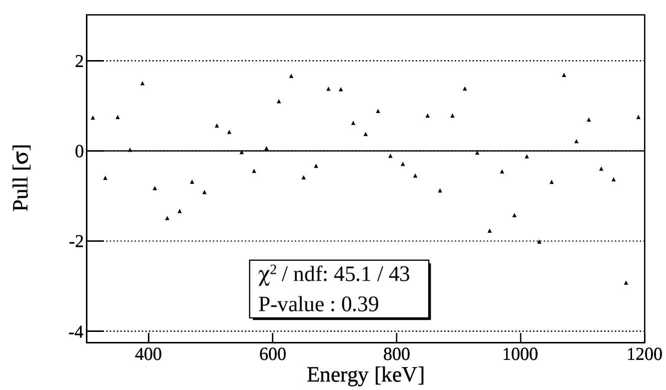

(c) Lower-energy pulls

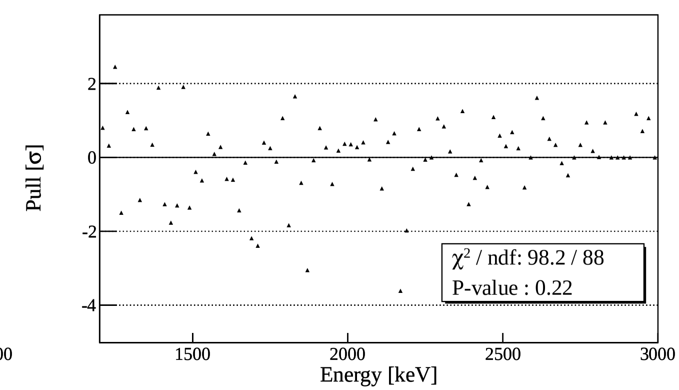

(d) Higher-energy pulls

Figure 6.6: Fitting the Pb-sheet data with a model pdf. The model consists of two shape pdfs: a pdf composed of the original (non-Pb sheet) cryostat background data and a pdf of the bremsstrahlung from ^{210}Pb/^{210}Bi decays in the Pb sheet (simulated from MaGe). The ^{210}Bi beta spectrum ends at 1160 keV, so a separate fit comparing WIPPn background and Pb-sheet data above the beta spectrum was also performed (b). The residual pulls for the two fits are shown in (c) and (d).

Table 6.3: Measured ^{60}Co rates in the WIPPn detector for the original cryostat and with the added Pb sheet.

Energy	Original Cryostat			With Pb Sheet			% Difference
(keV)	(No. / Day)	P-value	Sig.	(No. / Day)	P-value	Sig.	
1173	10.31 ± 0.99	0.38	13.08	6.58 ± 1.97	0.35	4.36	-36.2 ± 11.4
1332	8.57 ± 0.86	0.09	13.50	6.18 ± 2.00	0.23	4.97	-27.9 ± 9.5

photons make it out of the lead and into the detector.

A simulation was run in MaGe to test the hypothesis. The WIPPn geometry in MaGe was modified to include a lead sheet of similar dimensions to the lead inside of the WIPPn shield. Decays of ^{210}Pb inside of the lead sheet were generated and allowed to decay all of the way to ^{210}Po. The simulation results were histogrammed and a pdf model was created. The model pdf consisted of the (non-Pb) WIPPn background data and a pdf created from the simulated bremsstrahlung spectrum. This model was fit to the subtracted energy spectrum with the results shown in Fig. 6.6. A separate fit was performed above the ^{210}Bi endpoint between the non-Pb data and the Pb-sheet data (with no simulated bremsstrahlung component), and the results of this fit are also shown in Fig. 6.6. The spectral fit above the endpoint was found to be reasonable (P-value of 0.22), as was the background + model fit. The rates of the 1173 and 1332 keV gammas from ^{60}Co, for with and without the Pb-sheet, are compared in Table 6.3. A small reduction was found in the rates with the addition of the lead sheet.

6.2.3 Replacement cryostat: Upper ^{238}U Chain

The gamma lines from the first phase showed the “usual suspects” in background counting with HPGe detectors, namely ^{40}K, and gammas from the ^{232}Th (^{208}Tl and ^{228}Ac) and the lower ^{238}U (particularly ^{214}Bi). A somewhat surprising find was the line at 1001 keV from ^{234m}Pa. The gammas from ^{234m}Pa have small relative intensities (0.107% for the 743 keV line and 0.842% for the 1001 keV line), but the count rate of the 1001 keV gamma was found to be higher than the 609 keV from ^{214}Bi (45% relative intensity). This suggests the presence of ^{238}U chain out of equilibrium. The cryostat of the WIPPn detector contained a beryllium

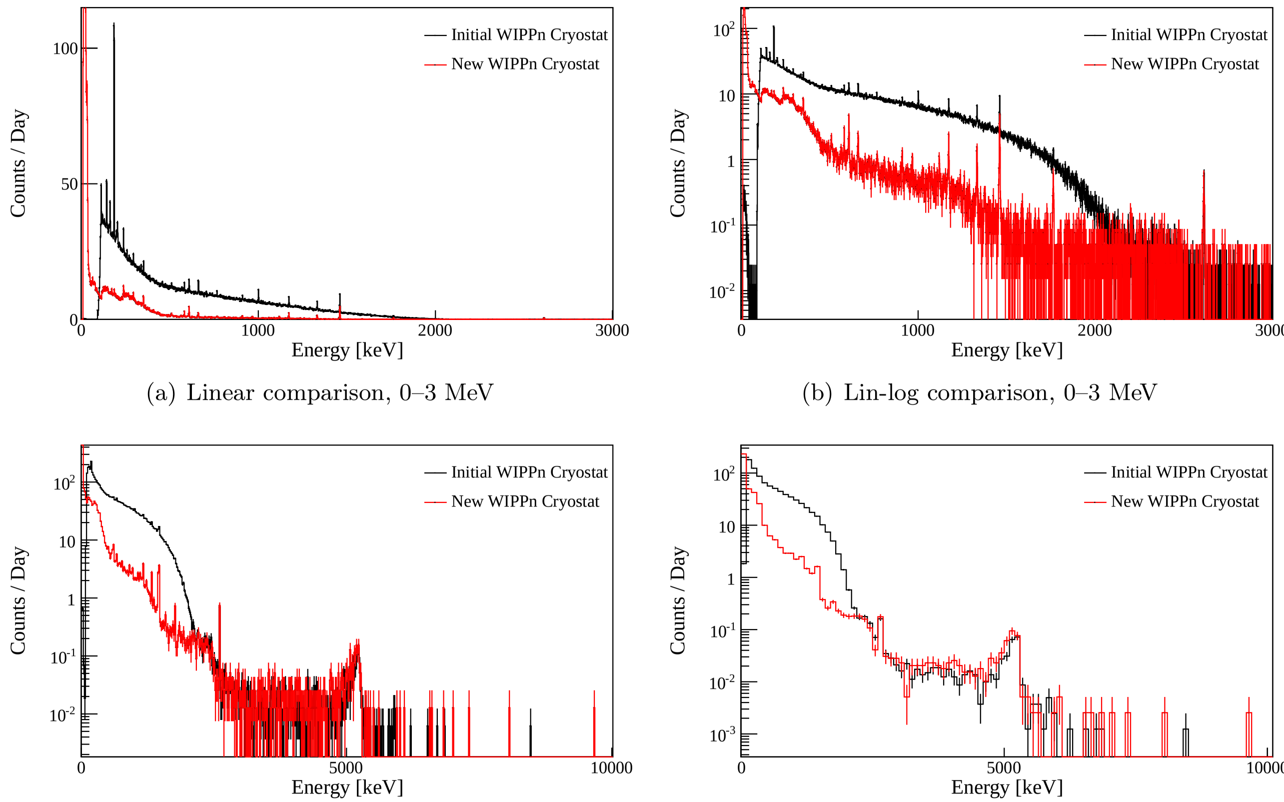

(a) Linear comparison, 0–3 MeV

(b) Lin-log comparison, 0–3 MeV

(c) Lin-log comparison, 10 keV bins

(d) Lin-log comparison, 20 keV bins

Figure 6.7: The first two phases of WIPPn background data (Setup I with 40.31 days of livetiem in black, Setup II with 19.55 days of live time in red). Setup I was taken with the original cryostat inside of a copper-lined lead shield. The count rate above 50 keV was 190 ± 1 mHz, or 11.4 counts per minute. Setup II was taken with a new cryostat. The count rate above 50 keV for this setup was 44.6 ± 0.7 mHz, or 2.7 counts per minute. The first runs of Setup II had a large noise peak at low energies, and the energy threshold was moved up to about 100 keV to take care of this. The large disparity in count rates is visible as a difference in the energy spectra up to ~ 2 MeV, corresponding to the ^{234m}Pa beta spectrum. (a) and (b) shows the disparity up to 3 MeV, while (c-d) show the energy spectrum up to 10 MeV on a lin-log scale. Figures (c) and (d) have been rebinned to enhance the broad structure aspects. Also clearly visible is a peak at 5.3 MeV from ^{210}Po alphas.

Table 6.4: A comparison of gamma lines in the original and new cryostat for the WIPPn detector. Only lines with p-value fits of > 0.05 and significance factors of > 10 were used for this comparison. The change of the cryostat had no statistical effect on gammas from ^{40}K, the ^{232}Th chain (^{208}Tl), or the lower ^{238}U chain (^{214}Pb, ^{214}Bi). There was a slight decrease in the amount of ^{60}Co. The 1001.03 keV gamma from ^{234m}Pa is too low to measure in the new cryostat, and the amount of ^{137}Cs saw a large reduction.

Source	Energy (keV)	Original Rate (Counts / Day)	New Rate (Counts / Day)	% Difference
$^{234\mathrm{m}}$Pa	1001.03	14.40±1.22	N/A	
^{214}Pb	351.93	13.43±1.54	13.54±1.61	0.8±16.6
^{214}Bi	609.32	13.19±1.39	12.29±1.10	-6.8±13.4
^{208}Tl	2614.51	2.68±0.26	2.74±0.39	2.2±17.5
^{40}K	1460.82	22.77±1.06	20.55±1.06	-9.7±6.6
^{60}Co	1173.23	10.22±1.06	7.14±0.77	-30.1±12.8
	1332.49	8.87±0.87	6.84±0.67	-22.9±12.4
^{137}Cs	661.66	20.06±1.58	9.48±1.02	-52.7±9.4

window on the outer face. This window is often included in N-type HPGe detectors because it is quite thin while still holding vacuum, thus allowing for the detection of lower-energy gamma and x-ray lines without the attenuation from aluminum or copper. This window was suspected of being the source of $^{234\mathrm{m}}$Pa in the energy spectrum, and the entire outer can of the detector was removed and replaced in July, 2006. The background spectrum for this second phase of WIPPn (Setup II in Table 6.2) was found to be substantially different than Setup I. Background data from this phase were collected starting in July, 2006 and continued until the Polaris had a severe malfunction and required servicing by XIA in February, 2007. The background spectrum from this phase represents 64.44 days of livetime. This spectrum is compared with the original phase (Setup I) in Fig. 6.7. The count rate dropped from 3.15 ± 0.05 counts/minute to 0.61 ± 0.02 counts/minute. The most noticeable feature is the deficit of counts below ~ 2 MeV. This deficit is consistent with the lack of a beta spectrum from $^{234\mathrm{m}}$Pa (endpoint 2269 keV). This is also corroborated by the lack of a detectable peak at 1001 keV. A comparison of lines between Setup I and Setup II are listed in Table 6.4. The cryostat was evidently the source of upper-chain ^{238}U contaminants, as well as ^{137}Cs.

6.3 High-energy spectrum

With 665 m of overburden (1585 m.w.e.), the muon background rate at WIPP is substantially lower than at sea level[1]. Backgrounds that would be undetectable at sea level become prominent with fewer cosmic events, particularly events at higher energies. Such is the case with the peak at 5.3 MeV. As a rule, processes that deposit events in the high-energy of the spectrum can and will deposit events in the lower-energy spectrum as well (including the $0\nu\beta\beta$ ROI). The question becomes: what constitutes the energy spectrum above 2615 keV? For this work, the terms high- or higher-energy correspond to the energy spectrum in an HPGe detector above 2700 keV. The energy spectrum is shown in Fig. 6.8.

Events that can deposit more than 2700 keV in energy and contribute to the high-energy spectrum include:

- Pileup ($\gamma + \beta$, $\gamma + \gamma$ simultaneously emitted from a decay, or any combination of alpha, beta, or gamma from near-simultaneous decay-chain partners, for example ^{212}Bi$\rightarrow$^{212}Po$\rightarrow$^{208}Pb)

- Cosmic-ray induced events (muons, bremsstrahlung photons)

- Alpha events (3.9 - 8.8 MeV alphas from ^{232}Th and ^{238}U decay chains)

Pileup from betas and gammas is not a likely source for these higher-energy events. Of all the beta decays in the ^{238}U and ^{232}Th decay chains, the largest Q-values come from ^{208}Tl (4999 keV) and ^{214}Bi (3270 keV). The rest are under 2600 keV, and so no single decay can deposit events in the higher-energy spectrum. Both ^{208}Tl and ^{214}Bi emit multiple gammas at once and so multiple gammas from the same decay can interact in the detector. For example, a calibration source of ^{232}Th / ^{208}Tl, situated close to a detector, will result in visible peaks at 3126 keV and 3198 keV. These are the result of pileup between the 2615 keV gamma and either the 511 or 583 keV gamma. Triple pileup at 3709 keV can also be seen if the source is close enough. The size of these pileup peaks is dependent upon the distance

[1] $0.01/\text{cm}^2/\text{s}$ at sea level vs. $3.1 \times 10^{-7}/\text{cm}^2/\text{s}$ at WIPP [2]

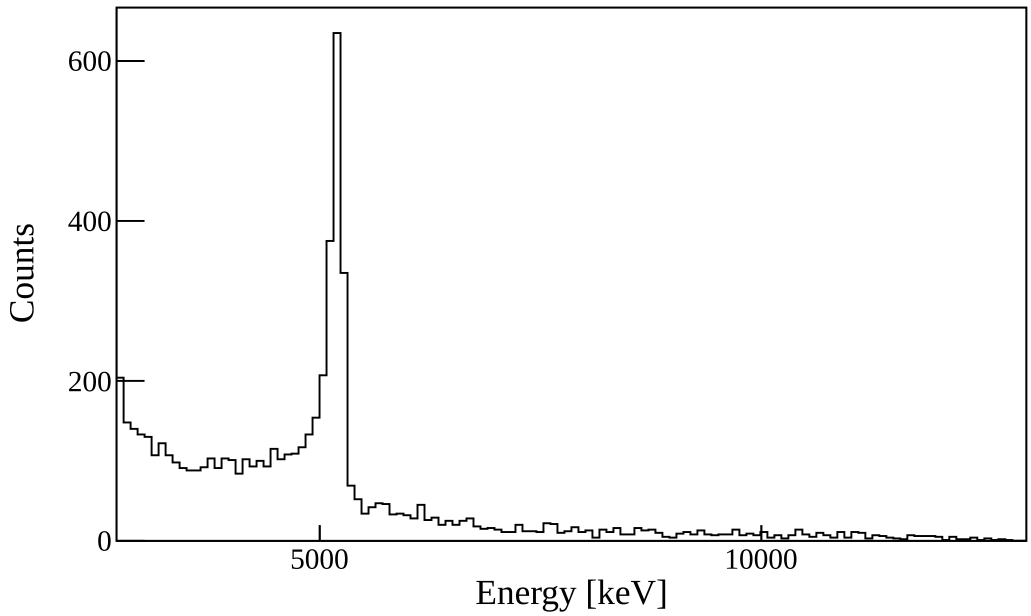

(a) WIPPn high energy, linear plot

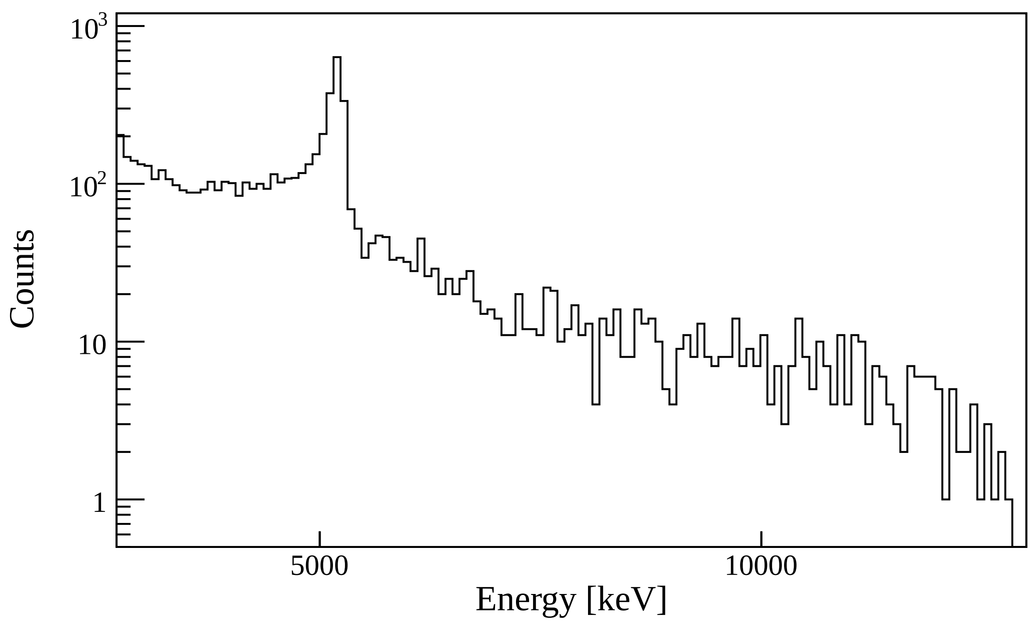

(b) WIPPn high energy, log plot

Figure 6.8: The high-energy spectrum of the WIPPn detector, with 519.78 days of livetime. Only the spectrum above 2700 keV is shown.

of the decay from the detector. No such sum-peaks were found in the WIPPn background data. A simulation was run in MaGe with a ^{232}Th source placed directly adjacent to an HPGe crystal with the dimensions of the WIPPn detector. Ratios of the pileup peaks (3126 and 2198 keV) to the 2615 keV peak were 3.5% and 15.2%, respectively. The ratio of the sum of all counts above 2615 keV to the number of counts in the 2615 keV peak was 1.87. The complete lack of sum-peaks in the WIPPn data implies that the majority of contributions to the 2615 keV peak are not close to the detector. The simulation also showed that the total number of counts above the 2615 keV peak from pileup was less than twice the amount in the 2615 keV peak, placing an upper bound on the rate of higher-energy pileup counts in relation to the number of counts in the 2615 keV peak. Pileup from $\beta - \gamma$ and $\gamma - \gamma$ coincidences can therefore be discounted as a large contributor to the high-energy spectrum of WIPPn.

Pileup from alpha/beta events is not so easily discounted. The lifetime of the alpha decay of ^{212}Po to ^{208}Pb is very short, only 299 ns after the beta decay of ^{212}Bi and on the order of a typical waveform risetime in the WIPPn detector. Because of this, the ^{212}Bi beta and the ^{212}Po alpha can contribute pileup to the energy spectrum. This was seen in section 5.3.2.

6.3.1 Cosmic-induced events: Muon veto

The muon flux underground at WIPP was measured to be 3.1×10^{-7} muons/cm^2/s by Esch et al. [58]. The majority of background counts in the WIPPn detector are attributable to alphas, betas, and gammas from the ^{238}U and ^{232}Th decay chains, but some events originate from cosmic rays. A muon veto panel, originally constructed at the University of Tennessee for use in the MEGA shield, was installed above the WIPPn detector shield. The panel measured 50" by 25" by 1.5" and was encased within a thin aluminum box, constructed to ruggedize the panel for transport and for light-tightness. The panel was installed and tested underground at WIPP over the course of two days, 10-11 December, 2008.

Initial testing of the veto panel took place with an oscilloscope. The aluminum enclosure was found to have numerous light leaks, and close examination of the edges and seams showed definite cracking and flaking. All edges and seams were taped over with dark-black electrical tape. The final light leak was found to occur at the BNC and SHV bulkhead fittings. These provide the outside connections for signal and high-voltage. Due to lack of time, the entire panel was wrapped in a double layer of thick, plastic rubbish bags. This successful, albeit clumsy, method worked; no light leaks were found in further testing with a flashlight and by flicking the room lights on and off.

As explained in Section 4.2.2, the initial implementation of XIA software for veto flags was faulty. A flagged event would have its energy set to zero. This bug was fixed by XIA and the software was reinstalled in January, 2009. Valid veto-flag data were taken between 11 January and 13 February, 2009. Unfortunately, the software version was reset sometime around the 19th or 20th of February. Veto-tagged events in subsequent runs had their energies set to zero. The rest of the data for the veto-tagged events were recorded normally, including the waveform data. The XIA calculates the energy of an event using a digital trapezoidal filter on the ADC values of the pulse. Such a filter, as explained in Section 4.2.2, was used to reconstruct the energies of those lost events.

The veto data taken from December, 2008 through May, 2010, represent 258.23 days of livetime. Out of 981577 events (average of 2.64 counts per minute, 3801 counts per day), there were 1218 events tagged by the Polaris as being in coincident with the veto panel pmt output. This is an average rate of 4.8 ± 0.2 tagged events per day. Figure 6.9(a) displays the vetoed and unvetoed spectra from this period. A parametric fit was performed to the vetoed data for use in energy spectrum fits (Fig. 6.9(b)). The shape function that was found to give a good fit is a sum of an exponential $\exp(-E/p_1)$ and a $1/E$. The contribution of cosmic events to the high-energy background is discussed in the next section.

6.3.2 Alpha Events

The peak at 5.3 MeV, as stated previously, strongly suggests the presence of ^{210}Po decays near the surface of the crystal, which must also imply the presence of ^{210}Pb. Depending on energy loss in the dead layer (or outside of the crystal), an alpha with an initial kinetic energy of 5.3 MeV will deposit between 0 and 5.3 MeV in the detector. The peak structure

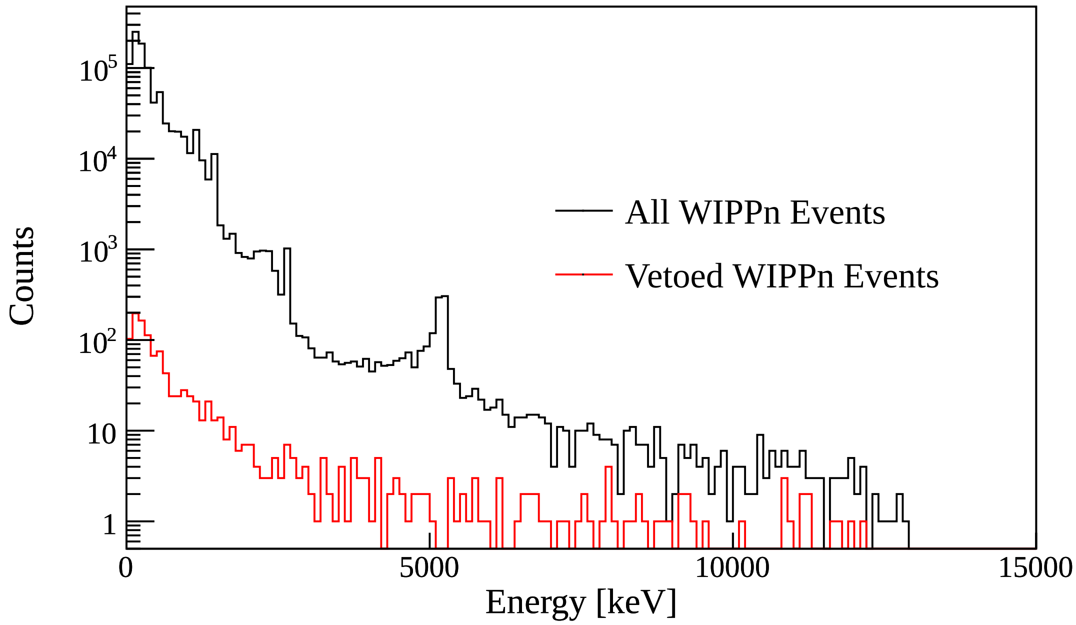

(a)

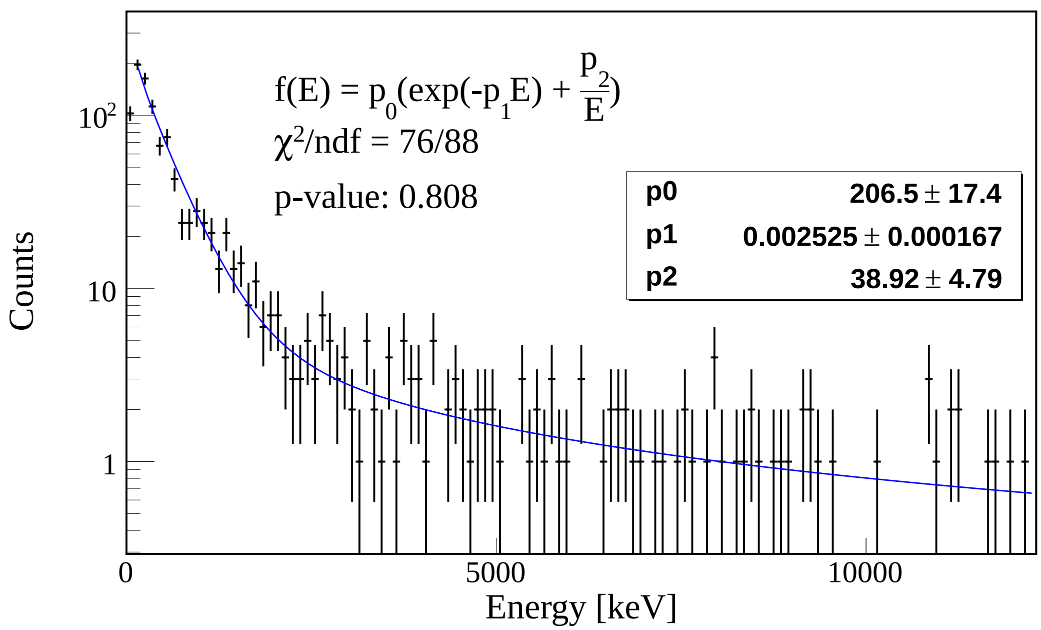

(b)

Figure 6.9: WIPPn events between 12 December, 2008 and May, 2010. The livetime for these runs totals 258.23 days. The black spectrum consists of all events, while those events with a muon-veto tag are plotted in red (a). A parametric fit was performed to the veto data (b).

Table 6.5: Alphas in the ^{238}U and ^{232}Th decay chains. All alphas of intensity $> 0.5\%$ are listed, where the intensity is relative to an initial decay of ^{232}Th . Values of energy, branching ratio, and half-life taken from [40, 42, 43, 44].

(a)

^{232}Th chain			
Isotope	Energy (MeV)	R.I. (%)	Half-life
^{232}Th	4.0123	78.2	1.4×10^{10} y
	3.9471	21.7	
^{228}Th	5.4231	72.7	1.9 y
	5.3404	27.2	
^{224}Ra	5.6854	94.92	3.66 d
	5.4486	5.06	
^{220}Rn	6.2881	99.886	55.6 s
^{216}Po	6.7783	99.998	150 ms
^{212}Bi	6.09	9.75	60.6 m
	6.051	25.13	
^{212}Po	8.7849	64.1	298 ns

(b)

^{238}U chain			
Isotope	Energy (MeV)	R.I. (%)	Half-life
^{238}U	4.151	21	4.47×10^{9} y
	4.198	79	
^{234}U	4.7224	28.42	2.46×10^{5} y
	4.7746	71.38	
^{230}Th	4.6205	23.40	7.54×10^{4} y
	4.6870	76.386	
^{226}Ra	4.601	5.55	1600 y
	4.7843	94.45	
^{222}Rn	5.4895	99.920	3.8235 d
^{218}Po	6.0024	99.979	3.098 m
^{214}Po	7.6868	99.990	164.3 μs
^{210}Po	5.3043	100	138.4 d

at 5.3 MeV implies that the ^{210}Pb is either on the crystal or on an adjacent surface. The continuum below the peak could also contain ^{210}Po events, albeit smeared due to energy loss. This energy loss could be due to ^{210}Pb embedded in some external material (e.g. a solder bead on the crystal). Such an example was actually discovered in data from the IGEX $0\nu\beta\beta$ experiment [33, 61].

Events above the peak are not from ^{210}Po but could conceivably be from other alphas in the ^{232}Th and ^{238}U decay chains (as well as cosmics). All alphas with relative intensities higher than 0.05% in these chains are listed in Table 6.5, and the full decay chains are shown in Fig. 6.10. With initial kinetic energies from 3.9–8.8 MeV, coupled with the possibility of energy loss external to the crystal, these alphas could be responsible for counts both above and below the ^{210}Po peak. It should again be noted that the decay chains are not necessarily in equilibrium, as there are several natural “breaks” or “bottlenecks” in the chains. One example of this is the lower uranium chain at ^{222}Rn. As explained in Section

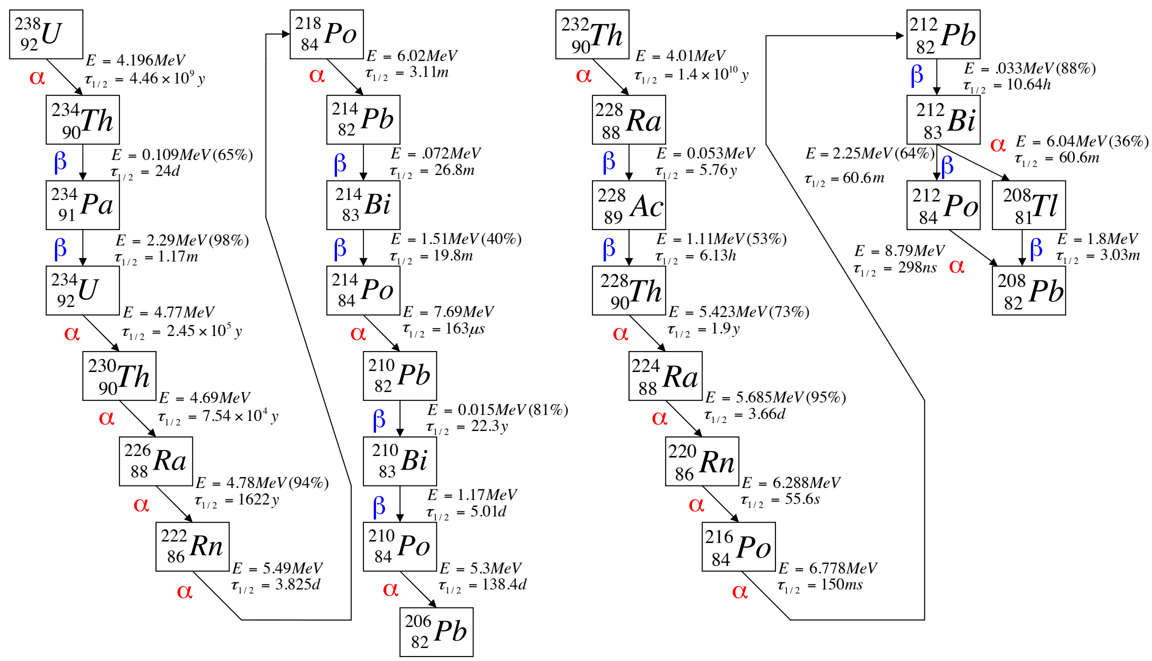

Figure 6.10: The decay chains of ^{238}U and ^{232}Th.

2.2.1, introduction of radon gas and subsequent decays quickly lead to the (relatively) long-lived isotope ^{210}Pb (22 years). This is why it is conceivable that the only alphas in the high-energy spectrum are from ^{210}Po. If counts *are* coming from alphas from nearby ^{238}U or ^{232}Th contamination, then there are several signatures for which to look. The energy spectrum might contain peak information from the alphas, and time-stamp information can be used to look for alpha–alpha and alpha–gamma correlations.

If there is no mechanism for energy loss of the alphas — no external material to travel through before entering the detector — then they should appear as peaks in the energy spectrum, similar to the ^{210}Po peak. The cleanest case for this would be decays within the germanium, leading to peaks in the energy spectrum at the Q-value of the alpha decay. These peaks would be narrow, subject only to the resolution of the detector with no energy straggling contributions. Decays at or adjacent to the crystal surface will be subject to energy loss and straggling in the dead layer, but still produce a peak like that of ^{210}Po. There is no obviously discernible peak structure either above or below the 5.3 MeV peak, implying that the concentration of alpha emitters either in or adjacent to the crystal is small compared with other backgrounds.

Time-Coincidence Analysis

The range of half-lives in the ^{238}U and ^{232}Th decay chains range from 299 ns to 10^{10} years. Because these decays occur with characteristic lifetimes, their timing signatures can be looked for in a data set. Specifically, cascades of alpha decays such as $^{224}\text{Ra}\xrightarrow{\alpha}{}^{220}\text{Rn}\xrightarrow{\alpha}{}^{216}\text{Po}$ occur within short-enough times[2] that analyzing the time stamps of high-energy events can yield information on the amount of uranium and/or thorium contamination near an HPGe crystal. The ^{238}U and ^{232}Th decay chains have several decays with half-lives shorter than a few minutes. These include cascades where either two alphas or an alpha and a gamma are separated by a short time. For example, two events, both depositing energies above 2.7 MeV and separated by less than 111.2 seconds (twice the half-life of ^{220}Rn) might qualify as a signature from $^{224}\text{Ra}\xrightarrow{\alpha}{}^{220}\text{Rn}\xrightarrow{\alpha}{}^{216}\text{Po}$. Similarly, an event depositing 609 keV, followed very shortly by a high-energy event, might signify an alpha from the chain $^{214}\text{Bi}\xrightarrow{\beta/\gamma}{}^{214}\text{Po}\xrightarrow{\alpha}{}^{210}\text{Pb}$.

While WIPPn certainly has a lower background than it would have on the surface, it still has a non-negligible background count rate (on the order of 2-4 counts / minute, depending on shielding and sample counting). There then exists the possibility of an accidental coincidence, where the rate of such an accidental double coincidence is given by $r_d = r_{s1}r_{s2}\Delta t$, with r_d the accidental doubles rate, r_{si} the rate of single events satisfying the i^{th} cut, and Δt the time window cut. This can be compared to the rate of actual alpha events, $r_{2\alpha} = \eta_1\eta_2\eta_t r_\alpha$, where $r_{2\alpha}$ is the expected double-alpha rate, r_α is the absolute rate of such decays, and η_1 and η_2 are the efficiencies to measure the first and second alpha decays. The time window Δt is set at twice the half-life of interest, thus giving a 75% probability of a double occurring within that window. Unless the decays are occurring within the crystal, the highest average efficiency possible would come from decays at the surface. The efficiencies for these alpha decays at the surface to deposit an energy above 2700 keV were calculated via Monte Carlo as in chapter 3. The efficacy of this technique therefore depends on not having r_d larger

[2]the half-life of ^{220}Rn is 55.6 s

than $r_{2\alpha}$, and so requires either very small background rates (small r_s) or only looking for events with small Δt.

The decay cascade $^{224}\mathrm{Ra}\xrightarrow{\alpha}{}^{220}\mathrm{Rn}\xrightarrow{\alpha}{}^{216}\mathrm{Po}\xrightarrow{\alpha}{}^{212}\mathrm{Pb}$ involves three alpha decays in rapid succession, with characteristic half-lives of 55.6 s and 150 ms. This portion of the ^{232}Th decay chain then provides the opportunity to look for triple coincidences. The corresponding accidental triple-coincidence rate would be $r_t = r_{s1}r_{s2}r_{s3}\Delta t_{12}\Delta t_{23}$, with Δt_{12} and Δt_{23} the time windows used between the second and third decays.

A Tree Analysis Module (Sec. 4.3.1) was developed for use in timing-correlation analyses. The module is initialized with cuts in energy and time. The module loops over events in a `TTree`, looking for an event that satisfies the first energy cut. It records the energy and time stamp of that event and then steps forward, event-by-event until the time window (twice the half-life of interest) is surpassed. Any event that falls within the time window (and also satisfies an optional energy cut) is recorded also. The number of events satisfying the cuts is output, and a second `TTree` with the distilled events is written where it can be analyzed further.

The data used for this test represents the WIPPn event-mode data from November, 2007 through May, 2010. This corresponds to after the XIA Polaris software was altered to fix the time stamp problem (Section 4.2.2). The livetime for this data set, as calculated via the prescription in Section 4.2.3, was found to be 535.39 days. Five separate analyses were run, utilizing the cuts found in Table 6.7. The lower energy cuts for alpha events was placed at 2700 keV to limit an extreme rise in accidentals due to the much larger event rate below this energy. Analyses AI-AIII look for alpha-alpha doubles, while BI looks for coincidences between a higher-energy alpha and any signature from ^{214}Bi (beta, gamma, or the combination). A triples analysis (analysis T1) was also performed, looking at events that satisfy both AI and AII. The values of Δt that were used to look for coincidences were set at twice the half-life of the decay, corresponding to an expected 75% efficiency to measure a coincidence corresponding to that half-life.

Results for the analyses are shown in Table 6.7. The number of counts for each analysis is listed along with the expected number of accidentals. It should be noted that time windows of 111.2 and 373.2 seconds are quite long for a detector with this event rate, as evidenced

Table 6.6: Energy and time window cuts used for time-correlation analysis of high-energy data with the WIPPn detector.

		Doubles		
	Energy Cut 1 (keV)	Energy Cut 2 (keV)	Time Window	Decay Scheme
		$\alpha - \alpha$		
AI	$2700 - 5690$	$2700 - 6290$	111.2 s	$^{224}\text{Ra}\xrightarrow{\alpha}{}^{220}\text{Rn}\xrightarrow{\alpha}{}^{216}\text{Po}$
AII	$2700 - 6290$	$2700 - 6780$	0.3 s	$^{220}\text{Rn}\xrightarrow{\alpha}{}^{216}\text{Po}\xrightarrow{\alpha}{}^{212}\text{Pb}$
AIII	$2700 - 5500$	$2700 - 6000$	373.2 s	$^{222}\text{Rn}\xrightarrow{\alpha}{}^{218}\text{Po}\xrightarrow{\alpha}{}^{214}\text{Pb}$
		$\alpha - \gamma/\alpha - \beta$		
BI	$0 - 3270$	$2700 - 7690$	328.6 μs	$^{214}\text{Bi}\xrightarrow{\beta/\gamma}{}^{214}\text{Po}\xrightarrow{\alpha}{}^{210}\text{Pb}$
		Triple		
TI	Satisfying	AI & AII		$^{224}\text{Ra}\xrightarrow{\alpha}{}^{220}\text{Rn}\xrightarrow{\alpha}{}^{216}\text{Po}\xrightarrow{\alpha}{}^{212}\text{Pb}$

by the high numbers of expected accidentals. The Majorana Demonstrator, with a far lower event rate, will be able to utilize these time windows to greater effect.

The two long-time analyses (111.2 s and 373.2 s) resulted in a slight excess of measured doubles above expected accidentals (8.4 and 14.5, respectively). These two analyses have very similar cuts, making it likely that an event that satisfies one cut will also satisfy the other. This is indeed the case, with 63 out of the 72 111.2 s double candidates also qualifying as 373.2 s doubles. This makes it difficult to assess the origin of alphas using this technique.

In contrast, the two short-time analyses (0.3 s and 328.6 μs) are well-separated in time with almost negligible expected accidentals. Figure 6.11 shows the energy spectra for the doubles candidates from the two analyses. The first and second events in the 0.3 s doubles analysis fall into peaks just below 6300 and 6800 keV, respectively. The spread of energies (around 100 keV) is similar to the width of the large peak at 5.3 MeV. Because the rate of accidentals is so small (only 0.18 expected accidentals), and because the peaks occur near the alpha energies of ^{220}Rn and ^{216}Po, these are very likely double-alpha events from the ^{232}Th decay chain, arising from surface contamination. Similarly, the 328.6 μs analysis shows a definite peak just below 7700 keV, the energy of the ^{214}Po alpha. There are also four

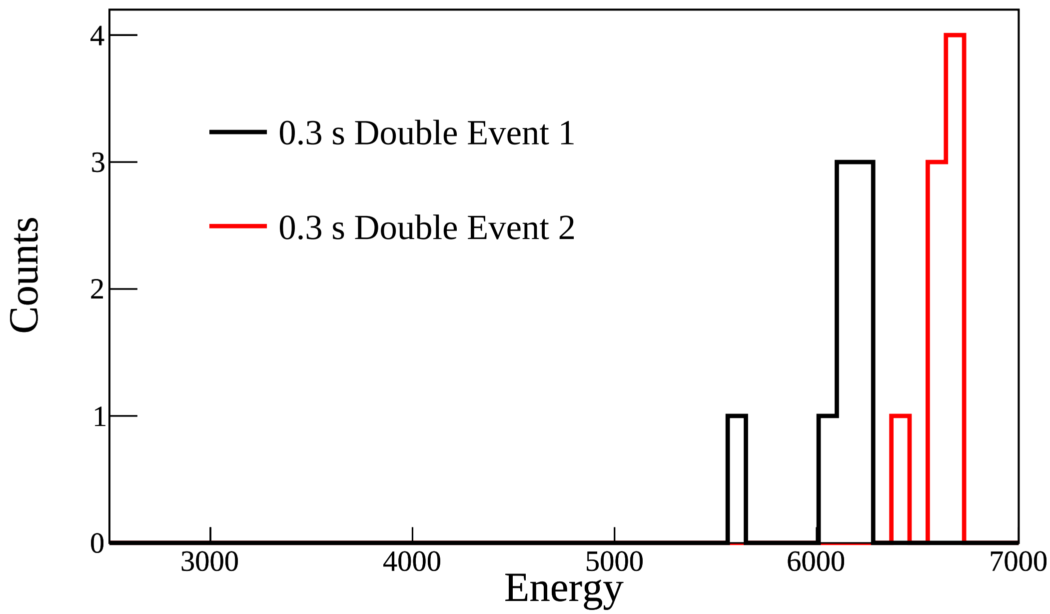

(a) 0.3 s double events (AII)

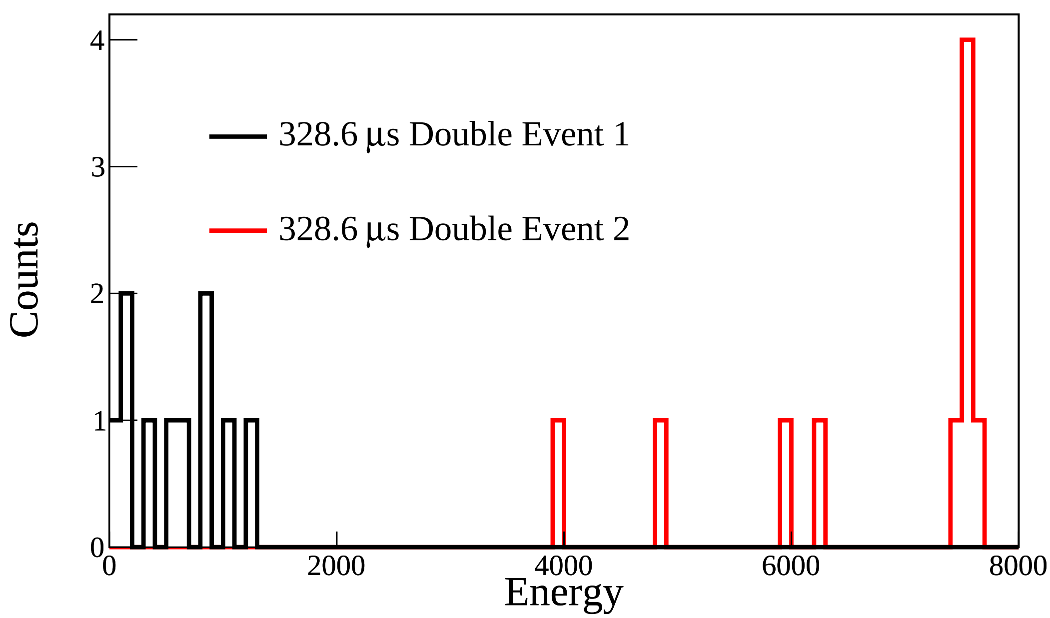

(b) 328.6 μs double events (BI)

Figure 6.11: Coincident events from the short double time correlation analyses.

Table 6.7: Results from the time-correlation analysis studies. The difference between expected accidentals and candidates are tabulated for each analysis, as well as the coresponding count rate. The livetime of the data used in these analyses was 535.39 days.

	Candidates Found	Expected Accidentals	Difference	Counts / Day
AI	72	63.61 ± 1.8	8.39	0.027
AII	8	$(1.85 \pm 0.05) \times 10^{-1}$	7.81	0.015
AIII	219	204.5 ± 5.8	14.53	0.027
BI	10	$(8.8 \pm 0.1) \times 10^{-2}$	9.91	0.019
TI	1	$(2.24 \pm 0.09) \times 10^{-3}$	0.998	0.0002

candidate double events at lower energies. These lower-energy events might be construed as either surface events at large incidence angles (the alpha travels through a significant portion of the dead region) or else they might originate in the bulk of some external material.

The two short-doubles analyses can be used to calculate the surface activity on the WIPPn detector. The true alpha rate is related to the measured rate as explained above as $r_\alpha = \frac{4}{3}\frac{r_{2\alpha}}{\eta_1\eta_2}$. The differences obtained in Table 6.7, combined with the efficiencies η_1 and η_2 as determined from simulation (assuming a surface contamination), give rates of $(8.1 \pm 3.0) \times 10^{-2}$ decays per day of $^{220}\mathrm{Rn} \xrightarrow{\alpha} {}^{216}\mathrm{Po} \xrightarrow{\alpha} {}^{212}\mathrm{Pb}$. Assuming that the ^{232}Th decay chain is in equilibrium, this number equates to the number of initial ^{232}Th decays at the surface of the crystal. The ^{232}Th chain has six alphas, yielding an overall alpha decay rate on the surface of the WIPPn detector from ^{232}Th of 0.49 ± 0.18 alpha decays per day. A similar treatment for the 328.6 μs analysis yields $(5.7 \pm 1.8) \times 10^{-2}$ decays of $^{214}\mathrm{Bi} \xrightarrow{\beta/\gamma} {}^{214}\mathrm{Po} \xrightarrow{\alpha} {}^{210}\mathrm{Pb}$ per day. The assumption of chain equilibrium in the ^{238}U chain is not valid, making it difficult to convert this rate to a total alpha decay rate. The doubles in this analysis were spread out in time over the 535 days of livetime, implying that they are supported by ^{226}Ra (the half-lives of the daughters of ^{226}Ra range from μs to days, until ^{210}Pb is reached). These are also surface events, and so it is possible that the ^{226}Ra source is not directly adjacent to the crystal, but instead the decay to ^{222}Rn (a noble gas) is allowing migration of the contamination. If this were the case, then the only ^{238}U chain alphas that are contributing are from ^{222}Rn, ^{218}Po and ^{214}Po. The alphas from ^{210}Po are treated separately in the next section.

Energy-Spectrum Fits

The timing-correlation analysis, while useful for measuring the surface-alpha activity, fails at measuring external-bulk alphas. This is due to the very small efficiency of measuring two subsequent alphas originating away from the crystal. To measure bulk contamination, the energy spectrum itself can be used. Simulations of bulk-alpha decays — specifically the ^{232}Th and portions of the ^{238}U decay chains — were simulated using MaGe, as explained in Chapter 3. The resultant energy spectra were turned into probability density functions for use in fitting. In this manner, such pdfs for the ^{232}Th and ^{222}Ra decay chains were created, as well as a pdf for the 5.3 MeV alpha from ^{210}Po. Another pdf was created to account for the cosmic background, using the curve from Fig. 6.9(b). All of these pdfs were combined into a single model pdf for use in an extended maximum-likelihood fit. Only data taken with the shield in its copper-lead configuration were used (September 2008 - May 2010), due to the different background count rates. The composite pdf then looks like

$$N_{total} = N_{PS} + N_{PB} + N_{TS} + N_{TB} + N_{RS} + N_{RB} + N_{cosmic} \tag{6.1}$$

$$\begin{aligned} N_{total} f_{total}(E, p_0, p_1, \dots) = {} & N_{\mathrm{PS}} f_{\mathrm{PS}}(E) + N_{\mathrm{PB}} f_{\mathrm{PB}}(E) \\ & + N_{\mathrm{TS}} f_{\mathrm{TS}}(E) + N_{\mathrm{TB}} f_{\mathrm{TB}}(E) \\ & + N_{\mathrm{RS}} f_{\mathrm{RS}}(E) + N_{\mathrm{RB}} f_{\mathrm{RB}}(E) \\ & + N_{\mathrm{cosmic}} f_{\mathrm{cosmic}}(E, p_0, p_1) \end{aligned} \tag{6.2}$$

where N_{xy} stands for the number of counts assigned to the pdf f_{xy}, and P, T, and R in the first subscript stand for ^{210}Po, ^{232}Th, and ^{222}Ra, and the S and B in the second subscript stand for "surface" and "bulk". The fit was performed using `MINUIT`'s `MIGRAD` (for function minimization) and `MINOS` (for asymmetric-error calculation). The fit showed that contributions from surface ^{232}Th and ^{226}Ra were consistent with zero, as was the contribution

Table 6.8: Numbers and rates of individual components of composite alpha model, fitted to WIPPn high-energy data. The data set represents 317.27 days of livetime. An extended maximum-likelihood fit was performed using `MINUIT`, with likelihood minimization performed by the `MIGRAD` algorithm and asymmetric errors calculated using the `MINOS` algorithm within `MINUIT`.

Contribution	Number	Counts / Day
Cosmic BG	1033^{+62}_{-59}	$3.33^{+0.21}_{-0.19}$
Surface ^{210}Po	907^{+37}_{-36}	$2.98^{+0.12}_{-0.12}$
Bulk ^{210}Po	641^{+75}_{-76}	$1.89^{+0.31}_{-0.31}$
Bulk ^{232}Th	1019^{+93}_{-90}	$3.27^{+0.61}_{-0.60}$

from bulk ^{226}Ra. The likelihood minimization was then re-run, but without the surface ^{232}Th and ^{226}Ra and bulk ^{226}Ra. This resulted in a better p-value (0.47 vs. 0.42). The composite model fit is shown in Fig. 6.12(a), with the residuals shown in Fig. 6.12(b). The number of events for each component of the model, extracted from the fit and converted to daily rate, are shown in Table 6.8.

6.3.3 Comparison of Timing-Coincidence and Energy-Spectrum Analyses

The timing-coincidence analysis found alpha rates of (0.49 ± 0.18) alpha decays per day from ^{232}Th and $(5.7 \pm 1.8) \times 10^{-2}$ alpha decays per day of ^{214}Bi/^{214}Po. The energy-spectrum fits gave ^{232}Th alpha rates of $3.27^{+0.61}_{-0.60}$ counts per day, while those from ^{238}U were consistent with zero. It is important to point out that the numbers from the energy decay represent *measured* counts per day, while those from the timing-coincidence analysis have had a measurement efficiency (derived in Section 3.2.2) applied and represent actual alpha decays. Without more information about the bulk contamination, it is futile to calculate an efficiency for any given external-bulk decay to make it to the HPGe detector. In particular, a decay embedded deep inside an external-bulk material has less of a chance to register with the detector than does a surface event. The probability of witnessing a double event is made that much harder, as it is the product of the efficiencies for measuring each individual alpha. This means that the timing-coincidence analysis is more sensitive to surface events (at least

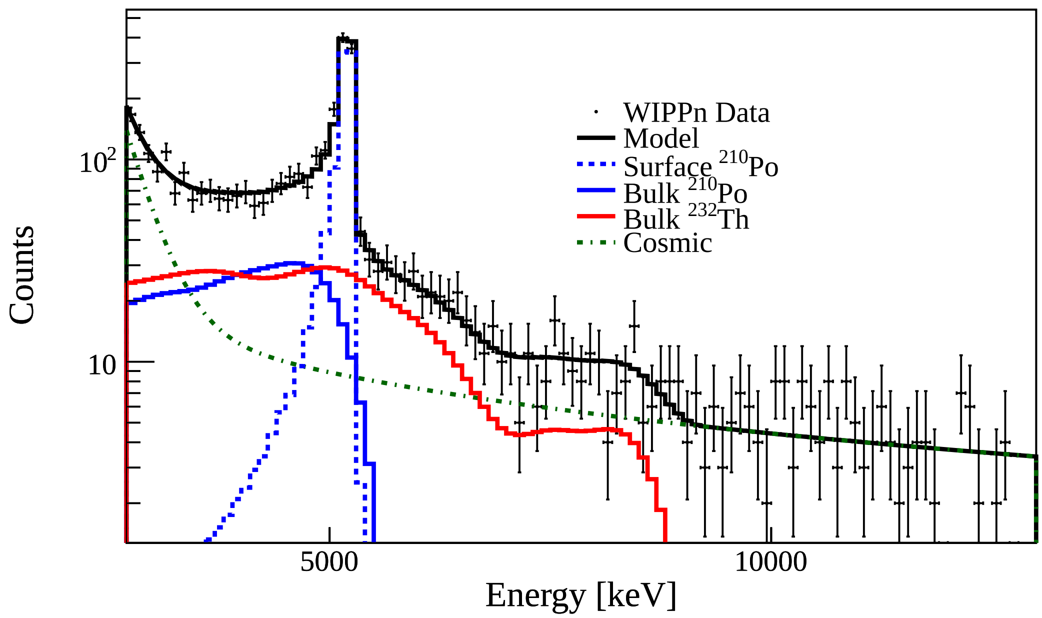

(a) WIPPn high-energy data fit with alpha model.

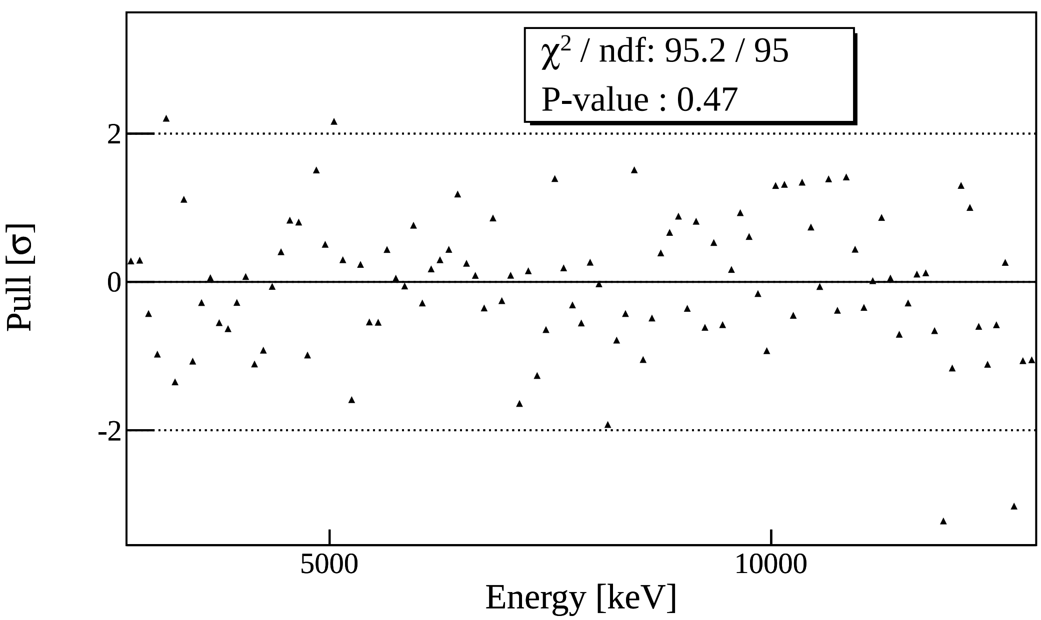

(b) Residual pulls of the fit.

Figure 6.12: Fit of high-energy WIPPn data to a composite-alpha model.

for the timing signatures in Table 6.6), while the energy-spectrum analysis is more sensitive to bulk events. The surface events from ^{210}Po do not have a useful timing signature, but the rate is high and so they show up in the energy-spectrum analysis.

6.3.4 Further High-Energy Background Reduction

Table 6.8 lists the high-energy background rates, as measured using an energy-spectrum analysis. These background rates could conceivably be improved, using some modest and not-so-modest efforts.

The cosmic background is in principle completely removeable. As noted in Sec. 4.2.2, the veto has not yet been optimized. In particular, a careful study of veto efficiency has not been performed. A fully operational cosmic veto, either using the existing veto panel or another, is a completely feasible upgrade to the current WIPPn setup.

The alpha backgrounds are another matter completely. The surface-type and bulk-type backgrounds must be coming from very close to the surface, but it isn't clear exactly where. The WIPPn detector is a non-segmented N-type HPGe detector, and so there is zero information about position information from surface events. Furthermore, HPGe detectors (specifically N-types) are quite fragile with respect to handling the surfaces. The benefits of "surgery" must be weighed against the possible cost of losing the detector.

6.4 Conclusions

The WIPPn detector has provided a chance for some interesting detective work in tracking down backgrounds, in addition to its primary role as a low-background counting facility. The high-energy spectrum, defined here as counts above 2700 keV, is a mixture of alphas and cosmic-related events. This spectrum was decomposed into a composite of cosmic events and bulk- and surface-alpha events using energy-spectrum fits and a timing-correlation analysis. The timing-correlation analysis measured the surface-event rate for ^{232}Th and lower-chain ^{238}U alphas, whereas the energy-spectrum analysis measured the bulk-event rates. A discrepency among ^{232}Th rates between the energy and timing analysis ($3.27^{+0.61}_{-0.60}$ counts / day vs. 0.49 ± 0.18 counts / day).

Chapter 7

EXPERIMENTAL IMPLICATIONS AND CONCLUSIONS

Next-generation experiments searching for rare-physics events — events such as $0\nu\beta\beta$ — need impressive background reduction techniques; any background that can mimic or mask the signal from $0\nu\beta\beta$ needs to be understood and mitigated as completely as possible. This work has attempted to explain the backgrounds from alpha decays on HPGe detectors (Chapter 2), develop predictive models for the effect alpha backgrounds will have on those detectors (using simulation in Chapter 3 and an analytic model in Chapter 5), and test those models with available data (Chapters 5 and 6). The time has come to apply those models to current and future experiments searching for the decay $^{76}\text{Ge}\rightarrow^{76}\text{Se} + 2e^{-}$.

7.1 Alpha-Background Efficiencies

The efficiency for a surface alpha, e.g. the alpha from ^{210}Po, to populate the region-of-interest in a double-beta decay experiment using HPGe detectors was calculated from simulations in Chapter 3. For a nominal dead layer value of 0.3 μm, the efficiency for a surface decay from ^{210}Pb is $(1.21 \pm 0.05) \times 10^{-5}$, as calculated via a MaGe simulation. Assuming a possible variation in dead-layer of ± 0.01 μm adds a systematic uncertainty of ± 0.04. This includes the corrective convolution that was required in Section 5.2.3, although the difference in calculated efficiency with and without the convolution was only 0.01×10^{-5}. The final, simulated efficiency is then $(1.21 \pm 0.05_{\text{stat}} \pm 0.04_{\text{sys}}) \times 10^{-5}$.

The same efficiency was also calculated using the analytic model constructed in Section 5.2.2. The model was used to generate an energy spectrum from surface ^{210}Po decays, and the efficiency for a decay to land in the 4 keV-wide ROI is calculated to be $(1.467 \pm 0.004) \times 10^{-5}$. Allowing for the same ± 0.01 μm variation in dead layer, the model efficiency becomes $(1.47 \pm 0.004_{\text{stat}}{}^{+0.04}_{-0.03}{}_{\text{sys}}) \times 10^{-5}$.

The two techniques differ by 0.26×10^{-5}. The SANTA test-stand data was in better agreement with the analytic model — particularly the bulk comparison — and so this value is used as the final calculated efficiency. It also represents the more conservative value. The discrepency between simulation and model is added as a systematic lower error.

There is another possible systematic effect arising from uncertainty in the dead-layer profile (Appendix A.3). Both the simulation and the analytic model assume a step-like efficiency function for the dead layer. In this case, no charge collection happens at all within the dead region, but charge collection is 100% efficient within the active region. The stopping power, $\frac{dE}{dX}$, is a non-linear function of alpha energy, and so the amount of energy lost in a dead region is dependent upon both energy of the alpha and the charge-collection efficiency within that region. A smoothly-varying dead-layer profile will result in less charge being collected than a step-like profile. Appendix A.3 derives this effect for an example profile that represents the largest possible difference in the energy spectrum. When this correction is added to the simulated and model energy spectra, the efficiency for a decay of ^{210}Po to land in the ROI increases by 7%. This makes physically intuitive sense, as the dead-layer difference results in more energy being lost to the dead region (Fig. A.4), thus pushing events at higher-incidence angles to lower-energy portions of the spectrum (Fig. 7.1). It is worth pointing out that the difference in energy spectrum is highly dependent on incidence angle (Fig. A.4) and is only appreciable ($\Delta E > 1$ keV) for incidence angles higher than $\sim 70°$, and so the SANTA test stand data cannot shed any light on the shape of the profile. A related effect would come from non-uniformity in the dead layer over the surface of a detector. If the dead layer varies from point to point on the detector, then the efficiency for an alpha decay would vary from point to point as well. Table 3.1 tabulates the efficiency for various dead-layer thicknesses, and these efficiencies vary linearly with dead layer. Therefore, non-uniformity in the dead layer can be treated using an average, effective dead layer thickness.

Accounting for the different predictions of the simulation vs. the analytic model, and folding in the possibility of a dead-layer effect, the value for the efficiency of a ^{210}Po alpha, emitted from the p^{+} (thin) surface of an HPGe detector, is $(1.47^{+0.10}_{-0.20} \times 10^{-5})$.

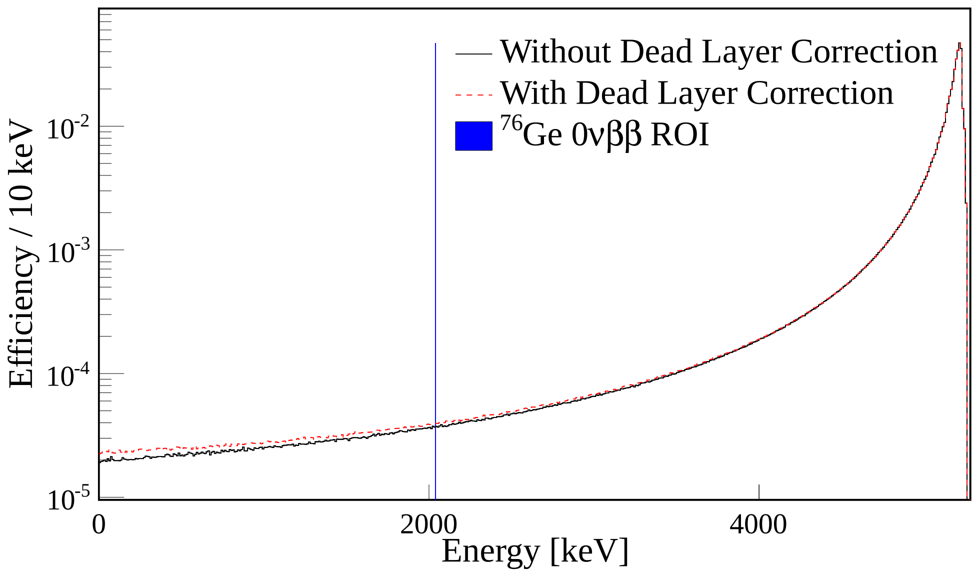

(a)

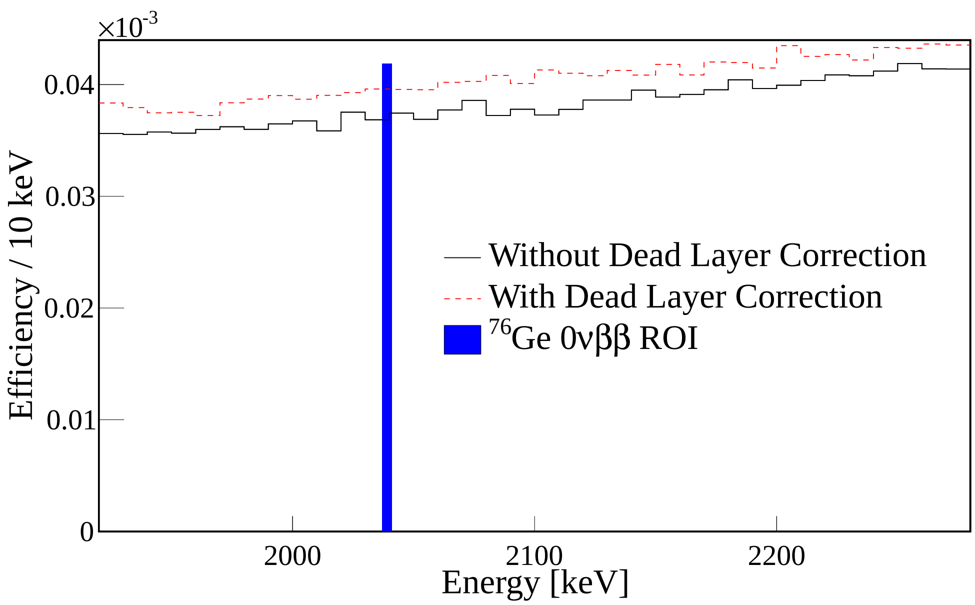

(b)

Figure 7.1: The dead-layer profile (as a function of depth) affects the energy spectrum for surface alphas emitted from ^{210}Po (5.3 MeV). The solid, black energy spectrum is from the analytic model with a step-like dead-layer profile. The red, dashed line assumes a linear profile (Appendix A.3). This profile represents the greatest difference in energy spectra, and the resultant change in efficiency for a surface-alpha background hit is 7%.

7.2 Contamination Limits for HPGe Detectors in $0\nu\beta\beta$ Experiments

The next step applies the efficiency of a surface-alpha decay on a p^+ surface to the actual HPGe detector. Section 2.1.2 discussed the different types of HPGe detectors with respect to their surfaces and susceptibility to alpha decays. Using the susceptibilities calculated there, we can calculate alpha-background rates.

7.2.1 Limits for the MAJORANA DEMONSTRATOR

The goals of the MAJORANA DEMONSTRATOR, as explained in Chapter 1.4, will be to test the $0\nu\beta\beta$ claim by Klapdor et al. [25] and to demonstrate the background goals necessary for a future tonne-scale experiment. The MAJORANA DEMONSTRATOR will comprise 40 kg of HPGe detectors (at least half of which will be enriched to 86% ^{76}Ge, and the rest composed of natural germanium (7% ^{76}Ge). With this in mind, we need to adjust our definition of "background counts in the ROI per tonne-year of exposure". Alpha backgrounds, both surface and external-bulk, are independent of the isotopic makeup of the detector. Therefore, it makes the most sense to express alpha-background rates in terms of "counts in the ROI per tonne-year of germanium". This can then be scaled to the actual percentage of ^{76}Ge within an experiment.

The background rate of a detector (or array of detectors), in units of background counts within the $0\nu\beta\beta$ ROI per tonne-year, is given as

$$R_\alpha = \frac{k}{M}\int_S \mathcal{A}(\vec{r})\varepsilon(\vec{r})\Omega(\vec{r})dS, \tag{7.1}$$

with M the active detector mass, k the coefficient to convert to counts of background per tonne-year in the ROI ($3.35 \times 10^7 s/y$), $\mathcal{A}$ the surface-alpha activity (i.e. in Bq/cm^2), and $\varepsilon(\vec{r})$ the efficiency for a decay at position $\vec{r}$ to count as a background. The integral is over all relevant surfaces dS, and $\Omega(\vec{r})$ is the solid angle of p^+ area with which the area element dS has direct line-of-sight. This can be significantly simplified for decays that occur on the surface of the detector itself:

$$R_\alpha = k\frac{\mathcal{S}}{M}\mathcal{A}_{avg}\varepsilon = k\lambda\mathcal{A}_{avg}\varepsilon \tag{7.2}$$

with $\mathcal{S}$ the total susceptible surface area, $\mathcal{A}_{avg}$ the average surface-activity rate, and ε the efficiency calculated in the previous section (a true "surface" event with solid angle $\Omega = 2\pi$). The factor λ, introduced in Section 2.1.2, is the ratio of susceptible surface area to active mass (with units of area/mass). Because the DEMONSTRATOR will be composed of P-type Point Contact (P-PC) detectors, it will have a particularly-low susceptibility to alpha backgrounds, especially in comparison to N-type detectors (Table 2.1). This is due to the vast majority of surface area that is n^+, or "thick". The susceptibility for the P-PC detectors used in the DEMONSTRATOR is 0.34±0.03 kg/cm^2, where the uncertainty comes from the quoted tolerances of the detector dimensions for the Canberra BEGe detectors that will compose the first module of the MAJORANA DEMONSTRATOR. For comparison, the susceptibility for a typical N-type detector such as SANTA is over 400 times greater. Plugging in the susceptibility and the calculated efficiency, the rate then becomes

$$\begin{aligned} R_\alpha &= (3.15\times 10^7\ \mathrm{s/y})\left(1000\ \frac{\mathrm{kg}}{\mathrm{tonne}}\right)(0.34\pm 0.03\ \mathrm{kg/cm^2})(1.47^{+0.10}_{-0.11}\times 10^{-5})\mathcal{A}_{avg} \\ &= 1.57^{+0.16}_{-0.17}\times 10^5\mathcal{A}_{avg}, \qquad \mathcal{A}_{avg}\ \text{in Bq/cm}^2 \\ &= 1.82^{+0.20}_{-0.21}\mathcal{A}_{avg} \qquad \mathcal{A}_{avg}\ \text{in Decays/Day/cm}^2 \end{aligned} \tag{7.3}$$

Table 7.1 displays expected background rates from ^{210}Po alphas for several values of surface activity $\mathcal{A}_{avg}$. The alpha rate from the Sudbury Neutrino Observatory's Neutral Current Detectors represents the cleanest surface ever measured in terms of alpha contamination. Also shown are the rates for a typical N-type detector, given the same activity rates.

If the alpha decays are not coming from the surface of the HPGe crystal, then the solid angle simplification no longer applies. For configurations involving complicated surfaces facing the p^+ area of a detector, the integral in Eq. 7.1 can be calculated using Monte Carlo. An upper limit on the activity can also be placed, assuming an the p^+ region of the crystal has a line-of-sight view of a contaminated surface with average surface activity

Table 7.1: Background count rates from surface alphas for P-PC detectors as will be used in the MAJORANA DEMONSTRATOR, and for typical N-type detectors. These rates are based upon assuming various surface concentration levels. The Borexino clean room was a class-100 clean room built for radon-deposition testing [34], and surface-activity values in the table represent the radon-deposited activity on nylon in that clean room. The WIPPn calculation was performed in Chapter 6, and the SNO NCD calculation is found in [35].

Source	Surface Activity [Bq/cm^2]	Background Rate [Counts in ROI / tonne-year]	
		P-PC	N-type
Borexino Test Clean Room	1.0×10^{-6}	0.16	70
WIPPn Detector	9.0×10^{-7}	0.14	61
MJ BG Model Upper Limit	5.0×10^{-7}	0.08	35
SNO NCD Surface	5.0×10^{-9}	0.0008	0.35

$\mathcal{A}_{avg,ext}$. The limit is then

$$R_{\alpha,ext} \geq k\lambda\mathcal{A}_{ext,avg}\varepsilon \tag{7.4}$$

where the equality holds if all of the solid angle that the sensitive area "sees" is emitting alphas at the surface rate $\mathcal{A}_{ext,avg}$ (and Eq. 7.2 is the limiting case for this). Equation 7.4 holds via a simple flux argument.

Beyond the DEMONSTRATOR

The susceptible surface of a P-PC detector, located right at the point contact, only has a direct line-of-sight with the detector mount. Alphas can only pose a background if they originate from surface plate-out (on the surface of the detector or the detector mount) or from the bulk material of the detector mount. Because of this compartmentalization, the rate of alpha backgrounds (in counts per tonne-year) should be the same for one detector as for one hundred, or one thousand (everything else being equal). The rate formula for P-PCs (Eq. 7.3) would still be valid, then, for a one-tonne scale experiment made up of P-PC detectors with the same susceptibility factor λ. It is worth mentioning here that while P-PC detectors look extremely promising, they are only beginning to be tested in the $0\nu\beta\beta$ arena.

That being said, the usage of P-PC detectors is extremely beneficial to MAJORANA from a surface-alpha standpoint (to say nothing of their other important qualities). As Table 7.1 notes, the disparity in surface-alpha background rates between P-PC detectors and N-types is large. The calculated rates for N-types do not include possible analysis cuts from pulse-shape discrimination, although the surface cut required to veto such events will requires a significant loss of fiducial volume (2 mm from the surface, or a $\sim 10\%$ fiducial volume cut, [62]). Without these cuts, Table 7.1 makes it clear that N-type detectors are unsuitable for $0\nu\beta\beta$ experiments without heroic measures to keep the surface activity down.

7.2.2 Bulk Alphas and $0\nu\beta\beta$ Experiments

Alphas originating in external-bulk materials present an added dimension of difficulty in predicting background rates. Both the activity rate — in Bq/kg — and the surface area of the bulk that is exposed to the detector affect the number of alphas that will hit the susceptible surface of an HPGe detector. It is also important to note that while the background from alphas is sensitive to the amount of exposed surface, the gamma background is not. Simulations have shown that a source of ^{232}Th or ^{238}U in a bulk material, will pose a far-larger background from ^{208}Tl or ^{214}Bi gammas and betas. As an example, the simulated energy spectrum from ^{232}Th within a thorium wire, adjacent to the SANTA detector, contained more counts from betas and gammas in the ROI than alphas. This holds true even for pure-surface contamination, although to a lesser degree. As an example, there is the possibility that the act of machining a "clean" bulk material (one that would face the p^+ area of an HPGe crystal) would introduce contamination. This embedded contamination is essentially confined to the surface of the object. Even in this scenario, the background in the ROI from the betas and gammas is 4-5 times larger than the background from alphas (depending on the size of the HPGe detector). While it is not useful to make predictions of bulk-alpha contamination rates, it was shown (Chapters 5 and 6) that analysis of the higher-energy spectrum can give information about bulk-alpha contamination. These backgrounds can then be used to predict the bulk-alpha background contribution to the ROI.

7.3 The Last Word

Like anything worth pursuing, the search for $0\nu\beta\beta$ is fraught with difficulties. The background levels required for the Majorana Demonstrator and future tonne-scale experiments would have been unthinkable even 20 years ago. The impressive strides in background reduction in the past few decades have enabled the half-life limits for $0\nu\beta\beta$, particularly in ^{76}Ge, to be pushed higher and higher. I am confident that this trend will continue as GERDA and the Majorana Demonstrator come on-line in the next few years.

The advent of using P-PC detectors in $0\nu\beta\beta$ experiments has generated much excitement in the ^{76}Ge $0\nu\beta\beta$ community. They are far-less complicated than highly-segmented N-type detectors, requiring fewer channels and fewer small parts, while providing similar background discrimination. Comparing the background rates in Table 7.1 for P-PC vs. N-type detectors, they also provide a much-higher immunity against alpha backgrounds.

The past 10 years has brought about an era of precision-neutrino experiments, and with it the excitement of discovery. May the next 10 years continue this trend, and so on, *ad infinitum.*

BIBLIOGRAPHY

[1] C. Amsler *et al.*, "The Review of Particle Physics," *Physics Letters B*, vol. 667, p. 1, 2008.

[2] E.-I. Esch, *Detector Development for Dark Matter Research.* PhD thesis, Justus-Liebig-Universität Giessen, 2001.

[3] W. Pauli, 1930. Letter to attendees at a physics conference in Tübingen.

[4] E. Fermi, "An attempt of a theory of beta radiation," *Zeitschrift für Physik A*, vol. 88, pp. 161–177, 1934.

[5] C. Cowan, F. Reines, F. Harrison, H. Kruse, and A. McGuire, "Detection of the free neutrino: a confirmation," *Science*, no. 3212, pp. 103–104, 1956.

[6] B. Kayser, F. Gibrat-Debu, and F. Perrier, *The physics of massive neutrinos*, vol. 25. World Sci. Lect. Notes Phys., 1989.

[7] F. Boehm and P. Vogel, *Physics of massive neutrinos.* Cambridge University Press, 1992.

[8] S. Fakuda *et al.*, "Constraints on neutrino oscillations using 1258 days of super-kamiokande solar neutrino data," *Phys. Rev. Lett.*, vol. 86, p. 5651, 2001.

[9] S. N. Ahmed *et al.*, "Measurement of the total active b-8 solar neutrino flux at the sudbury neutrino observatory with enhanced neutral current sensitivity," *Phys. Rev. Lett.*, vol. 92, p. 181301, 2004.

[10] T. Araki *et al.*, "Measurement of neutrino oscillation with kamland: Evidence of spectral distortion," *Phys. Rev. Lett.*, vol. 94, p. 081801, 2005.

[11] P. Adamson *et al.*, "Measurement of Neutrino Oscillations with the MINOS Detectors in the NuMI Beam," *Phys. Rev. Lett.*, vol. 101, p. 131802, 2008.

[12] L. Wolfenstin, "Neutrino oscillations in matter," *Phys. Rev. D.*, vol. 17, pp. 2369–2374, 1978.

[13] S. Mikheyev and A. Smirnov, "Resonant amplification of ν oscillations in matter and solar-neutrino spectroscopy," *Nuovo Cimento*, vol. 9C, p. 17, 1986.

[14] C. Kraus *et al.*, "Final Results from Phase II of the Mainz Neutrino Mass Search in Tritium β decay," *Eur. Phys. J. C.*, vol. 40, pp. 447–468, Apr 2005.

[15] W. C. Haxton and G. J. Stephenson, "Double beta decay," *Progress in Particle and Nuclear Physics*, vol. 12, pp. 409–479, 1984.

[16] J. Schechter and J. Valle, "Neutrinoless double-β decay in SU(2)$\times$U(1) theories," *Phys. Rev. D*, vol. 25, p. 2951, 1982.

[17] V.M. Gehman and S.R. Elliott, "Multiple-isotope comparison for determining $0\nu\beta\beta$ mechanisms," *Journal of Physics G: Nuclear and Particle Physics*, vol. 34, pp. 667–678, 2007.

[18] M. Doi, T. Kotani, H. Nishiura, K. Okuda, and E. Takasugi, "Double beta decay," *Prog. Theor. Phys.*, vol. 69, p. 602, 1983.

[19] F. T. Avignone, S. R. Elliott, and J. Engel, "Double beta decay, majorana neutrinos, and neutrino mass," *Rev. Mod. Phys.*, vol. 80, pp. 481–516, Apr 2008.

[20] G. J. Feldman and R. D. Cousins, "Unified approach to the classical statistical analysis of small signals," *Phys. Rev. D*, vol. 57, p. 3873, Apr. 1998.

[21] F. James, *Statistical Methods in Experimental Physics, 2nd Ed.* World Scientific Publishing Co., 2006.

[22] E. Fiorini, A. Pullia, G. Bertolini, F. Cappellani, and G. Restelli, "A search for lepton non-conservation in double beta decay with a germanium detector," *Physics Letters B*, vol. 25, pp. 602–603, Nov. 1967.

[23] H. V. Klapdor-Kleingrothaus, H. Pas, and A. Y. Smirnov, "Neutrino mass spectrum and neutrinoless double beta decay," *Physical Review D*, vol. 63, p. 073005, 2001.

[24] C. E. Aalseth *et al.*, "IGEX ^{76}Ge neutrinoless double-beta decay experiment: Prospects for next generation experiments," *Physical Review D*, vol. 65, p. 092007, May 2002.

[25] H. V. Klapdor-Kleingrothaus, A. Dietz, H. L. Harney, and I. V. Krivosheina, "Evidence for Neutrinoless Double Beta Decay," *Modern Physics Letters A*, vol. 16, pp. 2409–2420, 2001.

[26] H. V. Klapdor-Kleingrothaus and I. V. Krivosheina, "The evidence for the observation of 0nu beta beta decay: The identification of 0nu beta beta events from the full spectra," *Mod. Phys. Lett.*, vol. A21, pp. 1547–1566, 2006.

[27] C. E. Aalseth *et al.*, "Comment on 'evidence for neutrinoless double beta decay'," *Modern Physics Letters A*, vol. 17, pp. 1475–1478, 2002.

[28] S. Elliott *et al.*, "The MAJORANA Project," *Journal of Physics: Conference Series*, vol. 173, p. 012007, 2009.

[29] I. Canberra Industries, 2009. Broad Energy Ge Detectors, Canberra Industries, Inc., 800 Research Parkway, Meriden, CT 06450, U.S.A.

[30] R. Cooper, D. Radford, K. Lagergren, J. Colaresi, L. Darken, R. Henning, M. Marino, and K. Yocum, "A Pulse Shape Analysis Technique for the MAJORANA Experiment." *submitted to Nucl. Inst. & Meth. A* (2010).

[31] J. Janicskó-Csáthy, "Status of the gerda experiment," *Nuclear Physics B - Proceedings Supplements*, vol. 188, pp. 68 – 70, 2009. Proceedings of the Neutrino Oscillation Workshop.

[32] G. F. Knoll, *Radiation Detection and Measurement*. New York, USA: John Wiley & Sons, 2000.

[33] C. E. Aalseth. Personal communication.

[34] M. Leung, *The Borexino Solar Neutrino Experiment: Scintillator Purification and Surface Contamination*. PhD thesis, Princeton, 2006.

[35] L. C. Stonehill, *Deployment and Background Characterization of the Sudbury Neutrino Observatory Neutral Current Detectors*. PhD thesis, University of Washington, 2005.

[36] S. Agostinelli *et al.*, "Geant4: A simulation toolkit," *Nuclear Instruments and Methods in Physics Research A*, vol. 506, pp. 250–303, 2003.

[37] Qinetic Geant4 Developers, "Geant4 general particle source," 2004. http://reat.space.qinetiq.com/gps/.

[38] G. A. Cox, C. A. Duba, M. A. Howe, S. McGee, A. W. Myers, K. Rielage, R. G. H. Robertson, L. C. Stonehill, B. L. Wall, J. F. Wilkerson, and T. D. Vanwechel, "Sudbury Neutrino Observatory Neutral Current Detectors Signal Readout System," *IEEE Transactions on Nuclear Science*, vol. 51, pp. 2227–2230, Oct. 2004.

[39] XIA, "User's manual: Digital Gamma Finder (DGF)," 2004.

[40] A. Artna-Cohen *Nuclear Data Sheets*, vol. 80, p. 723, 1997.

[41] M. Basunia *Nuclear Data Sheets*, vol. 107, p. 3323, 2006.

[42] E. Browne *Nuclear Data Sheets*, vol. 104, p. 427, 2005.

[43] M. Martin *Nuclear Data Sheets*, vol. 108, p. 1583, 2007.

[44] S. Wu in *Nuclear Data Sheets*, vol. 108, p. 1057, 2007.

[45] XIA. http://www.xia.com.

[46] XIA, 2009. *What's New in the DGF-4c Revision 4.04*.

[47] M. Ballintijn, C. Loizides, and C. Reed, "Tree analysis modules," 2008.

[48] C. E. Aalseth, *Germanium Spectrometer Pulse-Shape Discrimination for ^{76}Ge Double-Beta Decay*. PhD thesis, University of South Carolina, 2000.

[49] V. M. Gehman, *Physics Reach of the Global Neutrinoless Double-Beta Decay Program and Systematic Uncertainties of the Majorana Pro ject*. PhD thesis, University of Washington, 2007.

[50] ORTEC. Advanced Measurement Technology, Inc, http://ortec-online.com.

[51] I. P. Laboratories, 2008. http://isotopeproducts.com.

[52] W. Leo, *Techniques for Nulear and Particle Physics Experiments: A How-To Approach*. Springer-Verlag, 1994.

[53] A. Rotondi and P. Montagna, "Fast calculation of vavilov distribution," *Nuclear Instruments and Methods in Physics Research*, vol. B47, pp. 215–223, 1990.

[54] J. Ziegler, "Stopping and ranges of ions in matter," 2009. Software Package.

[55] F. James, "`MINUIT` -function minimization and error analysis," *Cern Program Library*, vol. 94.1, 1998.

[56] G. Corporation. http://www.goodfellow.com.

[57] M. Berger *et al.*, "Stopping-power and range tables for electrons, protons, and helium ions," 2005. http://www.nist.gov/physlab/data/star/index.cfm.

[58] E.-I. Esch *et al.*, "The cosmic ray muon flux at WIPP," *Nucl. Instrum. Meth.*, vol. A538, pp. 516–525, 2005.

[59] R. H. Vreeland, W. D. Rosenzweig, and D. W. Powers, "Isolation of a 250 million-year-old halotolerant bacterium from a primary salt crystal," *Nature*, vol. 407, pp. 897–900, October 2000.

[60] K. Kazkaz, C. E. Aalseth, T. W. Hossbach, V. M. Gehman, J. D. Kephart, and H. S. Miley, "MEGA: A Low-Background Radiation Detector," *IEEE Transactions on Nuclear Science*, vol. 51, pp. 1029–1033, June 2004.

[61] H. Miley. Personal communication.

[62] D. Radford. Personal communication.

[63] B. Kayser. Personal communication.

Appendix A

USEFUL DERIVATIONS

A.1 Derivation of the See-Saw Mechanism

This section owes much to Boris Kayser [6, 63].

The addition of a right-handed mass term for the neutrino to the Standard Model lagrangian is a requirement for massive neutrinos, but the grouping of those terms can lead to Dirac-type terms, Majorana-like terms, or both. The see-saw mechanism follows from the addition of all Lorentz-invariant mass terms combining ψ_L, ψ_R, $(\psi^c)_L$, and $(\psi^c)_R$ with their adjoints.

The fields are denoted by ψ, with the subscripts L and R for left- and right-handed chirality. A superscript c denotes charge-conjugated field (anti-particle).

Start by writing down the term for a Dirac-type neutrino:

$$\begin{aligned} \psi_D &= \psi_L + \psi_R \\ \psi_D^c &= (\psi_L)^c + (\psi_R)^c \\ &= (\psi^c)_R + (\psi^c)_L \,. \end{aligned} \tag{A.1}$$

Combining Lorentz-invariant products of these fields and collecting them into the mass-portion of the Lagrangian:

$$\begin{aligned} -\mathcal{L}_D &= \frac{m_D}{2}\left(\overline{\psi}_R\psi_L + \overline{\psi}_L\psi_R + \overline{(\psi^c)}_L(\psi^c)_R + \overline{(\psi^c)}_R(\psi^c)_L\right) \\ &= \frac{m_D}{2}\left(\overline{\psi}_R\psi_L + \overline{\psi}_L\psi_R + \overline{(\psi_R)^c}(\psi_L)^c + \overline{(\psi_L)^c}(\psi_R)^c\right) \\ &= \frac{m_D}{2}\left(\overline{\psi}_R\psi_L + \overline{\psi}_L\psi_R + \overline{\psi}_L\psi_R + \overline{\psi}_R\psi_L\right) \\ &= m_D\left(\overline{\psi}_R\psi_L + \overline{\psi}_L\psi_R\right), \end{aligned} \tag{A.2}$$

where the propety that $(\psi_L)^c = (\psi^c)_R$ was used to show that the third and fourth product terms are equivalent to the first and second. These terms so far all conserve lepton number, i.e. left-handed neutrino couples to a right-handed neutrino, but other Lorentz-invariant products are valid as well. Another combination of terms leads to a second Lagrangian term:

$$-\mathcal{L}_M = \frac{m_R}{2}\left(\overline{(\psi^c)}_L\psi_R + \overline{\psi}_R(\psi^c)_L\right). \tag{A.3}$$

A similar term can be constructed with the interchange $R \leftrightarrow L$, resulting in a left-handed Majorana term. This is not strictly necessary and is omitted for pedagogic purposes.

It will be useful to gather terms,

$$\begin{aligned}\Lambda_1 &= \frac{\psi_L + (\psi^c)_R}{\sqrt{2}}\\ \Lambda_2 &= \frac{\psi_R + (\psi^c)_L}{\sqrt{2}},\end{aligned} \tag{A.4}$$

and then calculate their products:

$$\begin{aligned}\overline{\Lambda_1}\Lambda_2 &= \frac{1}{2}\left[\overline{\psi}_L\psi_R + \overline{\psi}_L(\psi^c)_L + \overline{(\psi^c)}_R\psi_R + \overline{(\psi^c)}_R(\psi^c)_L\right]\\ &= \frac{1}{2}\left[\overline{\psi}_L\psi_R + \overline{(\psi^c)}_R(\psi^c)_L\right]\\ &= \frac{1}{2}\left[\overline{\psi}_L\psi_R + \overline{\psi}_R\psi_L\right]\\ \overline{\Lambda_2}\Lambda_1 &= \frac{1}{2}\left[\overline{\psi}_R\psi_L + \overline{\psi}_R(\psi^c)_R + \overline{(\psi^c)}_L\psi_L + \overline{(\psi^c)}_L(\psi^c)_R\right]\\ &= \frac{1}{2}\left[\overline{\psi}_R\psi_L + \overline{(\psi^c)}_L(\psi^c)_R\right]\\ &= \frac{1}{2}\left[\overline{\psi}_R\psi_L + \overline{\psi}_L\psi_R\right]\\ \overline{\Lambda_2}\Lambda_2 &= \frac{1}{2}\left[\bar{\psi}_R\psi_R + \bar{\psi}_R(\psi^c)_L + \overline{(\psi^c)}_L\psi_R + \overline{(\psi^c)}_L(\psi^c)_L\right]\\ &= \frac{1}{2}\left[\overline{\psi}_R(\psi^c)_L + \overline{(\psi^c)}_L\psi_R\right].\end{aligned} \tag{A.5}$$

The two mass-Lagrangians are added together and simplified:

$$
\begin{aligned}
-\mathcal{L}_D - \mathcal{L}_R &= \left(m_D(\overline{\psi}_R \psi_L + m_D \overline{\psi}_L \psi_R) + \frac{1}{2} m_R (\overline{\psi}_R (\psi^c)_L + \overline{(\psi^c)}_L \psi_R) \right) \\
&= \left(m_D \left[\overline{\Lambda}_1 \Lambda_2 + \overline{\Lambda}_2 \Lambda_1 \right] + m_R \overline{\Lambda}_2 \Lambda_2 \right) \\
&= \begin{pmatrix} \overline{\Lambda}_1 & \overline{\Lambda}_2 \end{pmatrix} \begin{pmatrix} 0 & m_D \\ m_D & m_R \end{pmatrix} \begin{pmatrix} \Lambda_1 \\ \Lambda_2 \end{pmatrix} \\
&= \begin{pmatrix} \overline{\Lambda}_1 & \overline{\Lambda}_2 \end{pmatrix} S^{-1} S \begin{pmatrix} 0 & m_D \\ m_D & m_R \end{pmatrix} S^{-1} S \begin{pmatrix} \Lambda_1 \\ \Lambda_2 \end{pmatrix} \\
&= \begin{pmatrix} \overline{\nu} & \overline{N} \end{pmatrix} S \begin{pmatrix} 0 & m_D \\ m_D & m_R \end{pmatrix} S^{-1} \begin{pmatrix} \nu \\ N \end{pmatrix} \\
&= \begin{pmatrix} \overline{\nu} & \overline{N} \end{pmatrix} \begin{pmatrix} \frac{m_D^2}{m_R} & 0 \\ 0 & m_R \end{pmatrix} \begin{pmatrix} \nu \\ N \end{pmatrix}.
\end{aligned}
$$

The 4×4 matrix was diagonalized with a similarity transform S, and so the fields Λ_1 and Λ_2 are transformed into the physical neutrinos ν and N. For $m_R \rightarrow$GUT scale ($\sim 10^{15} - 10^{16}$GeV) and m_D a Dirac-type mass scale (1 MeV - 100 GeV), the corresponding mass of ν is small ($\frac{m_D^2}{m_R} \sim 1$ meV).

A.2 Derivation of Modified Gaussian Formula

A pulse-height spectrum of a monoenergetic source of particles depositing energy in an HPGe detector (e.g. a specific gamma line or an alpha source) will result in a peak at the particle's energy. This peak will in general not be completely gaussian, but instead will have a low-energy tail resulting from incomplete charge collection. This peak structure can be well-modeled by a gaussian convolved with an exponential rise, with the functions normalized and defined as

$$\mathcal{G}(\mu,\sigma,E) = \frac{1}{\sqrt{2\pi}\sigma}\exp\left(-\frac{(E-\mu)^2)}{2\sigma^2}\right) \tag{A.6}$$

$$\mathcal{D}(\mu,\tau,E) = \begin{cases} \frac{1}{\tau}\exp\left(\frac{E-\mu}{\tau}\right) & E \le \mu \\ 0 & E > \mu \end{cases} \quad . \tag{A.7}$$

The convolution integral is simplified considerably with the change of coordinates $x = E - \mu$ and proceeds as

$$\begin{aligned} \mathcal{S}(x) = (\mathcal{G} * \mathcal{D})(x) &= \int \mathcal{G}(x-u)\mathcal{D}(u)du \\ &= \left(\frac{1}{\tau\sigma\sqrt{2\pi}}\right)\int_{-\infty}^{0}\exp\left(\frac{u}{\tau}\right)\exp\left(\frac{-(x-u)^2}{2\sigma^2}\right)du \\ &= \left(\frac{1}{\tau\sigma\sqrt{2\pi}}\right)\int_{-\infty}^{0}\exp\left[\left(\frac{-1}{2\sigma^2}\right)\left(\frac{-2\sigma^2 u}{\tau} + x^2 - 2xu + u^2\right)\right]du \\ &= \left(\frac{1}{\tau\sigma\sqrt{2\pi}}\right)\int_{-\infty}^{0}\exp\left[\left(\frac{-1}{2\sigma^2}\right)\left(u^2 + u(-2x - 2\frac{\sigma^2}{\tau}) + x^2\right)\right]du \end{aligned} \tag{A.8}$$

Completing the square and collecting terms puts the integral into a more familiar form:

$$\begin{aligned} \mathcal{S}(x) &= \left(\frac{1}{\tau\sigma\sqrt{2\pi}}\right)\int_{-\infty}^{0}\exp\left[\left(\frac{-1}{2\sigma^2}\right)\left(\left(u - x - \frac{\sigma^2}{\tau}\right)^2 - x^2 - \frac{2x\sigma^2}{\tau} - \frac{\sigma^4}{\tau^2} + x^2\right)\right]du \\ &= \left(\frac{1}{\tau\sigma\sqrt{2\pi}}\right)\exp\left(\frac{x}{\tau}\right)\exp\left(\frac{\sigma^2}{2\tau^2}\right)\int_{-\infty}^{0}\exp\left[\frac{-(u-x-\sigma^2/\tau)^2}{2\sigma^2}\right]du \end{aligned} \tag{A.9}$$

Now make a simple substitution, letting $z = -(u - x - \sigma^2/\tau)/\sqrt{2}\sigma$ and therefore $dz =$

$-\frac{1}{\sqrt{2}\sigma}du$. The $u = 0$ integral limit becomes $z_0 = \frac{x}{\sqrt{2}\sigma} + \frac{\sigma}{\sqrt{2}\tau}$, and $u \to -\infty \Rightarrow z \to \infty$.

$$
\begin{aligned}
\mathcal{S}(x) &= -\sqrt{2}\sigma\left(\frac{\tau}{\sigma\sqrt{2\pi}}\right)\exp\left(\frac{x}{\tau}\right)\exp\left(\frac{\sigma^2}{2\tau^2}\right)\int_{\infty}^{z_0} e^{-z^2}dz \\
&= \sqrt{2}\sigma\left(\frac{1}{\tau\sigma\sqrt{2\pi}}\right)\exp\left(\frac{x}{\tau}\right)\exp\left(\frac{\sigma^2}{2\tau^2}\right)\int_{z_0}^{\infty} e^{-z^2}dz \\
&= \sqrt{2}\sigma\left(\frac{1}{\tau\sigma\sqrt{2\pi}}\right)\exp\left(\frac{x}{\tau}\right)\exp\left(\frac{\sigma^2}{2\tau^2}\right)\frac{\sqrt{\pi}}{2}\mathrm{Erfc}\left(z_0\right)
\end{aligned}
\tag{A.10}
$$

Where we have used the standard definition of the complementary error function. Now subbing back in z_0 and $x = E - \mu$, we are left with the final formula

$$
\mathcal{S}(E,\mu,\sigma,\tau) = \left(\frac{1}{2\tau}\right)\exp\left(\frac{E-\mu}{\tau}\right)\exp\left(\frac{\sigma^2}{2\tau^2}\right)\mathrm{Erfc}\left(\frac{E-\mu}{\sqrt{2}\sigma} + \frac{\sigma}{\sqrt{2}\tau}\right). \tag{A.11}
$$

The integral of $\mathcal{S}$ over E from $-\infty \to \infty$ is 1 thanks to the nice property that the convolution of two functions preserves their area, i.e.

$$
\int_{-\infty}^{\infty}(A * B)(x)dx = \left(\int_{-\infty}^{\infty} A(x)dx\right)\left(\int_{-\infty}^{\infty} B(x)dx\right) \tag{A.12}
$$

and because we started with two normalized functions.

It will also be useful to calculate the moments of the distribution. Reverting back to the variable $x = E - \mu$, The first moment is

$$
\begin{aligned}
\langle x\rangle &= \frac{1}{\sqrt{2\pi}\tau\sigma}\int_{-\infty}^{\infty} xdx\int_{-\infty}^{0} du\exp\left(\frac{u}{\tau}\right)\exp\left(-\frac{(x-u)^2}{2\sigma^2}\right) \\
&= \frac{1}{\sqrt{2\pi}\tau\sigma}\int_{-\infty}^{\infty}(y+u)dx\int_{-\infty}^{0} du\exp\left(\frac{u}{\tau}\right)\exp\left(-\frac{(y)^2}{2\sigma^2}\right) \\
&= \frac{1}{\tau}\int_{-\infty}^{0} u\exp\left(\frac{u}{\tau}\right)du = \frac{1}{\tau}\left[\exp\left(\frac{u}{\tau}\right)\left(u\tau - \tau^2\right)\right|_{-\infty}^{0} \\
&= -\tau \\
&\Rightarrow \mu_M = \mu - \tau,
\end{aligned}
\tag{A.13}
$$

and so we see that the mean of the distribution is shifted from the mean of the original gaussian by τ. The rest of the moments, centralized around the mean and normalized in the

Table A.1: Normalized moments around the mean for the modified-exponential gaussian

Mean (μ_M)	$\langle E \rangle$	$\mu_G - \tau$
Variance (σ_M^2)	$\langle (E - \mu_M)^2 \rangle$	$\sigma^2 + \tau^2$
Skewness	$\frac{\langle (E-\mu_M)^3 \rangle}{\sigma_M^3}$	$\frac{-2\tau^3}{(\sigma^2+\tau^2)^{3/2}}$
Kurtosis	$\frac{\langle (E-\mu_M)^4 \rangle}{\sigma_M^4} - 3$	$\frac{6\tau^4}{(\sigma^2+\tau^2)^2}$

case of the skewness and kurtosis, are found in Table A.1. Their calculations, while similar, are tedious and best left as an exercise for the reader or Mathematica. As expected, the mean, variance, skew, and kurtosis of the exponentially-modified gaussian approach their values for a gaussian distribution as $\tau \to 0$.

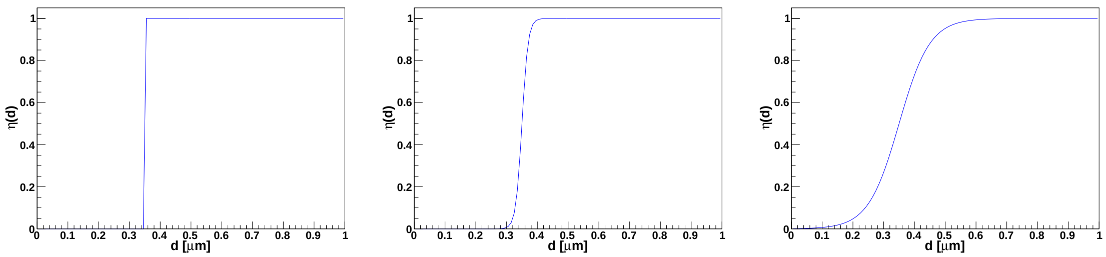

(a) Step-like efficiency profile (b) Slight sigmoid-like shape (c) Pronounced sigmoid-like shape

Figure A.1: Sample profile functions for charge-collection efficiency in dead regions of HPGe detectors.

A.3 Effect of Dead-Layer Profile on Surface-Alpha Depositions

The p^+ and n^+ contacts on HPGe diode detectors are formed by deposition of ions into the surface material (e.g. implantation of boron ions for the p^+ and lithium diffusion for the n^+). The layer formed by these impurities represents a region of sub-optimal charge collection. Assume a particle interacts within this region of the detector, depositing kinetic energy E in the form of E/2.71 keV electron-hole pairs. Because of the sub-optimal charge collection, some fraction will not be collected and so it will appear to the DAQ that less energy was deposited. Not only does this affect the efficiency of a detector, but it also allows higher energy particles the opportunity to degrade and deposit energy into the Q-value for $0\nu\beta\beta$.

An interesting question arises: what is the profile of this dead region? Let's assume that the efficiency of an interaction to register its full energy to the detector is 1 beyond a certain depth, i.e. the interior of the detector has little or no dead region. Furthermore, assume that the efficiency at the infinitesimal edge of the detector is 0. A simple model of the dead-layer profile can be constructed. Let $\eta(d)$ be the efficiency profile, as a function of depth d. Figure A.1 shows three such possibilities: one "step-like" function and two sigmoid-shaped functions.

Many preliminary simulations have assumed a shape such as in Figure A.1(a), with the dead layer having a concrete thickness. This model has no charge-collection within the dead region, and full-charge collection within the "active" region.. The question arises: is this treatment applicable, or is it necessary to discover a more-realistic efficiency profile?

A.3.1 Dead-Layer Profile: Step vs. Linear

Let ΔE be the energy loss by an alpha traveling through the p^+ dead-region of an HPGe crystal detector:

$$\Delta E = \int_0^{D_0} \frac{dE}{dX}(x)\bar{\eta}(d)dx, \tag{A.14}$$

where $\bar{\eta}(d) = 1 - \eta(d)$ becomes the efficiency profile for energy *loss* within the dead region of a detector. The upper limit in the integral is given as D_0, the distance the particle travels before it reaches $\bar{\eta}(d) = 0$. The integral is over x, the path that the particle travels, while $\bar{\eta}$ is a function of d, the depth. The relatively heavy alpha will not typically change direction until it slows appreciably, so the change of variable $d = \frac{x}{\cos(\theta})$ is justified for an alpha at incidence angle θ. Two examples of $\bar{\eta}(d)$ are shown in Figure A.2. While the shapes of $\bar{\eta}(d)$ differ qualitatively, they are constructed to give the same ΔE for an alpha at normal incidence to the surface. If we define Δ as the "typical" dead-layer thickness–that of the step function–than $D_0 = \Delta/\cos\theta$ for the step-function profile and $D_0 = 2\Delta/\cos\theta$ for the linear profile.

The stopping power $\frac{dE}{dX}$ is not a constant, but a function of the kinetic energy of the particle (Figure A.3(a)) [1, 57]. For an alpha of initial kinetic energy E_0, this $\frac{dE}{dX}$ can be expressed as a function of distance traveled through the detector (Figure A.3(b), for a 5.3 MeV alpha). Values of $\frac{dE}{dX}(E)$ were taken from [57] To facilitate the integral, a 2^{nd}-order polynomial is fit to the curve between 0 and 14 μm penetration depth (Table A.2).

With the polynomial approximation of dE/dX, the integral(Eq. A.14) is simply calculated for both $\bar{\eta}(d)$:

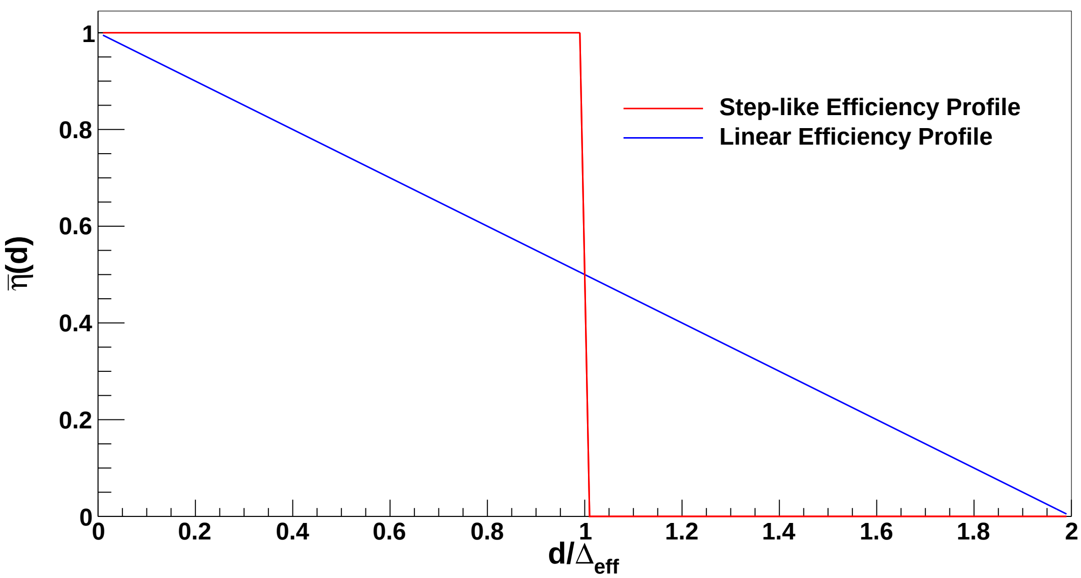

Figure A.2: Models for energy loss in the dead region on the surface of a detector. Here, $\bar{\eta}(d)$ represents the efficiency for that an energy deposit at depth d will not register with the DAQ. The idealized step-function case is compared with a linear model. Δ_{eff} represents an effective depth of the dead layer.

$$\begin{aligned}\Delta E_{step} &= \int_0^{\frac{\Delta}{\cos\theta}} \frac{dE}{dX} dx \qquad \text{(A.15)}\\ &= \int_0^{\frac{\Delta}{\cos\theta}} c_0 + c_1 x + c_2 x^2 dx \\ &= \frac{c_0 \Delta}{\cos\theta} + \frac{c_1 \Delta^2}{2\cos^2\theta} + \frac{c_2 \Delta^3}{3\cos^3\theta}\end{aligned}$$

Table A.2: Coefficients for 2nd-order fit of $\frac{dE}{dx}(x)$ for initial alpha energy of 5304 keV.

$\frac{dE}{dX}(x) \simeq c_0 + c_1 x + c_2 x^2$ $0 \leq x \leq 14\mu\text{m}$	
c_0	208.094
c_1	3.52529
c_2	0.39634

$$\begin{aligned}
\Delta E_{lin} &= \int_0^{\frac{2\Delta}{\cos\theta}} \frac{dE}{dX}\bar{\eta}(x)dx \qquad \text{(A.16)}\\
&= \int_0^{\frac{2\Delta}{\cos\theta}} \left(c_0 + c_1 x + c_2 x^2\right)\left(1 - \frac{x\cos\theta}{2\Delta}\right) dx\\
&= \int_0^{\frac{2\Delta}{\cos\theta}} \left[c_0 + \left(c_1 - \frac{c_0\cos\theta}{2\Delta}\right)x + \left(c_2 - \frac{c_1\cos\theta}{2\Delta}\right)x^2 - \frac{c_2\cos\theta}{2\Delta}x^3\right] dx\\
&= c_0 x + \left(c_1 - \frac{c_0\cos\theta}{2\Delta}\right)\frac{x^2}{2} + \left(c_2 - \frac{c_1\cos\theta}{2\Delta}\right)\frac{x^3}{3} - \frac{c_2\cos\theta}{2\Delta}\frac{x^4}{4}\Bigg|_0^{\frac{2\Delta}{\cos\theta}}\\
&= c_0\frac{\Delta}{\cos\theta} + \frac{2c_1}{3}\frac{\Delta^2}{\cos^2\theta} + \frac{2c_2}{3}\frac{\Delta^3}{\cos^3\theta}
\end{aligned}$$

The difference of the two models is

$$\Delta E_{step} - \Delta E_{lin} = \frac{c_1}{6}\frac{\Delta^2}{\cos^2\theta} + \frac{c_2}{3}\frac{\Delta^3}{\cos^3\theta}. \qquad \text{(A.17)}$$

As constructed, there is no disparity for constant $\frac{dE}{dX}(c_1 = c_2 = 0)$. Figure A.4 shows this difference in model predictions for two separate effective dead-layer depths. The disparity does not become appreciable ($>$ 1 keV) until above 70°.

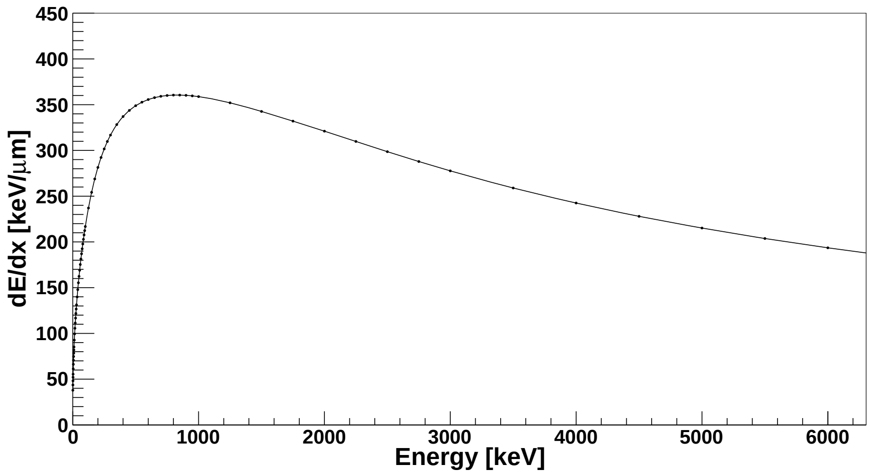

(a)

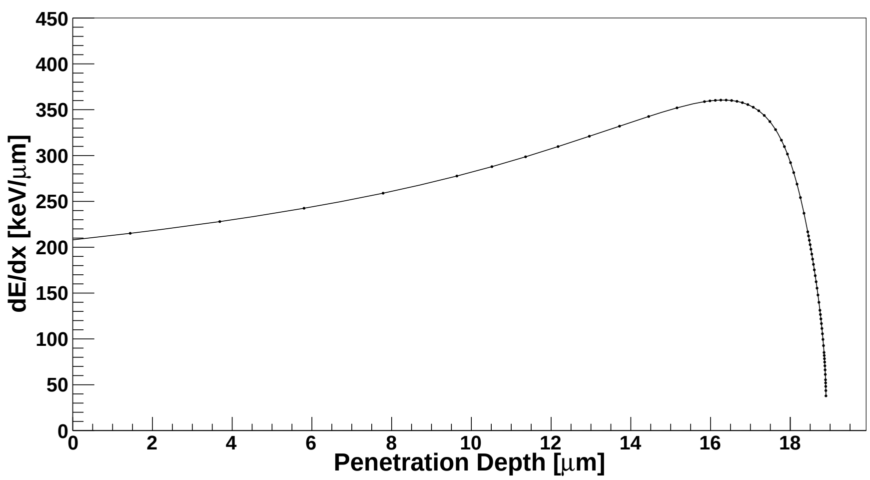

(b)

Figure A.3: Stopping power as function of energy (a) and penetration distance (b). Units have been converted to [keV/ μm] for alphas traveling through germanium. The curve in (a) is applicable for all alphas, but the curve in (b) depends on the initial kinetic energy (i.e. the energy of the alpha at 0 penetration depth) and was constructed for a 5.3 MeV alpha. Figures created using Stopping Range in Matter (SRIM) tables [54].

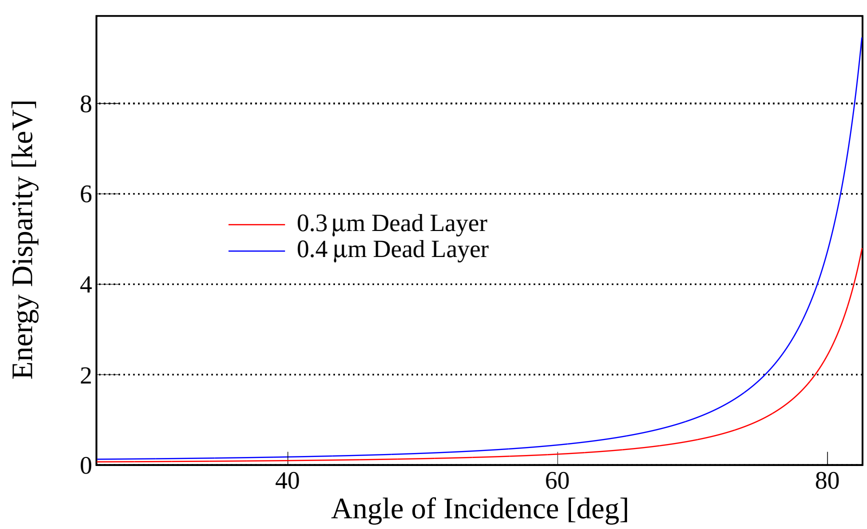

Figure A.4: The difference in energy loss in the dead region of a detector is shown for the step model and the linear model. Even for an effective dead layer depth of 0.4μm, the disparity isn't appreciable until angles of incidence higher than $70°$.

VITA

Rob was born in Arizona in 1979, moved briefly to Kentucky, and then landed in California's Bay Area in 1991. He attended the University of California at Berkeley (GO BEARS!), achieving a bachelor's degree with majors in Astrophysics, Mathematics, and Physics. While not playing frisbee golf on the Berkeley campus, he attended classes and dabbled in research in Astronomy (where he discovered Supernovae 1999cw and 1999da) and atomic physics. Rob took a year off after graduation to take stock of his life and in the meantime work in a condensed-matter lab looking at high-T_c superconductors. During that year, Rob applied to graduate schools and decided to attend the University of Washington in sunny Seattle. He joined the Electroweak Interactions Group under John Wilkerson and worked on the MAJORANA Experiment.

When not banging his head against a wall whilst doing physics, Rob enjoys riding and maintaining bicycles, cooking vegetarian food, brewing beer, drinking beer, and talking about brewing beer while drinking beer. He particularly enjoys playing outside (Rob's favorite subject in elementary school was Math, but Recess was a close second). He also finds it peculiar to talk about himself in the third person.